IPP-Report

MAX-PLANCK-INSTITUT
FÜR PLASMAPHYSIK

Raphael Schramm

Development and optimization of early-heating Advanced Tokamak scenarios using a predictive model

IPP 2024-05
Februar 2024

Development and optimization of early-heating Advanced Tokamak scenarios using a predictive model

Raphael Schramm

München 2023

Development and optimization of early-heating Advanced Tokamak scenarios using a predictive model

Raphael Schramm

Dissertation
der Fakultät für Physik
der Ludwig-Maximilians-Universität
München

vorgelegt von
Raphael Schramm
aus München

München, den 20.9.2023

Erstgutachter: Prof. Dr. Hartmut Zohm
Zweitgutachter: Prof. Dr. Harald Lesch
Tag der mündlichen Prüfung: 22.11.2023

Zusammenfassung

Thermonukleare Fusion ist der Schlüssel zu einer treibhausgasfreien, sicheren und nachhaltigen Energiequelle, sofern es gelingt, ein Wasserstoff-Plasma mit ausreichender Energiedichte einzuschließen. Das aktuell führende Konzept ist der Tokamak, eine torusförmige Maschine, die das Plasma durch ein helikales magnetisches Feld einschließt. Letzteres wird durch einen Strom innerhalb des donutförmigen Plasmas generiert. Konventionell wird dieser durch eine Transformator Spule induziert, bei der das Plasma als Sekundärwindung fungiert, wodurch allerdings inhärent die maximale Pulsdauer limitiert wird.

"Advanced Tokamak" Szenarien reduzieren diese Limitierung durch Hinzuziehen von zusätzlichen Stromquellen. Von besonderem Interesse ist der Bootstrap-Strom, ein selbstgenerierter Strom, der von Druckgradienten und Sicherheitsfaktor abhängt, letzterer ein Maß für die Helizität des Plasmas. Die Herausforderung besteht somit darin, diese Größen zu maximieren. Im einfachsten Fall werden, nachdem das Plasma einen stationären Zustand erreicht hat, zusätzliche Heizsysteme eingesetzt, um optimale Bedingungen für einen hohen Bootstrap-Strom zu generieren. Dieser Ansatz wurde in der Vergangenheit erfolgreich verwendet, seine Anwendbarkeit bei größeren Maschinen ist jedoch aufgrund der langsameren Reaktionszeit des Plasmas fragwürdig. Alternativ ermöglicht die Anwendung der zusätzlichen Heizsysteme bereits während der transienten Phase, ehe der Plasmastrom sein Gleichgewicht erreicht hat, eine direkte Steuerung in das gewünschte Szenario. Dies erlaubt gleichzeitig, den höheren Flussverbrauch der Transformatorspule in der Phase bevor das gewünschte Scenario erreicht ist zu limitieren. Da dieser Ansatz jedoch empfindlich vom Timing der Aktuatoren abhängt, schwer zu diagnostizieren und anfällig für Plasmainstabilitäten ist, erfordert ein rein empirisches Vorgehen in der Regel zahlreiche Iterationen.

Im Rahmen der vorliegenden Arbeit wurde ein Modell zur Bestimmung der für diesen zweiten Ansatz interessanten Parameter, mit Plasmadichte und verwendetem Heizszenario als Input, entwickelt. Die Verwendung eines vollständig analytischen Transportmodells mit freien Parametern, um Rechenzeiten von nur wenigen Minuten zu erreichen, ermöglicht die schnelle Berechnung der zahlreichen für Design des Szenarios erforderlichen Iterationen und erlaubt besser informierte Entscheidungen zwischen aufeinander folgenden Entladungen. Ein großer Teil des iterativen Einstellungsprozesses kann so in das Modell verschoben werden. Um dieses zu validieren, wurde ein neues Szenario für den ASDEX Upgrade Tokamak entwickelt und an der Maschine getestet. Nach Optimierung des Druckes konnte ein nicht-induktiver Anteil des Plasmastroms von mehr als 90% demonstriert werden.

Ein zweites Szenario mit höherer Leistung und einem anderen Heizformat, um näher an Reaktor-relevante Bedingungen heranzureichen, wurde optimiert. Mit einer kleineren Änderung eines freien Parameters konnte das Modell auch auf dieses, deutlich unterschiedliche Szenario, angewendet werden. Der Vergleich mit einem ähnlichen, wenn auch etwas einfacheren Modell zeigt eine gute Übereinstimmung, was die Glaubwürdigkeit des in dieser Arbeit entwickelten Modells untermauert.

Um zu untersuchen, wie gut das Modell verallgemeinert werden kann, wurde es an den größeren Tokamak JET angepasst. Wiederum war nur eine geringfügige Änderung der freien Parameter erforderlich, um eine gute Beschreibung der experimentellen Ergebnisse zu erreichen.

Abstract

Thermonuclear fusion offers access to green house gas emission free, safe, and sustainable energy, provided the challenges to confine hydrogen plasma at sufficient energy density can be overcome. The currently leading concept to achieve fusion is the tokamak, a torus-shaped device, confining the plasma by a helical magnetic field. Part of this field is generated by a current driven in the donut-shaped plasma. Conventionally, this current is induced by a transformer coil with the plasma acting as the secondary winding, thus inherently limiting the pulse duration.

Advanced tokamak scenarios reduce these limitations by exploiting additional current sources. In particular the bootstrap current, a self-generated current depending on the pressure gradient in the plasma and the safety factor, which is a measure of the helicity of the field, is of interest. The aim is therefore to maximize these quantities. The simplest way to enter a scenario conducive to a large bootstrap current fraction is to wait for the plasma to reach a stationary state and then to apply additional heating systems. This approach was used successfully in the past, but applicability to larger machines is questionable due to the slow response time of the plasma. Instead, applying the additional heating already during the early phase, while the plasma current is not yet fully established, allows for a direct entry into the desired regime. This also allows to limit flux consumption of the transformer coil in the phase before the desired scenario is reached. As this second approach is sensitive to actuator timings, hard to diagnose, and susceptible to plasma instabilities, fully empirical design usually requires many iterations.

In the present work a model was developed, which predicts the behavior of the quantities of interest for this second scenario, based on the density and heating setup as inputs. Using a fully analytical transport model with free parameters to achieve run times around a few minutes enables fast calculation of the iterations required for scenario design and testing between subsequent discharges, allowing for more informed decisions. A large part of the iterative process can thus be moved to the model. In order to validate the modeling system, it was used to design a new scenario for the ASDEX-Upgrade tokamak, which was tested on the device. After optimization of the pressure, a non-inductive current fraction of above 90 % could be demonstrated. A second scenario was optimized, using higher power and a different heating setup to achieve more reactor-relevant conditions. With a minor modification to a free parameter, the model is also applicable to this significantly different scenario. Comparison to a similar, albeit somewhat simpler model shows good agreement, strengthening the credibility of the model.

To investigate how well the model can be generalized, it was adapted to the larger tokamak JET, where it was found that again only a minor modification of the free parameters was needed to achieve a good description of the experimental findings.

Contents

1 Introduction **1**
1.1 Thermonuclear Fusion 2
1.2 Magnetic confinement 4
1.2.1 The Tokamak 5
1.2.2 Advanced Tokamak Scenarios 6
1.3 This Thesis 9

2 Physics background **11**
2.1 Tokamak equilibrium 12
2.1.1 The Grad-Shafranov equation 13
2.1.2 Plasma geometry 14
2.1.3 The plasma safety factor 15
2.2 Classical transport 16
2.3 Neoclassical transport 16
2.3.1 Bootstrap current 18
2.4 Turbulent transport 19
2.4.1 Drift wave 19
2.4.2 Interchange instability 20
2.4.3 Critical gradients 21
2.5 Bohm/gyro-Bohm transport scaling 22
2.6 The High confinement mode 23
2.7 Plasma instabilities 24
2.7.1 Sawteeth 25
2.7.2 Ideal modes 26
2.7.3 Neoclassical Tearing Modes 28
2.7.4 MARFE 30

3 Experimental setup and diagnostics **31**
3.1 ASDEX-Upgrade . . . 31
3.2 JET . . . 32
3.3 Heating systems . . . 33
3.3.1 Neutral beam injection . . . 34
3.3.2 Electron Cyclotron resonance heating . . . 38
3.4 Diagnostics . . . 42
3.4.1 Electron cyclotron emission . . . 42
3.4.2 Thomson Scattering . . . 43
3.4.3 Interferometry . . . 44
3.4.4 Charge Exchange Recombination Spectroscopy . . . 44
3.4.5 Magnetics . . . 45
3.4.6 Manometers . . . 46
3.5 Data analysis . . . 46
3.5.1 Integrated data analysis at AUG . . . 46
3.5.2 Equilibrium reconstruction at AUG . . . 47
3.5.3 Equilibrium reconstruction at JET . . . 48

4 Advanced Tokamak Scenarios **49**
4.1 Background . . . 49
4.2 Late heating and early heating . . . 51
4.3 Hybrid vs advanced . . . 53
4.4 Previous work on AUG and other machines . . . 54
4.5 Experimental approach on AUG . . . 55

5 Model **59**
5.1 ASTRA . . . 59
5.2 Model setup . . . 59
5.3 The transport model . . . 61
5.3.1 Parameter fit . . . 66
5.4 Model limitations . . . 68

6 Model application **69**
6.1 Designing a new early-heating AT scenario . . . 69
6.2 Experimental results . . . 72
6.3 Performance of the scenario . . . 76
6.3.1 Stability limits . . . 77

7 Application to a 1 MA scenario **81**
7.1 The counter ECCD setup . . . 81
7.2 Comparison to a RAPTOR model . . . 83
7.3 Improving the scenario . . . 84
7.3.1 Further optimizations . . . 88
7.3.2 Attempting to stabilize the 3/2 mode . . . 89
7.4 NTM stabilization through reduced current . . . 92
7.4.1 Performance of the lower current scenario . . . 96
7.5 Summary and discussion . . . 98

8 Application to a bigger machine **101**
8.1 Testing with older discharges . . . 101
8.2 Potential issues . . . 105
8.3 Discussion . . . 108

9 Summary and Outlook **111**

A Additional Information **117**
A.1 A mode-free 1MA discharge . . . 117
A.2 An issue with the divertor neutral pressure . . . 119
A.3 Performance of noteworthy discharges . . . 120
A.4 Parameter fit . . . 120
A.4.1 AUG, 800kA scenario . . . 120
A.4.2 JET . . . 122
A.5 Comparison of MHD markers to IDE . . . 123

B A density model **125**
B.1 The model . . . 125
B.2 Results . . . 128
B.2.1 The density of 41400 . . . 130

References **135**

Image sources **145**

Acknowledgments **147**

Chapter 1

Introduction

Since the discovery of electricity, the demand for energy has constantly been strongly increasing as it constitutes a corner stone of modern society. As the world population is expected to keep growing, and an increase in living standards, particularly visible in developing countries, generally increases the demand for electricity, this trend is not expected to stop anytime soon [1].

At the same time, the effects of global warming driven by the burning of fossil fuels, evidenced by a steep increase of the frequency of extreme weather conditions such as heat-waves, droughts and heavy precipitation, endangers the living conditions of a substantial part of the world population and affects the biodiversity on earth [2].

The need to tackle this societal challenge has been recognized by most of the world's governments and efforts are being made to speed up a transition towards clean and sustainable sources of energy. The two most readily available sources of renewable energy are wind and solar energy. However, both have the major drawback of depending on the weather conditions and therefore cannot be considered as reliable. In order to mitigate the risk of a temporary mismatch between power consumption and production, availability of a reliable base-load is desirable.

The two carbon neutral options that could serve this purpose, are hydroelectric power and nuclear fission energy. However, hydroelectric power is limited by geographic availability and has considerable environmental impacts. While nuclear fission is a well-established and reliable technology, there are concerns regarding radiation safety, the possibility of weaponizing the technology and the still unsolved problem of the long term storage of nuclear waste. For those reasons, some countries such as Germany have opted out of this option [3]. The alternative is to keep some fossil fuel plants running or to try storing significant amounts of energy, which is

another not fully solved problem, in order to maintain the grid stability.

Thermonuclear fusion produces energy via the fusion reaction of hydrogen to helium. The required elements for this reaction are abundantly available, the process is passively safe and long term storage of radioactive waste is not required. While no serious forecast predicts fusion energy reactors to become reality in the very near future, fusion energy is nevertheless expected to be available "early in the second part of this century" [4]. Triggered amongst others by the impact of global warming, considerable interest has come about fusion energy, resulting in multiple start-ups trying to speed up the process, an increase in funding towards fusion research and a seminal position paper [5] on fusion research being published by the German Ministry for Education and Research (BMBF). Fusion is an attractive option for supplying a base-load and could help reduce the required amount of intermittent power.

1.1 Thermonuclear Fusion

Thermonuclear fusion is a process in which two elements merge into one heavier element. For sufficiently light elements, the binding energy per nucleon, i.e. the mass difference between the heavier element and the sum of its constituents, increases during this process (see figure 1.1). Following Einsteins law ($\Delta E = \Delta m c^2$), the mass difference is released in form of energy. As can be seen in figure 1.1, the energy released in a fusion process can be much larger than in a fission process, if the

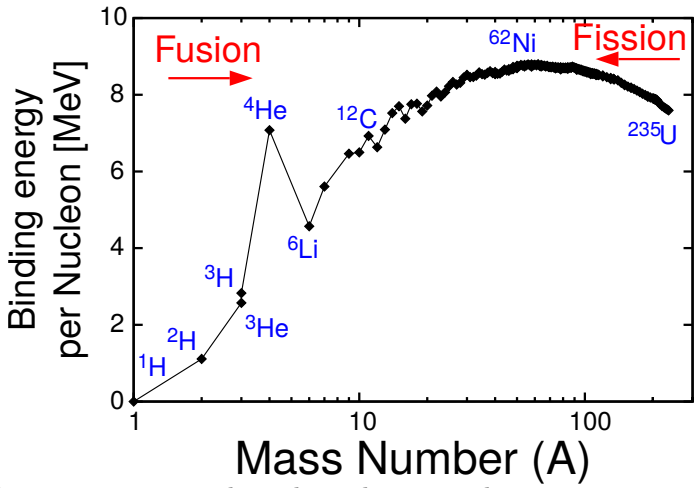

Figure 1.1: Binding energy per nucleon dependency on the atomic mass number (logarithmic scale); For the low mass elements the difference in binding energy is much larger (Figure based on [A])

appropriate reaction is chosen.

Fusion of hydrogen into helium via multiple intermediate steps is the fundamental process underlying the energy production of the sun and other stars. Fusion of two nuclei requires them to come close enough for the strong interaction to overcome the repulsive coulomb force. In the core of a star, this happens due to the enormous pressure generated by gravitation. As the initial step for the hydrogen fusion involves a proton turning into a neutron based on the weak interaction, the respective cross section is exceedingly low, rendering this process uninteresting for terrestrial fusion applications.

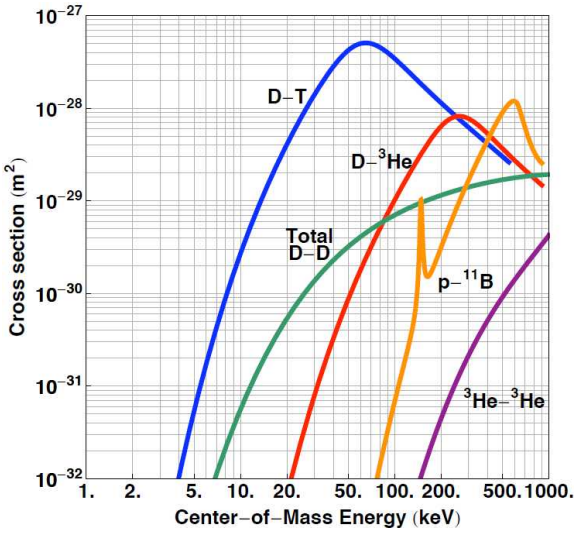

Figure 1.2: Reaction cross section versus center of mass energy for the most relevant fusion reactions (Note: this is a log-log plot); The D-T reaction achieves the highest cross-section, with its maximum appearing at the lowest center of mass energy, i.e. temperature [B]

There is however a large collection of relevant fusion interactions with much larger cross sections, the most commonly known ones are shown in figure 1.2. Among them, the reaction of the two isotopes of hydrogen, deuterium with one additional neutron, and tritium with two additional neutrons (see equation 1.1) is the most promising, since it combines the highest cross-section with the maximum arising at the lowest center of mass energy.

$$ {}^{2}_{1}\mathrm{D} + {}^{3}_{1}\mathrm{T} \rightarrow {}^{4}_{2}\mathrm{He}(3.5\mathrm{MeV}) + {}^{1}_{0}\mathrm{n}(14.1\mathrm{MeV}) \tag{1.1} $$

In order for this reaction to work, a set of requirements must be fulfilled. As can be seen in figure 1.2, a significant center of mass energy of $\sim$ 10keV (corresponding to a temperature of $\sim 10^8$K) is needed. This is required for the kinetic energy of

the particles to be sufficiently high to overcome the repulsive Coulomb interaction. Further, since Coulomb collisions are still more likely to occur, the particles have to be confined at a sufficiently high density for a sufficient amount of time. In order to be self-sustained, the energy generated by the reaction, excluding the neutrons since they cannot be confined, needs to be larger than the emitted power. This is expressed by the Lawson-criterion [6]:

$$nT_i\tau_E > 3 \cdot 10^{21}\,\mathrm{keV\,s\,m^{-3}} \tag{1.2}$$

with the ion temperature (T_i), the density n, and the energy confinement time τ_E, which is calculated by dividing the stored energy of the system by the emitted power (excluding the neutrons).

There are two overarching concepts to fulfill the Lawson-criterion: inertial confinement and magnetic confinement.

Inertial confinement uses high energy beams to deposit large amounts of energy in a small fuel-pellet, causing a strong compression and thereby pressure increase. On the relevant timescales, inertia is sufficient to generate the required confinement. Inertial confinement fusion fulfills the Lawson-criterion by achieving very high densities in order to compensate for the relatively short confinement time on the nanosecond scale.

The alternative is magnetic confinement, which will be the focus for the remainder of this work.

1.2 Magnetic confinement

In the magnetic confinement approach, the material is confined for a much longer time, achieving an energy confinement time of seconds at a considerably lower density. At the relevant temperatures, matter is in the plasma state, i.e. it is a fully ionized gas. While being globally neutral, in a plasma, electrons and ions are no longer directly bound and therefore individual particles carry an electrical charge. This allows to influence them by a magnetic field, which is used to confine the particles. The simplest possible configuration, a linear device trapping the particles on straight field-lines, does not provide sufficient confinement, due to the high losses at the end.

The obvious solution is to connect the ends, creating a torus. When doing so, particle drifts need to be considered. For particles trapped in a magnetic field, any external force will introduce a drift perpendicular to both the magnetic field and the acting force. The resulting drift speed ($\vec{v}_D$) is given by

$$\vec{v}_D = \frac{1}{q_{el}} \frac{\vec{F} \times \vec{B}}{B^2} \tag{1.3}$$

with the electrical charge of the particle q_{el}, the triggering force $\vec{F}$ and the magnetic field $\vec{B}$. In a torus-shaped setup, two effects have to be taken into account: the curvature of the particle trajectory and a gradient of the magnetic field, since the coil density is inherently higher on the inner side of the torus. Together, these effects lead to a drift of the plasma particles given by:

$$\vec{v}_D = \frac{m}{q_{el}B^3}\left(v_\parallel^2 + \frac{1}{2}v_\perp^2\right)\vec{B}\times\nabla B \tag{1.4}$$

where $v_\parallel$ and $v_\perp$ are the parallel and perpendicular component of the velocity with respect to the magnetic field lines and m is the particle mass. As the gradient of the magnetic field is pointing radially inwards, the resulting drift will be in the vertical direction. Since the particle charge is included, this will lead to a charge separation and thereby an electric field, which causes an additional drift

$$\vec{v}_D = \frac{\vec{E}\times\vec{B}}{B^2} \tag{1.5}$$

pointing outwards, independently of charge. Due to this outwards flow, particles cannot be confined in a purely toroidal magnetic field. The solution here is to add an additional poloidal component to the magnetic field, creating helical field lines such that the particles spend comparable amounts of time on the upper and lower side, thereby preventing a significant charge separation.

The two leading concepts are the stellarator and the tokamak.

In a stellarator, the magnetic field is created exclusively by a three-dimensional coil assembly, while a tokamak uses an internal plasma current for the creation of the poloidal magnetic field and axisymmetric coils for the creation of the troroidal magnetic field. For this reason the coils for a tokamak are usually much simpler.

The present thesis focuses on the tokamak concept.

1.2.1 The Tokamak

The tokamak has long been the leading candidate for a fusion power plant. First developed in the Soviet Union in the middle of the 20th century, its name is a transliteration from Russian and means "toroidal vessel with magnetic field coils". A schematic view of a tokamak is shown in figure 1.3. The toroidal part of magnetic field in a Tokamak is generated by a set of toroidal field coils (shown in blue). The poloidal part is induced by a plasma current. In order to generate this plasma current the current in the central poloidal field coil (also called transformer coil, shown in green) is ramped down, inducing a current in the plasma, which acts as

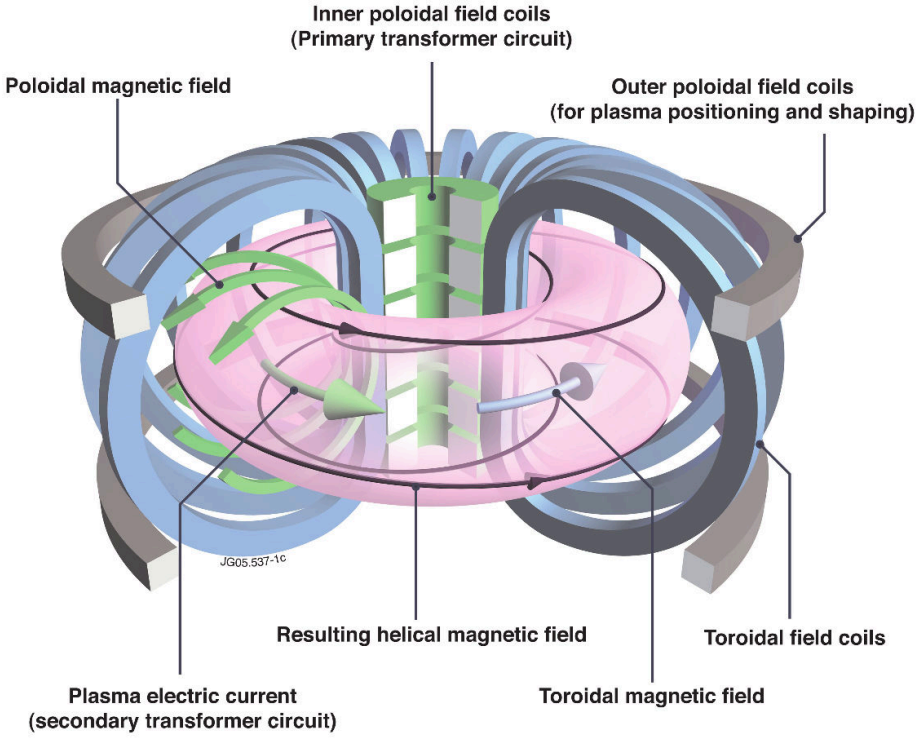

Figure 1.3: Schematic view of a tokamak [C]

the secondary winding of a transformer. Additional poloidal field coils (shown in gray) are present in order to control the shape and position of the plasma. As the plasma has a nonzero electrical resistance, the current in the transformer coil has to be further ramped down continuously, in order to keep the plasma current constant. This inherently limits the tokamak to pulsed operation as even superconducting coils reach a limit eventually. An additional downside of the plasma current is it being a source of free energy for instabilities, which introduces the possibility of a disruption, meaning a sudden loss of the plasma current leading to significant mechanical and thermal stress on the device.

1.2.2 Advanced Tokamak Scenarios

Advanced Tokamak (AT) scenarios aim at achieving steady state operation by reducing the need to rely on the inductive current supplied by the transformer coil. This can be achieved by making use of the bootstrap current (explained in more detail in

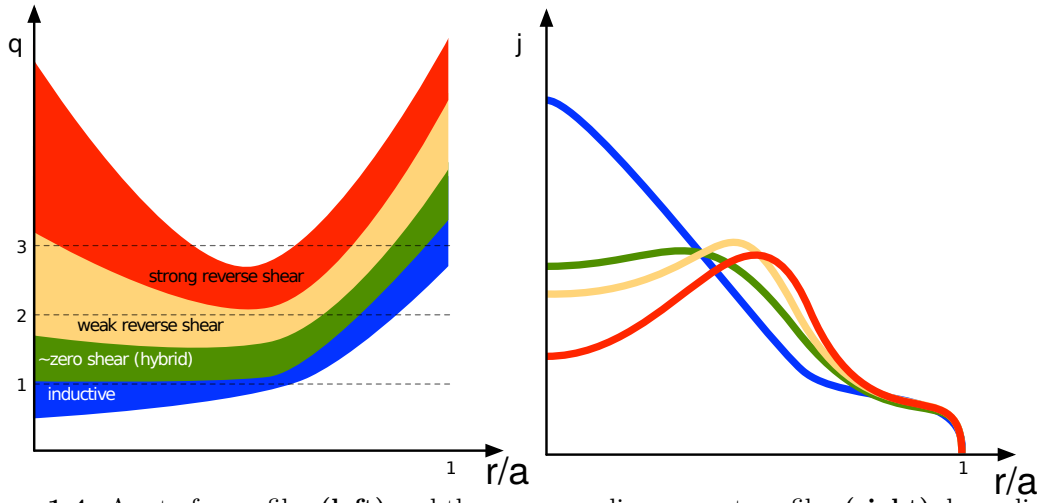

Figure 1.4: A set of q-profiles **(left)** and the corresponding current profiles **(right)** depending on the normalized radius [D]

section 2.3.1), which is a self generated current that can be described by

$$j_{bs} \propto q \cdot \nabla p \tag{1.6}$$

including the plasma plasma safety factor q (explained in more detail in section 2.1), which is a measure of the helicity of the magnetic field and the pressure gradient ∇p. Using external heating systems (see section 3.3) to drive current off axis, the q-profile can be modified from a shape as shown in blue in a stylized way in figure 1.4 to the higher regimes.

Two scenarios are usually being distinguished, the so-called hybrid scenario, where the q-profile reaches its minimum value slightly above one at the magnetic axis ($r/a = 0$), and the advanced scenario where the minimum is further outwards. While a discussion of these two setups is provided in section 4.3, this work focuses on the "advanced" case. In the right part of figure 1.4, the current profiles corresponding to the q-profiles are shown in matching colors. Starting with the inductive case shown in blue, increasing the off axis current raises the q-profile and thereby the bootstrap current. It should be noted, that the figure exaggerates the effect as increasing q at the edge ($r/a = 1$) would imply a reduction of the overall plasma current and thereby a lower confinement. A more realistic discussion of achievable profiles is given in chapter 4.

Unfortunately, a tokamak cannot start with any plasma current, it has to be ramped up from zero. This leads to an early phase, where the q-profile is strongly changing.

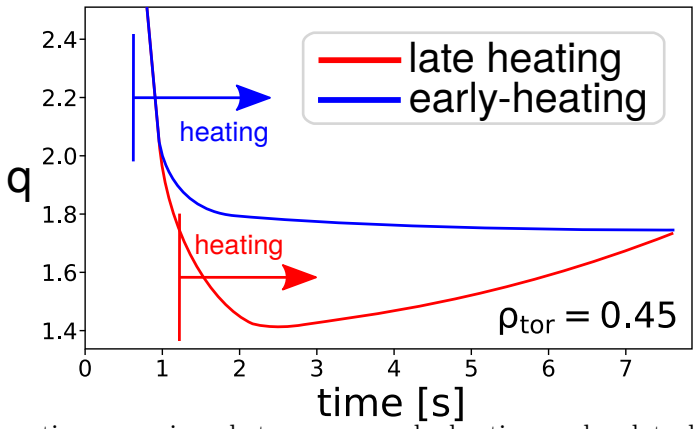

Figure 1.5: Schematic comparison between an early heating and a late heating case of the q-evolution (based on an AUG discharge)

The simple solution to initiate an advanced tokamak setup is to allow the plasma to reach a stationary state, before any additional heating is applied. This setup leads to a considerable drop in q, before it slowly starts rising again as shown in red in figure 1.5. The rate of the increase depends on the current diffusion time (τ_r)

$$\tau_r = \mu_0 \sigma L^2 \tag{1.7}$$

with the vacuum permeability μ_0, the volume averaged neoclassical conductivity σ and the characteristic length L, which is usually chosen as half of the minor radius. For ASDEX-Upgrade (see section 3.1) the resulting value for scenarios of interest is around $\tau_r \sim 1.5$s, making this approach acceptable. However, when considering machines of larger size, such as the International Thermonuclear Experimental Reactor (ITER), currently under construction in Southern France, one reaches values of several hundred seconds (estimation based on [7]), which is likely not a desirable approach anymore. For a future reactor, such as the European demonstration power plant (DEMO), which is being planned as a follow-up to ITER and is expected to be even larger, this problem would get worse.

The alternative approach is to apply the additional heating earlier, already during the phase, when the plasma current is increasing. This allows reaching a behavior as is sketched in figure 1.5 in blue. An additional benefit is, that the increased requirement of current from the transformer coil during the intermittent low-q phase can be avoided, which could potentially reduce the minimum size of this coil for future machines. However, this approach has the downside to be very sensitive to actuator timings and plasma instabilities, while also being harder to diagnose. For this reason, development of these scenarios usually takes a considerable amount of iterations if done fully empirically.

1.3 This Thesis

Experimental time at a tokamak is limited and expensive. For this reason, moving away from a fully empirical scenario design, where changes are made in an iterative approach until a desired behavior is achieved, seems advisable. The work presented in this thesis establishes a workflow for a stable path to the realization of such an early heating advanced scenario, while moving a considerable part of the iterative process to computational modeling. In order to get to that point, a model was developed, which can predict the behavior of temperature and safety factor profiles and time evolution depending on the heating setup for such a scenario in a reasonable amount of time.

This thesis is structured as follows: Chapter 2 provides a background for the relevant physics in this topic. Chapter 3 introduces the experimentally relevant systems. A more detailed view of Advanced Tokamak scenarios is provided in 4. The design of the model used for this work is presented in 5 and its application to design a new scenario on the ASDEX Upgrade (AUG) tokamak, as well as the performance of said scenario is shown in 6. Application to a different scenario for AUG has been tested, the results of which are presented in chapter 7. In order to test the general applicability of the model it has been tested on the considerably bigger JET tokamak, which is shown in chapter 8. Finally conclusions are provided in chapter 9

Chapter 2

Physics background

The plasma, which can be found in current tokamak fusion experiments can be described as a magnetized fluid, the behavior of which is explained by magneto-hydrodynamic (MHD) theory [8, 9]. The requirements for this are as follows: A large amount of particles per volume, meaning the gyroradius has to small with respect to the system size is generally fulfilled in a typical tokamak. The second requirement of a local thermodynamic equilibrium, meaning a small mean free path with respect to the system size is only fulfilled for the dynamic perpendicular to the magnetic field lines where the mean free path is given by the Larmor radius (see next section). For the dynamics parallel to the field lines, the mean free path in a tokamak is on the order of km. Therefore a kinetic description would be required for these effects. However, most macroscopic effects in a plasma are sufficiently described by the dynamics perpendicular to the field lines. If dynamics parallel to the field lines need to be considered, which is most relevant for turbulence effects, a kinetic theory is required. Two relevant timescales arise from MHD: The Alfvén time τ_A characterizing plasma waves perturbing the magnetic field lines, is given by

$$\tau_A = \frac{L\sqrt{\mu_0 \rho_n}}{B} \tag{2.1}$$

with the characteristic length of the system L and the mass density ρ_n. The resistive current diffusion time τ_R (see equation 1.7) describes phenomena affecting currents in the plasma. It is usually much longer (on the order of seconds for ASDEX Upgrade) than the Alfvén time (on the order of microseconds for ASDEX Upgrade).

2.1 Tokamak equilibrium

In a device using magnetic confinement, the plasma is forced to follow the magnetic field lines, since it consists mainly of charged particles, which are affected by the Lorentz force

$$\vec{F} = q_{\mathrm{el}}(\vec{E} + \vec{v} \times \vec{B}) \tag{2.2}$$

with the electric charge q_{el}. This force allows them to move freely in parallel to the field lines, but restricts the perpendicular motion to a circular trajectory. The radius of this motion is called Larmor-radius r_{L} and given by

$$r_{\mathrm{L}} = \frac{m v_{\perp}}{q_{\mathrm{el}} B} \tag{2.3}$$

with the particle mass m and the velocity perpendicular to the magnetic field $v_{\perp}$. The resulting behavior is a gyrating motion along the magnetic field lines. In order for such a configuration to be stable, the kinetic pressure resulting of the pressure gradient towards the plasma core needs to be balanced by the magnetic pressure from the applied field. This magnetostatic force balance can be written as

$$\nabla p = \vec{j} \times \vec{B} \tag{2.4}$$

with the plasma pressure p and the current density $\vec{j}$. A measure of the efficiency of this confinement is provided by the ratio of the total kinetic and magnetic pressure (β).

$$\beta = \frac{2\mu_0 \langle p \rangle}{B^2} \tag{2.5}$$

with the volume averaged pressure $\langle p \rangle$. As value for the magnetic field in this equation, the total field at the magnetic axis is being used. Alternatively, the poloidal β (β_{pol}) is calculated by using only the poloidal part of the magnetic field. In order to be able to compare different scenarios and devices more easily, a normalized β (β_N) is introduced:

$$\beta_N = \frac{a B_{tor}}{I_p} \beta \tag{2.6}$$

with the minor radius a, the toroidal magnetic field on the axis B_{tor} and the plasma current (I_p). This value originally comes from a stability consideration, in which it was found, that tokamaks become unstable to ideal MHD instabilities (see section 2.7.2), once a certain limit is exceeded. This limit was originally found to be reached at $\beta_N \sim 2.8$ [10] however, newer investigations taking into account a non-circular plasma shape could show that this limit is somewhat higher, around $\beta_N \sim 3.5$ [11] in typical tokamak operations. Depending on the current profile, this limit can also be considerably lower.

2.1.1 The Grad-Shafranov equation

Under the assumption of MHD theory [8], which treats the plasma as a single fluid, an equation for the magnetic structure can be derived from the radial part of equation 2.4 and the Maxwell equations. The coordinate system used for these calculations is displayed in figure 2.1. This is the Grad-Shafranov equation [12, 13]

$$\Delta^* \psi = -\mu_0 2\pi R j_\phi = -\mu_0 (2\pi R)^2 \frac{dp}{d\psi} - \mu_0^2 \frac{dI_{pol}}{d\psi} I_{pol} \tag{2.7}$$

where Δ^* is the Stokes operator, R is the major radius of the tokamak, j_ϕ is the toroidal current density, I_{pol} is the poloidal current and ψ is the poloidal magnetic flux, defined as the integral over a poloidal surface S_ψ. Analogously the toroidal flux is defined as an integral over a topologically different toroidal surface S_ϕ. Note that these surfaces do not have to be planar.

$$\phi = \int_{S_{tor}} \mathbf{B} \cdot d\mathbf{S} \qquad \psi = \int_{S_{pol}} \mathbf{B} \cdot d\mathbf{S} \tag{2.8}$$

Solutions to the Grad-Shafranov equation consist of a set of nested surfaces of constant flux, pressure and poloidal current density. These are usually called flux-surfaces. A visualization of this is shown in figure 2.1.

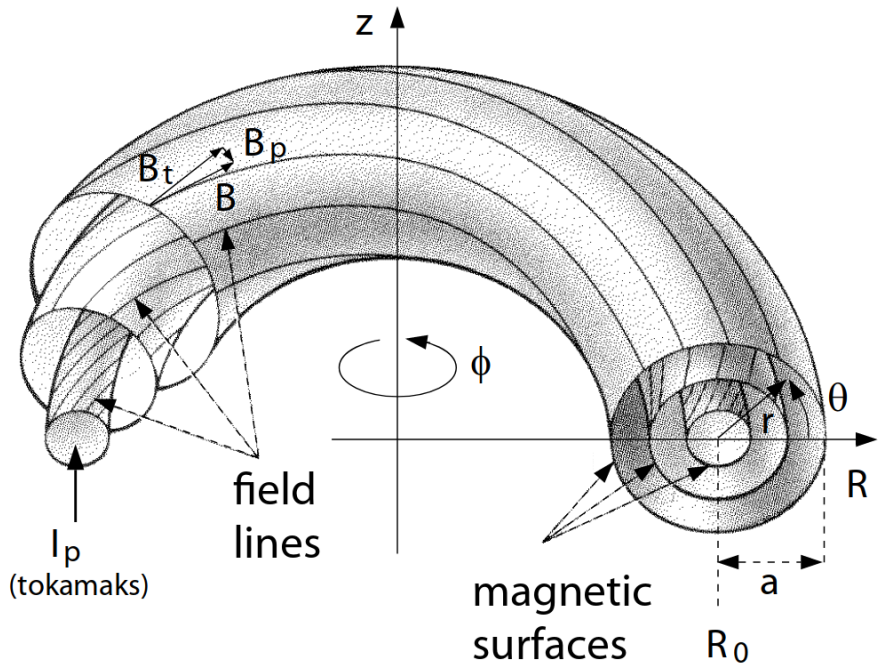

Figure 2.1: Schematic view of the flux surfaces in a tokamak [E]

Using the fact, that parameters are constant on flux surfaces, their description can be further simplified to a 1D radial profile. In order to preserve comparability between different machines, a coordinate system based on the normalized toroidal flux (ρ_{tor}) and normalized poloidal flux (ρ_{pol}) is introduced:

$$\rho_{pol} = \sqrt{\frac{\psi - \psi_{\text{axis}}}{\psi_{\text{separatrix}} - \psi_{\text{axis}}}} \qquad \rho_{tor} = \sqrt{\frac{\phi - \phi_{\text{axis}}}{\phi_{\text{separatrix}} - \phi_{\text{axis}}}} \tag{2.9}$$

where "axis" refers to the value at the magnetic axis and "separatrix" refers to the value at the last closed flux-surface (see next section). By definition, these values are zero at the magnetic axis and one at the separatrix.

2.1.2 Plasma geometry

A typical cross section of a tokamak is shown in figure 2.2 at the example of the ASDEX Upgrade tokamak. In order to improve transport properties and thereby confinement, the plasma shape is elongated and slightly triangular. There are two types of flux surfaces visible in the figure, with their field lines shown in red. Inside the blue so-called separatrix the corresponding field lines are closed, providing a good confinement. Outside of it, the corresponding field lines are open and intersect with plasma facing components. The location, where the separatrix intersects with itself is called X-point. The configuration shown in figure 2.2 is the so-called divertor configuration, where only the open field lines hit a dedicated location of the wall, the divertor. This configuration prevents impurities from the wall from getting into the main confined plasma region, allowing for better performance. In the alternative, so-called limiter configuration, a clear separatrix is not present. Instead the region of closed flux surfaces intersects directly with the wall. In this configuration, radiation from impurities introduced from the wall significantly reduced the plasma stored energy making the configuration not desirable. This configuration is usually present during the early

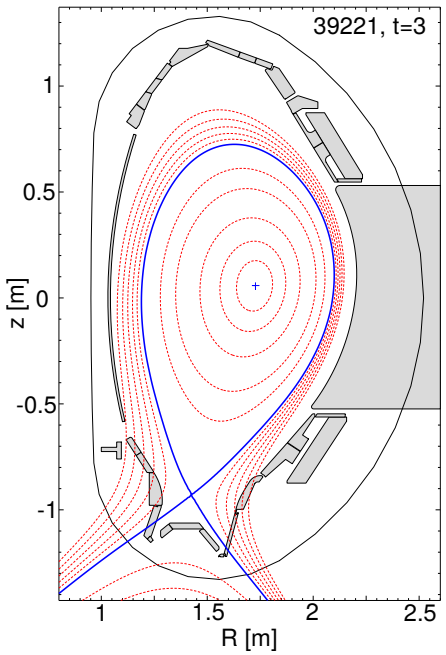

Figure 2.2: Cross-section of the ASDEX-Upgrade tokamak

ramp-up of a device, limiting the earliest time, where relevant performance can be expected.

2.1.3 The plasma safety factor

The helicity of the magnetic field is the ratio between the poloidal and toroidal magnetic flux, which can be understood as the value of the ratio of poloidal and toroidal turns a field line does around the torus before closing in on itself. This parameter is commonly described by the plasma safety factor (q):

$$q = -\frac{d\phi}{d\psi} \approx \frac{r}{R}\frac{B_{tor}}{B_{pol}} \tag{2.10}$$

with the minor radius (r) and the major radius (R), where the second approximation assumes a small inverse aspect ratio $\epsilon = r/R \ll 1$, which is reasonable for a standard tokamak. A second assumption of circular poloidal cross section is usually not fulfilled however, the relation still works as an approximation. The most significant deviation happens at the separatrix, since the poloidal magnetic field becomes zero at the X-point, causing the safety factor to diverge. For this reason, the safety factor at 95% of the flux (q_{95}) is usually used for comparisons. As B_{tor} is generated by the toroidal field coils and mostly independent of the behavior of the plasma, changes to q are largely driven by B_{pol}. As B_{pol} is mostly generated by the plasma current, the shape of the q-profile is strongly tied to the current distribution in the plasma.

The name "safety factor" comes from the fact, that it plays a significant role in plasma stability as it was found, that a plasma is always unstable to an external kink mode (described in section 2.7.2) if the safety factor at the separatrix drops below one. This is called the Kruskal–Shafranov limit [14, 15], although in realistic tokamak operations, a higher order mode already prevents operation for $q_{95} < 2$ [8].

Further, flux surfaces with rational plasma safety factor ($q = m/n$ with $m, n \in \mathbb{N}$) are susceptible to instabilities (see section 2.7.3) since they close in on themselves thereby allowing periodic perturbations to grow.

The magnetic shear (S) is a measure of how much the safety factor changes with the radius. It is given by

$$S = \frac{r}{q}\frac{dq}{dr} \tag{2.11}$$

and plays a role both in particle and heat transport as well as for the stability of the plasma.

2.2 Classical transport

Charged particles in a magnetic field can move freely along field lines, while their movement perpendicular is limited to a gyrating motion. If more than one particle is considered, perpendicular transport can however occur through collisions. This phenomenon is called classical or collisional transport and can be described in a simplified fashion with a random walk model. The assumption is that, on average collisions move a particle by a distance of Δx per time interval Δt. Since the direction of this movement is random, the average position of a particle does not change. However, a normal distribution centered around zero, whose width increases over time, develops. This process can be described by a diffusion coefficient

$$D = \frac{(\Delta x)^2}{\Delta t} \tag{2.12}$$

In classical transport theory of a magnetized plasma, the characteristic length scale of collisions and thereby Δx is described by the Larmor radius (see equation 2.3). The resulting diffusion coefficient is given by

$$D_c = r_{\mathrm{L}}^2 \nu \tag{2.13}$$

where ν is the collision frequency. For particle transport to occur, a gradient in particle density is required, while for heat transport a temperature gradient is necessary.

2.3 Neoclassical transport

As already mentioned in the previous section, the geometry of a tokamak generates a gradient of the magnetic field, decreasing with the plasma radius. With reference to the magnetic axis, the half of the plasma experiencing the higher magnetic field is called High Field Side (HFS), while the other half is called Low Field Side (LFS). Due to the helical nature of the magnetic field in a tokamak, a particle following a magnetic field line experiences this gradient. In addition to drift effects, this also generates a magnetic mirror. As the magnetic moment of a particle is invariant, given by $\mu_0 = \frac{m v_\perp^2}{2B}$ a change of the magnetic field also changes $v_\perp$ and thereby, due to conservation of the kinetic energy, $v_\parallel$. If $v_\parallel$ reaches zero, the particle is reflected by the magnetic field and its trajectory is reversed. Building on that, a so-called mirror condition can be formulated:

$$\frac{v_\parallel^2}{v_\perp^2} < \frac{B_{\max}}{B_{\min}} - 1 = \frac{B_0(R_0 - r)}{B_0(R_0 + r)} - 1 = \frac{2r/R_0}{1 - r/R_0} \tag{2.14}$$

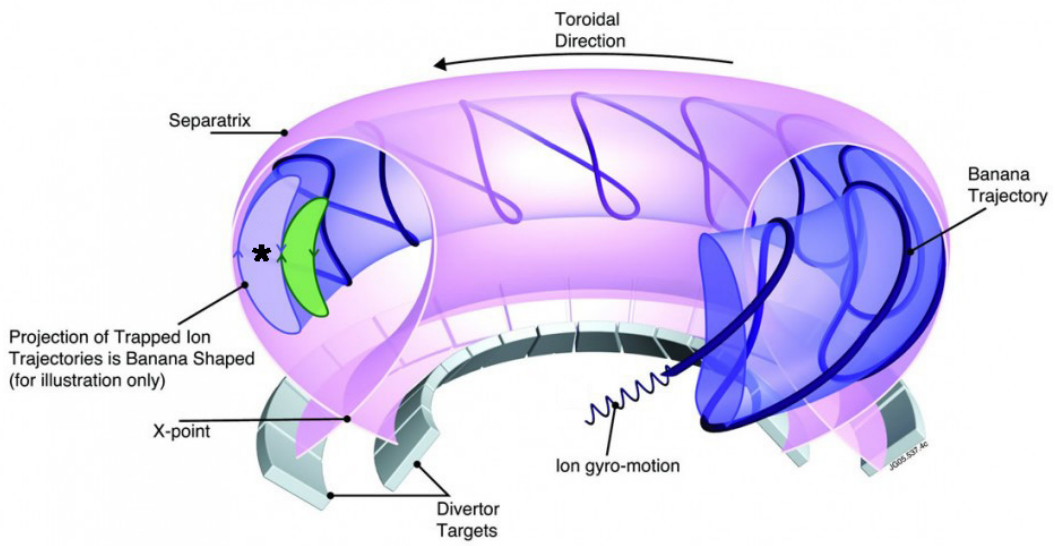

Figure 2.3: Banana orbits around a tokamak [F]

The particle is trapped, if the condition is fulfilled. R_0 is the major radius of the machine and r is the minor radius of the flux surface of interest. For the equality, $B = \frac{B_0 R_0}{R}$, where R is the major radius of the flux surface of interest, was used. Assuming a small inverse aspect ratio $\epsilon = \frac{r}{R}$, which is a reasonable assumption for a typical tokamak, the mirror condition becomes

$$\left| \frac{v_\parallel}{v_\perp} \right| < \sqrt{2\epsilon} \tag{2.15}$$

Assuming the particle velocities to follow a Maxwell distribution, the trapped particle fraction can be estimated as $f_t = n_t/n = \sqrt{\epsilon}$. While this trapping only causes an oscillation along a magnetic field line, the same drift mentioned in section 1.2 causes a movement for an ion inward when moving from the LFS to the HFS and opposite on the way back. This trend is reversed for electrons. The considerably smaller poloidal part of the magnetic field causes an additional ∇B drift, leading to a slow precession in toroidal direction. The resulting trajectory of the particles which is called a banana-orbit is shown in figure 2.3. Based on the same random walk principle as in the classical transport, a diffusion coefficient can be calculated. The characteristic length w_B is the width of the banana orbit, which can be calculated by using the drift velocity v_d and the time a particle requires to pass through one orbit, which

can be calculated from the length of the orbit L and the parallel velocity.

$$w_B = v_D \frac{L}{v_\parallel} = r_L \frac{q}{2} \frac{v_\perp}{v_\parallel} \nabla\theta \sim r_L \frac{q}{\sqrt{\epsilon}} \tag{2.16}$$

where $\nabla\theta$ is the poloidal angle from the point of maximum to minimum magnetic field on one orbit, which is equal to π for the maximum size orbit. With an effective collision frequency of $\nu_{\text{eff}} = \frac{\nu}{2\epsilon}$, which is higher than in the classical case, since the collision only has to be strong enough for a trapped particle to become free, the diffusion coefficient becomes

$$D_{neo} = w_B^2 \nu_{\text{eff}} f_t = r_L^2 \frac{q^2 \nu}{2\epsilon^2} \sqrt{2\epsilon} \sim \frac{q^2}{\epsilon^{(3/2)}} D_c \tag{2.17}$$

and is now called neoclassical.

2.3.1 Bootstrap current

If a radial pressure gradient ∇p is present, particles on the part of the banana orbit further inside the plasma experience a higher density and temperature than those in the outside part. Due to overlapping banana orbits, this leads to more and higher energy particles moving in one direction than in the other, and thereby to a mostly toroidal current generated by the trapped particles. Collisions of the trapped particles with the passing electrons result in a force, accelerating electrons and thereby creating an additional contribution to the current [16]. The bootstrap current is then given by [17, 18]:

$$\langle j_{BS} B \rangle = -I(\psi) p_e \times \left(\mathcal{L}_{31} \frac{p}{p_e} \frac{\partial \ln p}{\partial \psi} + \mathcal{L}_{32} \frac{\partial \ln T_e}{\partial \psi} + \mathcal{L}_{34} \alpha \frac{1 - R_{pe}}{R_{pe}} \frac{\partial \ln T_i}{\partial \psi} \right) \tag{2.18}$$

with the poloidal current ($I(\psi)$), the ratio of electron pressure to total pressure R_{pe} and four factors $\mathcal{L}_{31}$, $\mathcal{L}_{32}$, $\mathcal{L}_{34}$, and α depending on various plasma parameters. An analytical set of equations describing these parameters based on numerical simulations has originally been provided by [17, 18] with a newer, more accurate version available in [19]. Typical values for these parameters are $\mathcal{L}_{31} = \mathcal{L}_{34} \sim 0.5$, $\mathcal{L}_{32} \sim -0.2$, $\alpha \sim -0.5$, and $R_{pe} \sim 0.5$. Based on this it can be seen, that the largest contribution is generated by the pressure term. For this reason, the simplification

$$j_{BS} \propto \frac{\sqrt{\epsilon}}{B_\theta} \nabla p \propto q \nabla p \tag{2.19}$$

is commonly used. The $\sqrt{\epsilon}$ term here comes from the trapped particle fraction. The second approximation uses the fact, that under the assumption of constant toroidal field the inverse B_θ dependency can be roughly approximated as a q dependency.

2.4 Turbulent transport

Turbulent transport, also called anomalous transport, since historically it was unclear, why the transport was considerably higher than expected from classical and neoclassical theory, describes the transport caused by fluctuations in the plasma. These fluctuation originate from micro-instabilities [20, 21] that arise, once a critical gradient of density or temperature is exceeded. The instabilities create macroscopic structures, which are capable of transporting heat and particles. In the following, two micro-instabilities relevant to this work will be presented. It should be mentioned, that this does not present an exhaustive discussion of micro-instabilities in general.

2.4.1 Drift wave

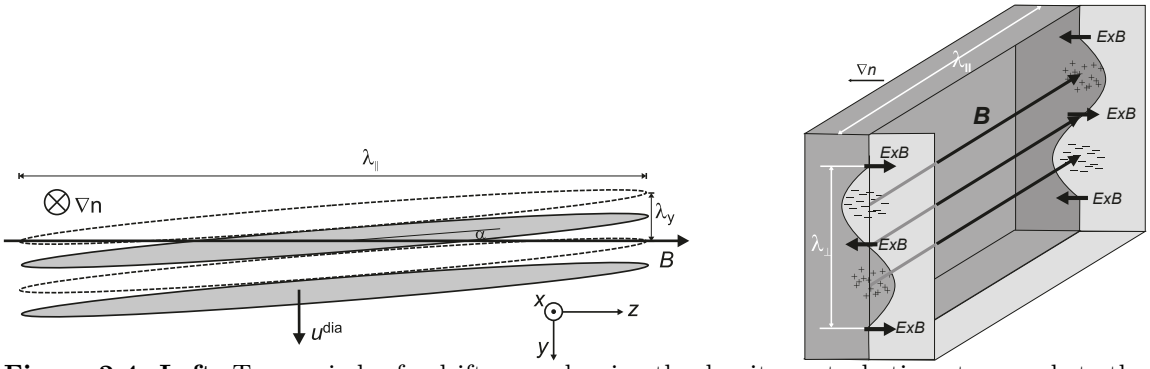

Figure 2.4: Left: Two periods of a drift wave showing the density perturbation at an angle to the magnetic field **Right:** The mechanism driving a drift wave, darker areas represent a higher density [G]

[22] For a drift wave to arise, a three dimensional density perturbation with a component both parallel and perpendicular to the magnetic field (see figure 2.4 left) needs to be present in the homogeneous magnetic field along a field line. If this perturbation is fast with respect to the diamagnetic drift speed of the ions, but slow with respect to the diamagnetic drift speed of the electrons, the electrons move to the region with lower density, while the ions stay behind, creating a potential difference through charge separation and thereby an electric field. The resulting $E \times B$ drift leads to a radial drift outwards. This behavior is shown in figure 2.4, right. Once again, the electrons move to the region of lower density, thereby causing the density and potential perturbation to be in phase. The radial drift therefore only leads to

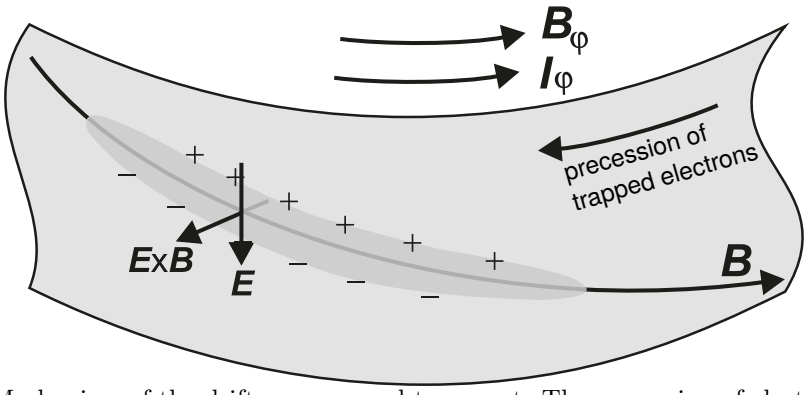

Figure 2.5: Mechanism of the drift wave caused transport. The precession of electrons leads to a charge separation across the perturbation (in darker gray) that causes a drift radially outwards [G]

a movement of the entire perturbation downwards in the electron diamagnetic drift direction, but not to a radial transport.

So far, an ideal response of the electrons was assumed. In a tokamak, this is however not the case as collisions and trapping of electrons affect this behavior. The main actor is the toroidal precession of the electrons (see section 2.3), which causes a charge separation across the initial perturbation, which reinforces it and leads to an outwards drift of particles as visualized in figure 2.5. This behavior is called Trapped Electron Mode (TEM).

2.4.2 Interchange instability

[22] For an interchange instability, an initial perturbation of the temperature along a field line is required. This is shown by the two differently shaded areas in figure 2.6. As the curvature drift of particles, which points upwards for ions, is dependent on the temperature, this perturbation leads to an accumulation of ions at the higher to lower temperature boundary and a reduction of ions on the lower to higher temperature boundary. The resulting modulation in ion density creates an electric field, and therefore a ExB drift pointing outwards. On the HFS, this drift thereby points against the initial perturbation, stabilizing it. However on the LFS, it points along the perturbation (as ∇T is reversed) thereby reinforcing it and leading to outwards transport. This phenomenon is called toroidal Ion Temperature Gradient mode (ITG). An analogous Electron Temperature Gradient (ETG) mode does also exist. However, since the characteristic length scale of this instability is the Larmor radius, which is much smaller for electrons, it is usually less relevant.

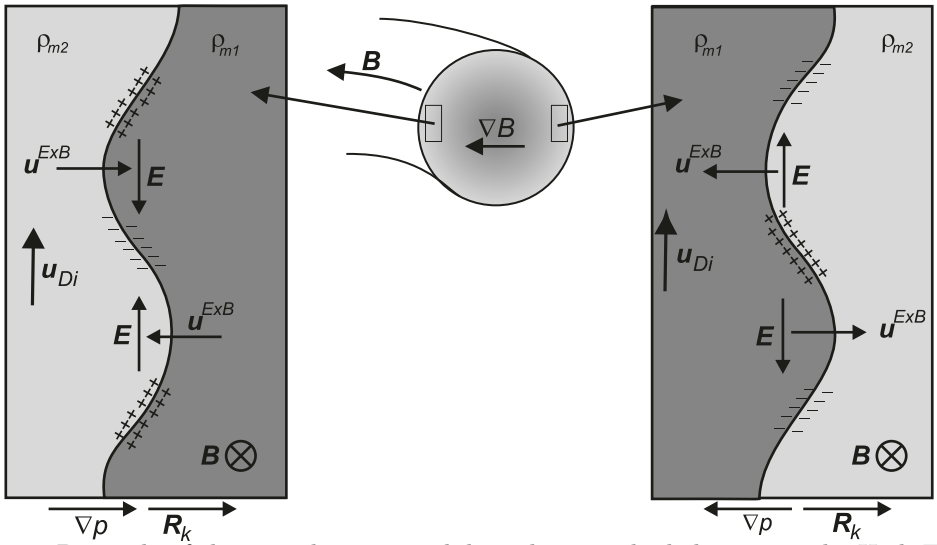

Figure 2.6: Principle of the interchange instability, showing the behavior on the High Field Side left and the Low Field Side right [G]

2.4.3 Critical gradients

As mentioned earlier, micro-instabilities only become destabilized and cause transport, once the driving gradient exceeds a threshold. This threshold is called the critical gradient. In the example of the ITG mode, the relevant parameter is the ion temperature gradient. To be precise, from linear gyrokinetic theory follows, that the actual dependency is the normalized temperature gradient [23]. The effect on the transport is that once the threshold is exceeded, a mode becomes unstable, leading to a strong increase of the heat flux outwards. This behavior is visualized in figure 2.7. The energy loss incurred by this process leads to a situation, where a slight increase in temperature gradient leads to a strong increase in outwards

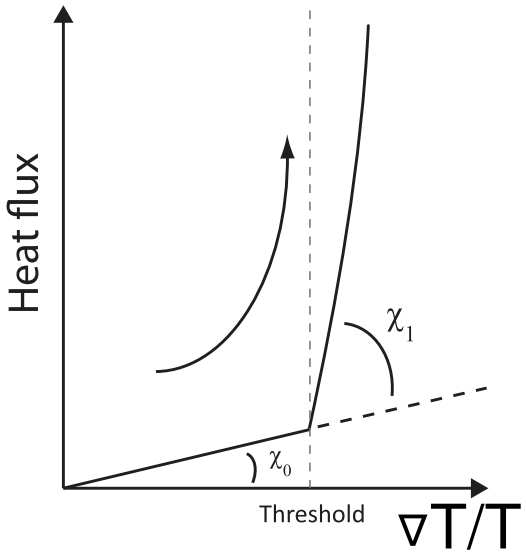

Figure 2.7: Outwards heat flux as a function of temperature gradient; Once the critical gradient is exceeded, a significant increase in transport can be seen (figure adapted from [H])

heat flux. The heat conductivity can then be described by

$$\chi = \chi_0 + \chi_1 \cdot \max(L_T^{-1} - L_{T,crit}^{-1}, 0) \tag{2.20}$$

Here $L_T = (|\nabla T|/T)^{-1}$ is the normalized temperature gradient length. Once the critical value $L_{T,crit}$ is exceeded, the heat conductivity, previously given by χ_0, is dominated by the much larger χ_1 term. To achieve temperature gradients beyond this threshold, increasingly larger amounts of input power would be required, eventually becoming unrealistic. This behavior limits the achievable temperature gradients. In the experimental case the temperature gradient, balanced by external heating, is usually located at or slightly beyond the threshold throughout a large part of the radial profile. It is therefore difficult to change the temperature gradient inside the plasma. This behavior is called "profile stiffness" [24].

2.5 Bohm/gyro-Bohm transport scaling

Starting from classical conductivity, the velocity of the particles between collisions can be assumed to be equal to the thermal velocity ($v_{th} = \frac{k_B T}{m}$), if the collision frequency is large as compared to the gyrofrequency. In this case, the diffusion resulting of a random walk can be described as

$$D = \frac{(\Delta x)^2}{\Delta t} = v^2 \cdot \Delta t = \frac{v_{th}^2}{\nu} \tag{2.21}$$

This term is maximized, when the collision frequency is equal to the gyrofrequency ($\omega = \frac{q_{el} B}{m}$). In this case, the resulting diffusion coefficient is given by

$$D = \frac{v_{th}^2}{\omega} = \frac{k_B T}{q_{el} B} \tag{2.22}$$

First discovered in [25], it has been found, that a Bohm-scaling $D \propto \frac{T}{q_{el} B}$ can be used to describe some diffusion processes in a tokamak plasma.

The thermal diffusion coefficient in a plasma based on dimensionless analysis can be written as [26]

$$\chi = \chi_0 F(x_1, x_2, x_3, ...) \tag{2.23}$$

where χ_0 is some transport coefficient with the correct dimension, and x_n are local dimensionless parameters. It has been found, that a Bohm scaling is a reasonable

choice for χ_0 [27, 28]. To separate the effect of large scale and small scale turbulence, the normalized gyroradius ($r_L^* = r_L/a$) is treated separately, yielding

$$\chi = \chi_{\text{Bohm}} \cdot (r_L^*)^\alpha \cdot F(x_1, x_2, x_3, ...) \tag{2.24}$$

with χ_{Bohm} being the transport coefficient resulting from Bohm-diffusion. Here, the case of $\alpha = 0$ is called Bohm scaling and the case of $\alpha = 1$ is called gyro-Bohm scaling [29]. Numerical simulations show, that transport can be described by local effects (using a gyro-Bohm scaling) once the minor radius surpasses ~ 300 gyroradii, whereas global effects (using a Bohm scaling) have to be considered otherwise [30]. Based on experimental results, it has been found that

$$F = cq^2(L_T^*)^{-1} \tag{2.25}$$

where L_T^* is the temperature gradient length normalized to the minor radius and c is a free parameter produces a good agreement [26]. Note that the q in this equation is the safety factor.

While both a Bohm, as well as a gyro-Bohm scaling can be used to describe individual scenarios, experience shows that they tend to break down, once different machine sizes or different heating setups are considered. In order to overcome this issue, using a mixed Bohm/gyro-Bohm setup can better describe the overall plasma behavior [31].

The model, applied to describe transport in this work, is based on the mixed Bohm/ gyro-Bohm setup, the exact formulas used are provided in section 5.3

2.6 The High confinement mode

First discovered [32] on ASDEX, the high confinement mode (H-mode) features an improved performance compared to the previously used low confinement mode (L-mode). Its distinguishing feature is the presence of a so-called "pedestal" in the plasma temperature and density close to the edge: In a small region close to, but inside the separatrix, the turbulence and thereby the transport is strongly suppressed, leading to a region of much larger gradients in the otherwise stiff profiles (see section 2.4.3). This allows reaching much higher values for temperature and density in the core. [33]

The H-mode can be accessed by increasing the power, crossing the separatrix above a certain threshold [34], although the exact mechanism behind it is not yet fully understood. Once the threshold is surpassed, a Transition from L-mode to H-mode (L-H transition) occurs.

Accompanying the H-mode is an instability called the Edge Localized Mode (ELM). ELMs are MHD instabilities, driven by the pressure gradient in the pedestal. In a repeating fashion, the pressure increases, thereby increasing the bootstrap current. Once a threshold is reached, an ELM-crash occurs, expelling heat and particles from the plasma, allowing the process to restart. These ELMs do have benefits, as they generate transport of impurities outwards, which may otherwise cause radiative losses in the core, degrading plasma performance. They do however cause a major issue for future reactor operation, as they generate transient heat loads on the divertor every time a crash occurs, which are likely above material limits, requiring strategies to avoid or mitigate them. [35]

As the processes governing the plasma confinement are not yet fully understood, an empirical scaling was created on the basis of large databases to evaluate the confinement of any particular discharge. Commonly used is the IPB98(y,2) [36] scaling:

$$\tau'_{E,th} = 0.0562 I_p^{0.98} B_{tor,0}^{0.15} P_{loss}^{-0.69} \bar{n}^{0.41} M^{0.19} R_0^{1.97} \epsilon^{0.58} \kappa^{0.78} \tag{2.26}$$

with the toroidal magnetic field at the major radius $B_{tor,0}$, the line averaged density $\bar{n}$, the loss power P_{loss}, the average ion mass M and the plasma elongation κ. Comparing this scaling with the performance achieved in a discharge, one arrives at the IPB98(y,2) confinement factor (H_{98}):

$$H_{98} = \frac{\tau_E}{\tau'_{E,th}} \tag{2.27}$$

with the measured energy confinement time of the discharge τ_E.

A newer version of equation 2.26, which includes more data, leading to a better confinement scaling H_{20} [37] is available. This scaling features a reduced importance of the line integrated density and the major radius as well as the inverse aspect ratio. It introduces a dependency on the triangularity and slightly increases the dependency on the ion mass. As this quantity is not yet implemented in the data evaluation on ASDEX Upgrade (AUG), and plans for DEMO still use H_{98} [38], this work uses the older version.

2.7 Plasma instabilities

Operation of the plasma inside a tokamak is limited by various instabilities. A selection of the relevant ones for the purpose of this work is presented in the following. The instabilities are usually located at a location in the magnetic equilibrium, where they are resonant. This location is characterized by their poloidal mode numbers m,

describing the amount of poloidal periods in one circumference and the analogous toroidal mode number n. This then yields a resonance at the flux surface, where $q = m/n$.

For ideal modes, the magnetic topology is conserved, while for resistive modes, tearing and reconnecting of magnetic field lines is allowed.

2.7.1 Sawteeth

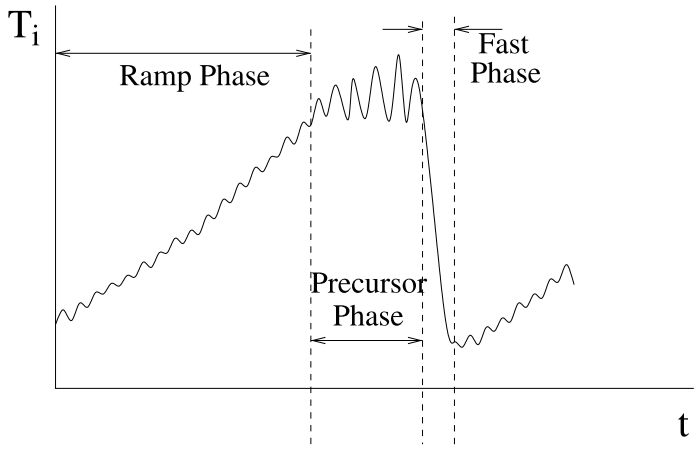

Figure 2.8: One period of a sawtooth oscillation: After some time of temperature ramp-up, a mode appears, which causes a fast crash, repeating the cycle [I]

The sawtooth instability [39] got its name from introducing a characteristic sawtooth like shape into the time evolution of the core temperature. A sketch of its build-up is shown in figure 2.8. Following a slow build-up of the core temperature (ramp-up phase), a mode appears, which can be seen growing (precursor phase) before a fast collapse is observed, redistributing energy outwards, where the temperature increases outside the so-called inversion radius at q=1, before this pattern repeats. The sawtooth instability is only present if a q=1 surface is present in the plasma and is linked to the appearance of a m/n=1 mode. While some details regarding the exact mechanism of the sudden drop remain unsolved, the commonly used explanation is as follows: The increase in electron temperature (T_e) increases the conductivity, leading to a local increase of the current and thereby a reduction of q. At some point, the mode at the q=1 surface becomes unstable, leading to a reconnection event, redistributing the current and bringing q back to one. During this process, particles are expelled outwards.

In general sawteeth are undesirable, as they degrade the performance of the plasma and can trigger seeds for other instabilities.

2.7.2 Ideal modes

In equilibrium, the magnetic pressure from the field lines is balanced by the kinetic pressure. If a perturbation now leads to a kink in the plasma, the magnetic pressure is locally increased, while the kinetic pressure stays the same. This leads to an unstable situation, where the plasma response reinforces the initial perturbation. Figure 2.9 shows a schematic of the working principle. The presence of a field along the plasma current contributes a stabilizing term, as the perturbation will bend it, leading to a restoring force through field line tension.

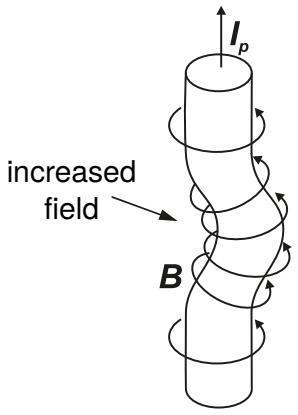

Figure 2.9: Principle of the kink instability. An initial perturbation leads to an increased field, reinforcing the perturbation (figure based on [G])

For external kink modes, the initial perturbation happens at the plasma edge. For a tokamak, assuming simple geometry and low β, it can be derived, that the resonant surface of this mode needs to be outside the plasma. A system is therefore stable with respect to modes, whose resonant surface lies inside the separatrix. In the β=0 approximation, the instability condition is given by:

$$\frac{m}{n} > q_{\text{edge}} = \frac{2\pi a^2 B_{tor}}{\mu_0 R_0 I_p} \tag{2.28}$$

These modes are especially unstable, if a strong current gradient is present near the edge, which can be the case during the current ramp up.

A special case is the $m = 1$ mode, with respect to which a tokamak plasma is especially unstable. For $n = 1$ the condition given by equation 2.28 is even sufficient, leading to the Kruskal-Shafranov-limit of $q_{\text{edge}} > 1$ mentioned in section 2.1.3. While it can by stabilized through active control, the $m = 2$ mode is sufficiently unstable to limit typical tokamak experiments to $q_{\text{edge}} > 2$.

For an internal kink mode, the perturbation happens inside the plasma, with the external shape being unperturbed. These modes are generally stable for $m > 1$. As the external shape is unperturbed, the perturbation has to drop to zero at some point inside the plasma. A 1/1 mode can be unstable if $q_0 < 1$ and corresponds to a displacement of the plasma inside the q=1 surface. This mode is commonly attributed to be the origin of sawteeth (see previous section).

It can be shown, that for $q > 1$, an interchange mode as introduced in section 2.4.2 is stable by itself, since the stabilizing contribution from the HFS outweighs the destabilizing contribution from the LFS. This is known as the Mercier criterion

[40], and is usually fulfilled, since regions below q=1 are also unstable to the internal kink, which limits their existence via the sawtooth instability. However, if one allows the mode to be not exactly on its resonant surface, while a stabilizing contribution from field line bending is introduced, multiple modes can now generate a situation, where interference reduces the amplitude in the stabilizing region and increases it in the destabilizing region. A schematic view of the resulting behavior is shown in figure 2.10.

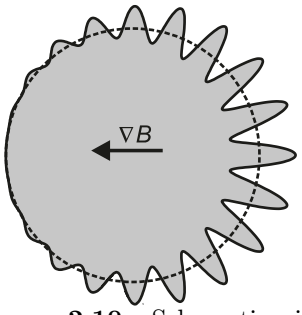

Figure 2.10: Schematic view of a ballooning instability. Starting from the initial flux surface shown by the dotted line, interference of interchange modes leads to a strong deformation at the Low Field Side [G]

While the assumption of coupling modes contradicts the localization on a resonant surface, in the limit of $n \to \infty$ the distance of the surfaces goes to zero. The stability is then governed by a balance between a stabilization due to field line bending and a destabilization through the pressure gradient. From the stability of this mode, a marginally stable pressure profile can be generated, which sets an idealized β limit, although the ultimate limit (mentioned in section 2.1) is lower and set by the finite β version of the external kink.

In the finite β case, an additional term has to be considered for the external kink instability. This creates a situation, where an external kink with its resonant flux surface inside the plasma can become unstable. The stability criterion is then given by

$$\beta' r \ll \left(\frac{m}{nq}\right)^2 (m^2 - 1) \tag{2.29}$$

resulting in the β limit mentioned in section 1.2. This mode is especially unstable in regions with low shear and large pressure gradient. Unfortunately both of these conditions coincide with the operating region of AT-scenarios, where a high pressure gradient and elevated q-profile, which is usually slightly reversed in the center, leading by default to the existence of an area with zero shear, are desirable to maximize bootstrap current. Therefore the β-stability in these cases is usually lower.

In addition, for sufficiently large pressure gradient in a region of low shear, external kink modes with $n > 1$ can also be unstable. These so-called "infernal" modes can further reduce the stability limit.

It should be mentioned, that introducing a conducting wall close to the plasma introduces a stabilizing contribution, possibly allowing to increase the β-limit beyond the traditional value presented in section 1.2. This effect is however not relevant to this work, since the scenarios of interest require large wall clearance and the AUG

vessel is not designed to act as a conducting wall. [8, 9]

2.7.3 Neoclassical Tearing Modes

The existence of a current sheet (see figure 2.11, left), which is a situation, where neighboring field lines point in opposite directions is possible in a tokamak due to the helical magnetic configuration.

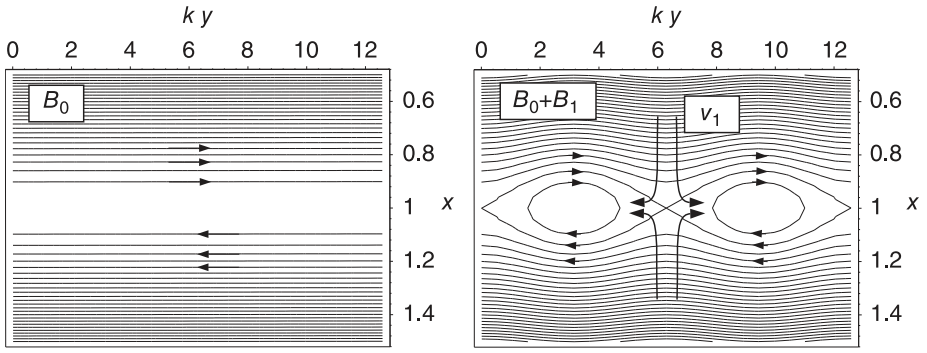

Figure 2.11: left: Magnetic field lines in opposite directions next to one another, forming a current sheet; **right:** Magnetic island structure after reconnection, the four arrows in the middle show the plasma flow [E]

The magnetic shear creates an effective helical field with changing sign across the respective flux surfaces. This allows for a situation, where the free energy of the system can be reduced by tearing (hence the name Tearing Mode) and reconnecting the field lines to form magnetic islands (see figure 2.11, right). The point of maximum width of the island is called O-point, while the point of minimum width is called the X-point, which is also the location where plasma can flow into the island. Integrating over the perturbed helical flux caused by the island from both sides generates a discontinuity across the island, indicating a surface current. This current determines the classical stability of the island.

When taking neoclassical effects into account (therefore Neoclassical Tearing Mode (NTM)), further effects appear. For an island to grow, an initial seed island needs to be present. This usually happens via some other instability, the most common cause is a sawtooth crash (see section 2.7.1). The existence of an island leads to a flattening of the kinetic profiles, since radial transport happens parallel to field lines of the island instead of requiring perpendicular transport which is much smaller. For positive magnetic shear, the resulting decrease of the bootstrap current density leads to an increase in island size, creating an unstable situation. At the same time, a high magnetic shear reduces the region, where $q \sim m/n$, generating a

stabilizing contribution. The island will grow until the classical contribution stabilizes it. The behavior of the resulting growth rate is shown in figure 2.12. It can be seen, that β has a significant influence over the mode stability, maximum island size and minimum seed island size.

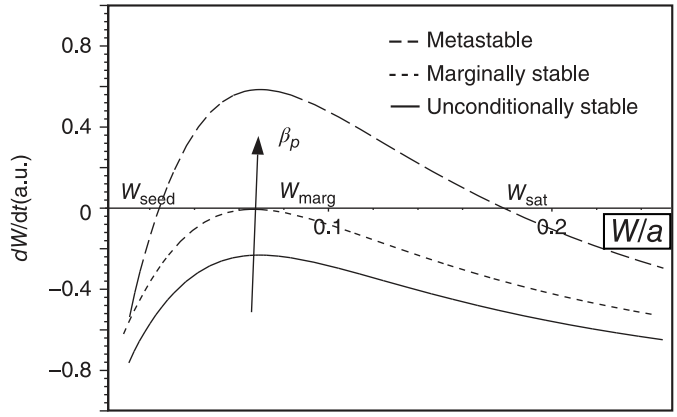

Figure 2.12: NTM growth-rate as a function of island size (W) for different values of β [E]

The flattening of the particle and temperature profiles leads to a loss of core temperature and density as the profiles are essentially shifted inwards (see figure 2.13). Depending on the size of the mode, this can lead to a significant loss of stored energy. As modes with higher mode numbers are generally further outwards, they have a larger effect on the total plasma. If an island grows large enough, it can lock to the intrinsic error field of the device, destabilizing the entire plasma and usually causing a disruption.

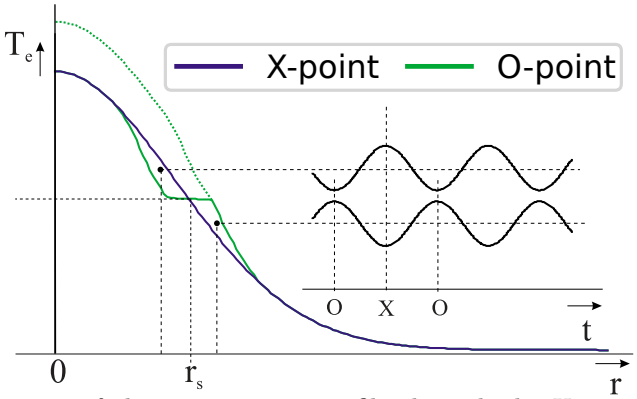

Figure 2.13: Comparison of the temperature profile through the X-point and through the O-point. The green dashed line shows the profile if the mode were not present. The Insert shows the temperature time evolution as it would be measured at the two locations indicated by the points (figure adapted from [41])

Figure 2.13 shows a comparison between a profile through the X-point and trough the O-point. Also shown is a profile without the mode present. The insert shows, what would be measured at the indicated radial positions, assuming the mode to be rotating. When measuring at a sufficient amount of locations, the phase difference between the two curves can be used to localize the mode.

As NTMs are essentially driven by a "hole" in the bootstrap current, one commonly used mitigation strategy is to use external heating systems (see section 3.3) to drive sufficient current to remove that hole. The common and most successful approach uses Electron Cyclotron Current Drive, which can also be used on ASDEX Upgrade to suppress the initial mode growth [42].

2.7.4 MARFE

A Multifaceted Asymmetric Radiation From the Edge (MARFE)[43] is a radiation-driven thermal instability, that can appear if the density at the edge surpasses a threshold, which depends on the impurity concentration and the input power. It can be characterized as a cold, high density region, initially located at the HFS. The increase in density causes a drop in temperature due to energy loss from ionization and radiation of neutrals entering the plasma. This strong increase in radiation leads to a situation, where a significant amount of the energy in the plasma is radiated away. Counteracting this is the heat-conductivity parallel to the magnetic field. A MARFE usually appears close to the X-point, where the potentially radiating volume is largest. As the heat conductivity depends on the temperature, if the energy loss becomes strong enough, a temperature gradient can appear along one flux-surface. While keeping the energy loss equal to the parallel heat flux, achieving a stable situation with this phenomenon is possible and has potential applications for heat exhaust solutions [44]. If the particle loss through recombination exceeds the input from parallel convection, a pressure hole develops. This situation is unstable, as the diamagnetic current along the pressure contour in the inhomogeneous magnetic field causes advection towards the HFS. If the MARFE grows large enough, it can trigger a disruption. [44]

The drop in electron temperature can have a significant impact on the rest of the plasma, where the reduction propagates to the plasma core, similar to NTMs. As a MARFE is essentially caused by insufficient heating, it can be removed by increasing the heating power.

Chapter 3

Experimental setup and diagnostics

3.1 ASDEX-Upgrade

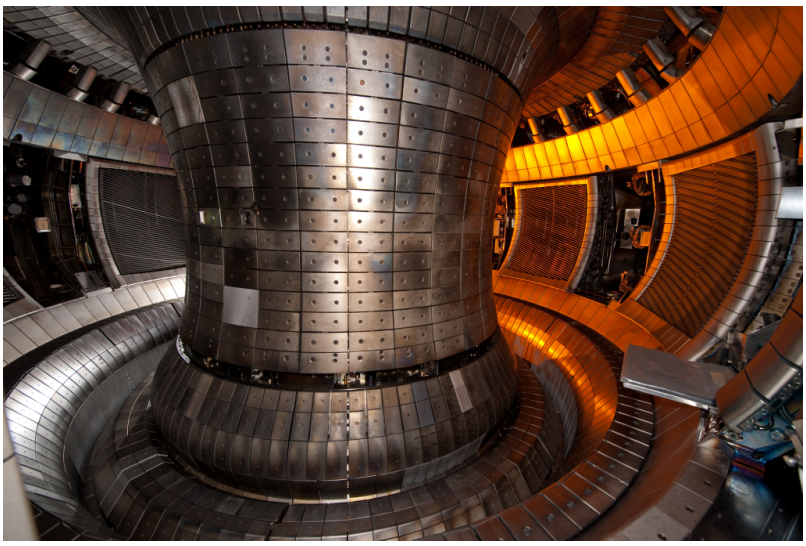

Figure 3.1: Photo of the inside of the ASDEX Upgrade vessel [K]

ASDEX Upgrade (short form of: **A**xially **S**ymmetric **D**ivertor **EX**periment, usually further shortened to AUG) is a medium sized tokamak operated by the Max-Planck-Institute for Plasma Physics in Garching near Munich, Germany. Built in the late 1980s, it has been operating since 1991 as a successor to the ASDEX tokamak,

which was the first device employing a divertor geometry (see section 2.1.2) thereby discovering the H-mode (see section 2.6). Figure 3.1 shows a view of the inside of the machine.

While originally built as a machine with the plasma-facing components made from graphite, by 2007 AUG had been upgraded, replacing the graphite by tungsten. Tungsten features superior resistance to erosion by the plasma, has a very high melting point and does not significantly react chemically with hydrogen. This makes it an attractive candidate for a future fusion reactor. The downside is that as a very high Z element it is not fully ionized, even at temperatures that are found in the core of the plasma. Consequently it radiates, thereby cooling the plasma. For this reason measures have to be taken limit the tungsten impurity content and avoid accumulation in the core.

AUG has a large variety of diagnostics to evaluate the plasma performance and, compared to its size, it has a very high amount of heating power. The components of AUG, which are relevant in the framework of this thesis, are discussed in more detail in the following sections.

3.2 JET

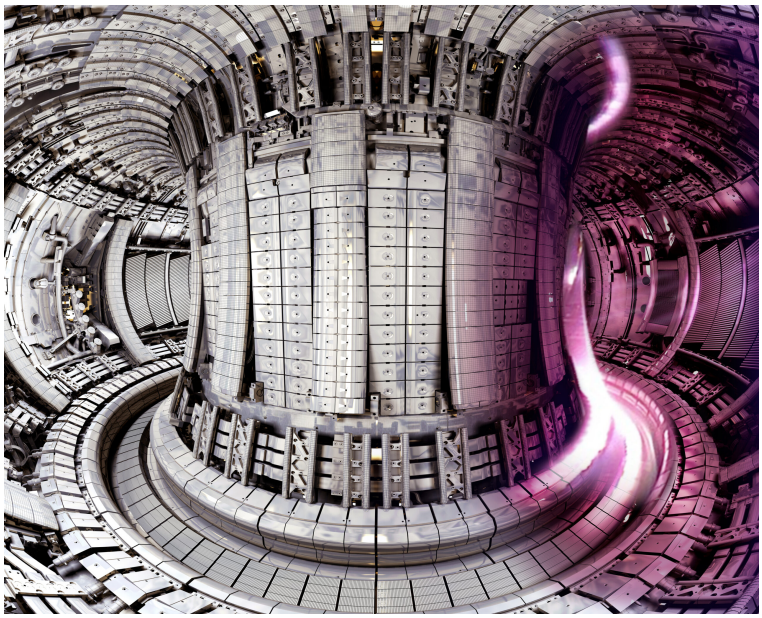

Figure 3.2: Picture of the inside of the JET vacuum vessel with superimposed images of a visual light camera during a discharge on the right side [L]

The Joint European Torus (JET) is the largest tokamak in operation at the time of writing. Located at the UKAEA campus in Culham, UK, it is operated by a European collaboration through the EUROfusion program. Figure 3.2 shows a view of the inside of the machine.

Starting operation in 1983 with plasma-facing components from carbon and without a divertor, JET has been upgraded with a divertor in the early 90s and with beryllium/tungsten plasma-facing components in 2010. This setup allows for studies with reactor-relevant geometry and materials. Since it is the only tokamak that can currently operate D-T plasmas, it holds the records for both fusion energy and peak fusion output.

While it has a smaller amount of diagnostics, due to the much harsher conditions caused by neutrons emerging from the fusion process and less heating power compared to its size than AUG, the similar geometry and plasma facing components qualify JET as a good candidate for comparisons with a much bigger machine.

A comparison of the most important machine parameters is shown in table 3.1. An explanation of the NBI and ECRH heating systems will be given in following sections. The ICRH heating system has no relevance to this work and is only mentioned for the sake of completeness. While it does have a higher amount of heating power, the much larger size of JET leads to a considerably lower heating power per volume.

	R	r	V	B_{max}	I_{max}	P_{NBI}	P_{ICRH}	P_{ECRH}
AUG	1.6m	0.5m	$13m^3$	3.2T	1.4MA	20MW	6MW	8MW
JET	3m	0.9m	$90m^3$	4T	5MA	34MW	10MW	-

Table 3.1: Comparison of major radius (R), minor radius (r), volume (V), maximum magnetic field strength (B_{max}), maximum plasma current (I_{max}) and heating power (P_{NBI}, P_{ICRH}, P_{ECRH}) between AUG and JET

3.3 Heating systems

In order to achieve sufficiently high temperatures for fusion at a realistic machine size and to emulate the effects of fusion born alpha particles heating the plasma, usage of external heating systems is required. The systems relevant to this work are presented in the following, although it should be mentioned that this list is far from being exhaustive in terms of possible heating approaches. Of those, the AUG tokamak uses Neutral Beam Injection and Electron Cyclotron Resonance Heating, while the JET tokamak only uses Neutral Beam Injection.

3.3.1 Neutral beam injection

The concept of Neutral Beam Injection (NBI) consists in the generation of a beam of highly energetic neutral particles and to shoot it into the plasma.

A gas source (usually deuterium) is first ionized by a low-power plasma. The resulting ions are then accelerated by a strong electric field, before being shot through a neutral gas target, where charge exchange reactions neutralize the fast particles. As the initial particles are not always fully ionized, a distribution of multiple energy levels, depending on the charge state of the initial particles is generated. The resulting beam is sent through a magnetic field to eliminate particles that have not been neutralized, before injecting it into the plasma. The neutralization step is necessary as charged particles could not penetrate the magnetic field of the plasma.

In the plasma, the particles are ionized again and become so-called fast ions, with their speed larger than the background plasma. The rate of this ionization depends on the plasma density, the beam energy and to a lesser extent the plasma temperature. Particles that are not ionized are essentially lost, passing through the plasma and hitting the wall (so-called shine-through), which can force a beam to shut down if the target becomes too hot.

These fast-ions then follow the magnetic field lines. They interact with the plasma via collisions, leading to a slowing down of the fast ions, transferring energy to lower energy particles. At the same time, collisions can transfer momentum, broadening the pitch. An example for a resulting fast ion distribution is shown in figure 3.3 for a simplified example of a point source and only one energy level.

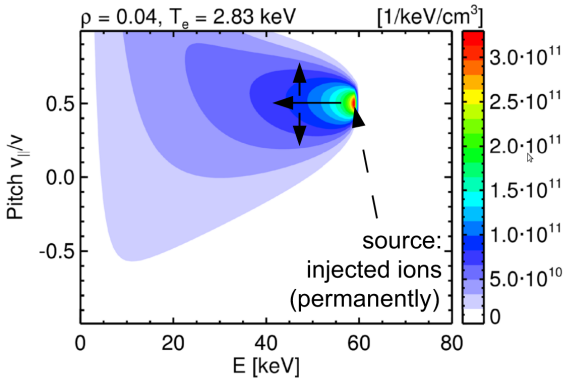

Figure 3.3: Fast ion distribution of a single point-like source [45]

In reality, not all particles stay on their initial flux surface, but depending on their parallel velocity some of them enter trapped banana orbits. For a particle starting at the outside of such an orbit, this effectively leads to a broadening of the source towards the plasma center.

Integrating over the slowing down term, the heating power can be calculated

resulting in the flux surface averaged energy loss [46]

$$\left\langle \frac{dW}{dx} \right\rangle = -\frac{c_1 A Z^2 \ln\Lambda}{W} \sum_j \frac{n_j Z_j^2}{A_j} - c_2 \frac{Z^2}{A^{1/2}} \frac{n_e \ln\Lambda}{(kT_e)^{3/2}} W^{1/2} \tag{3.1}$$

where A and Z are the injected ion atomic mass and charge, the index j refers to the particles in the plasma, W is the beam energy, $\ln\Lambda \sim 17$ is the Coulomb logarithm, $c_1 = 1.3 \cdot 10^{-13}$ and $c_2 = 2.28 \cdot 10^{-15}$. This equation assumes the injected ions to be of the same charge state. While high energy ions transfer their energy dominantly to electrons, lower energy ions increasingly transfer energy to the plasma bulk ions. The fraction of energy given to ions G_i is given by

$$G_i = \frac{W_{\text{crit}}}{W} \int_0^{W/W_{\text{crit}}} \frac{dy}{1+y^{3/2}} \tag{3.2}$$

with the critical energy where the same amount of energy is given to electrons and ions

$$W_{\text{crit}} = 14.8 k T_e \left(\frac{A^{3/2}}{n_e} \sum_j \frac{n_j Z_j^2}{A_j} \right)^{2/3} \tag{3.3}$$

If injected with a component parallel to the magnetic field, NBI introduces a Neutral Beam driven current (NBCD). Since the neutral particles are being ionized when they hit the plasma, and the ions retain their speed considerably longer than their electrons due to their higher mass, a current is driven in the direction of the injected beam. The resulting current can be calculated by integrating the fast ion distribution over the pitch and velocity resulting in [47]

$$I_{\text{fi}} = Z I_0 \frac{v_0 t_s}{2\pi R_0} \xi_0 I(x,y) \tag{3.4}$$

with the injected particle current I_0, the injection velocity v_0, the initial pitch angle ξ_0, a pitch angle scattering parameter $I(x,y)$ (see [47]) and the Spitzer slowing down time [46]

$$t_s = 6.28 \cdot 10^8 \frac{(kT_e)^{3/2} A}{Z^2 n_e \ln\Lambda} \tag{3.5}$$

While electrons being pulled along do generate a shielding effect, since trapped electrons cannot participate, a net current remains. This can be described by introducing an additional factor, leading to the total current given by

$$I_{\text{nbcd}} = I_{\text{fi}} \left(1 - \frac{Z}{Z_{\text{eff}}} (1 - G(Z_{\text{eff}}, \epsilon)) \right) \tag{3.6}$$

with the effective ion charge Z_{eff} (see section 3.4.4), and a trapped electron parameter G, depending on Z_{eff} and the inverse aspect ratio ϵ. This calculation neglects neoclassical effects, charge exchange reactions, and effects of injected particles of different charge state. A more complete formulation can be found in [48]. While the driven current does depend on the temperature, since it also depends on the trapped particle fraction, which is larger off-axis, the efficiency of NBCD does not drop strongly off-axis. [45, 49]

NBI at AUG

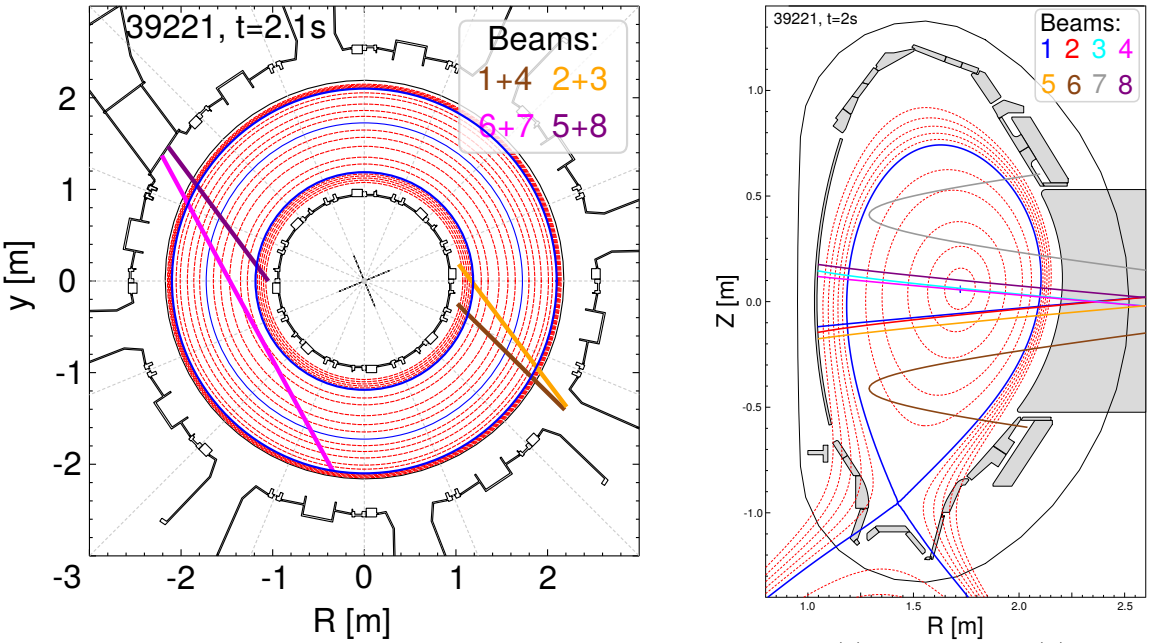

Figure 3.4: Path of the neutral beam system in AUG in a toroidal (a) and poloidal (b) cross-section

AUG features two neutral beam injectors with four beams each. Every beam has a power of 2.5 MW for a total heating power of 20MW [50]. The geometry of the beams in the plasma is shown in figure 3.4. Beams 6 and 7 have a considerably longer path through the plasma and are capable of generating significant amounts of current drive both on- and off-axis. Owing to the smaller toroidal contribution of the other beams, those are driving considerably less current. Due to the poloidal setup, this current is driven more closely to the magnetic axis. An example of the neutral beam driven current in AUG, as calculated by RABBIT in ASTRA (see section 5.1), is displayed in figure 3.5. Note that in the actual discharge not all beams were running.

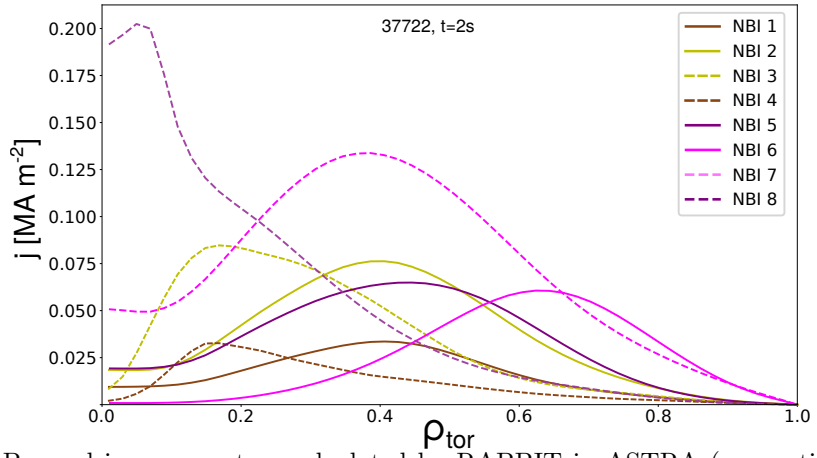

Figure 3.5: Beam driven current as calculated by RABBIT in ASTRA (see section 5.1) for an AT-discharge

The increased current drive of beams 6 and 7 can clearly be seen. While beams 2 and 5 still have a considerable off-axis contribution, the other ones are peaked much closer to the axis or are much less efficient at driving current.

In principle, every beam can operate for an entire discharge. However, in low density plasmas, especially for the beams with a shorter path, part of the particles can travel through the plasma, hitting the inner wall. If these target locations become too hot, the respective beam is deactivated to protect the machine. For technical reasons, beam number 7 was not available for a significant part of this work.

NBI at JET

Similar to AUG, JET has two neutral beam injectors. Those feature a set of eight beams each, with a nominal heating power of ∼2.1MW per beam for a total heating power of ∼34MW. In principle the beams can run for 20s, which is longer than required or used for any of the discharges considered during this work. In reality however, depending on the plasma density, limits are in place, both with respect to the maximum length and to the maximum power in order to prevent potential damage to the machine [51].

A schematic view of the NBI-system is shown in figure 3.6. Similar to AUG some of the beams are injected tangentially, allowing for an increased current drive. An example for the resulting beam driven current, as calculated by RABBIT in ASTRA (see section 5.1), is shown in figure 3.6b. Note that in the actual discharge not all beams were running. Similar to AUG some beams with a deposition off-axis can be seen. Notably, the current driven per beam is lower, since the power is reduced due

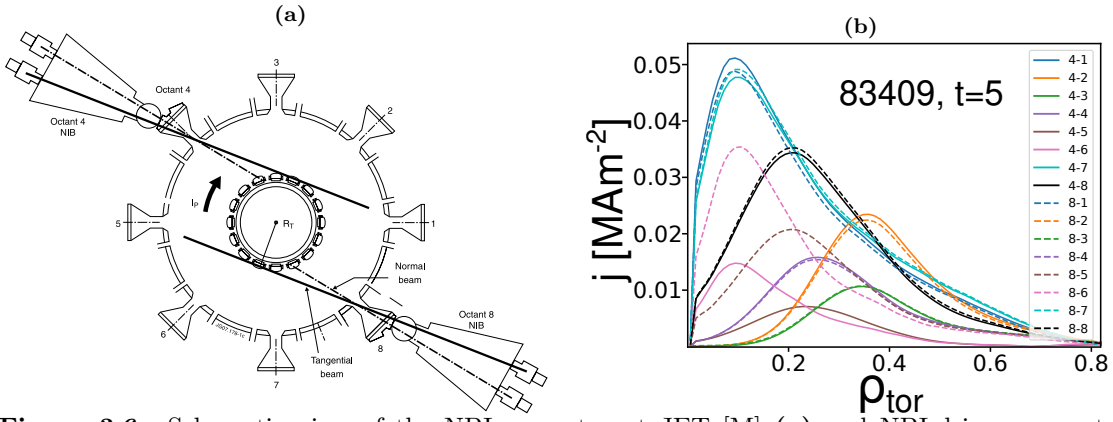

Figure 3.6: Schematic view of the NBI geometry at JET [M] **(a)** and NBI-driven current as calculated by RABBIT in ASTRA **(b)**

to the example discharge operating at low density.

Simulation

In order to simulate NBI, the time evolution of the fast ion distribution generated by the beam(s) needs to be solved. To this end, the source, collisions and orbit effects need to be considered. This can be done to a very good accuracy with Monte-Carlo codes such as NUBEAM [52], at the cost of high computational times. Alternatively, the Rapid Analytical Based Beam Injection Tool (RABBIT) [45] uses a simplified beam geometry, simplified orbit effects, and describes collisions based on the Fokker–Planck equation that can be calculated mostly analytically, to achieve a much faster run time while preserving most of the accuracy. For this reason RABBIT is used for NBI calculations in this work.

3.3.2 Electron Cyclotron resonance heating

Electron Cyclotron Resonance Heating (ECRH) deposits power into the plasma through waves of a frequency equal to the cyclotron frequency of the electrons

$$\omega_c = \frac{eB}{m_e} \tag{3.7}$$

or harmonics of it. At a resonance location, the waves are absorbed, transferring their energy to the electrons, thereby heating them. Due to the considerable mass difference, energy transfer from electrons to ions is inefficient, causing ECRH to

mainly heat electrons, although this efficiency increases at higher density. Since the resonance frequency and thereby the location in the plasma is dependent on the magnetic field, and ECRH is typically injected with rather low width microwave beams, it allows for a localized heat deposition. Depending on the density of the plasma, the refractive index can become smaller than zero, i.e. the wave is reflected. These regions are inaccessible to ECRH, one speaks of a cut-off. To get around this, higher harmonic frequencies of ω_c can be used. In the following, a brief description of ECRH and the resulting current drive will be provided, a more comprehensive explanation can be found in [53].

If the injection path includes a component parallel to the magnetic field, the Doppler effect needs to be taken into account. Including also the relativistic contribution, the resonance condition for the l'th harmonic is given by

$$\omega = \frac{l\omega_c}{\gamma} + k_\parallel v_\parallel \tag{3.8}$$

where γ is the Lorentz factor ($\gamma = \sqrt{1 - v^2/c^2}$) for $v^2 = v_\parallel^2 + v_\perp^2$, and $k_\parallel = \omega n_\parallel / c$ is the component of the wave vector parallel to the magnetic field with the refractive index parallel to the magnetic field $n_\parallel$. This equation can be rewritten as

$$\frac{v_\perp^2}{v_\parallel^2} = \left(1 - \frac{\omega^2}{l^2\omega_c^2}\right)\frac{c^2}{v_t^2} + 2n_\parallel \frac{\omega^2}{l^2\omega_c^2}\frac{c}{v_t}\frac{v_\parallel}{v_t} - \left(1 + n_\parallel \frac{\omega^2}{l^2\omega_c^2}\right)\frac{v_\parallel^2}{v_t^2} \tag{3.9}$$

where v_t is the relativistic thermal velocity. The solution to this equation is an ellipse in velocity space, centered around the origin, if the wave is injected fully perpendicular to the magnetic field. Depending on the sign of $k_\parallel$, this ellipse is shifted away from $v_\parallel = 0$, causing only electrons moving in one direction to be heated. This behavior is sketched in figure 3.7, where the red ellipse shows the resonance condition.

The electrons fulfilling the resonance condition are accelerated towards higher $v_\perp$, which is the direction of the gyrating motion (indicated with the blue arrow in the figure). The energy transfer in this process depends on the phase of the gyromotion relative to the wave. Thus in principle the same amount of particles are accelerated as are decelerated. This picture does however not take the fact into account, that the velocity distribution of the electrons can be assumed to be Maxwellian, meaning there are more low energy electrons than high energy electrons. Therefore this process reduces the amount of low energy electrons in favor of high energy electrons. These higher energy electron thermalize through collisions, thereby heating the plasma.

Since preferentially electrons traveling in one specific direction are heated, for $k_\parallel \neq 0$ a current is driven in addition. This process is called Electron Cyclotron

Current Drive (ECCD) and has two contributions. If the accelerated particles move up far enough in velocity space, they can enter the region, where the mirror condition (equation 2.14) is fulfilled, becoming trapped particles. This removes their contribution to the toroidal current, since trapped particles cannot fully revolve around the torus, generating a net electron flow in the opposite direction of $v_{\parallel}$. This process is called Ohkawa current drive [54].

If the electrons do not enter the trapping region in the velocity space, they still contribute to the current. Since collision rate scales with v^{-3}, higher velocity particles take longer to slow down via collisions. As only electrons traveling in one direction are accelerated, this process leads again to a current drive. This second process is called Fisch-Boozer current drive [55].

The current drive efficiency depends on the ratio of electron temperature to electron density. As for typical plasmas the electron temperature is more peaked than the density, this yields a reduction in efficiency towards the edge. Additionally, as the trapped particle fraction increases towards the edge, the competition between the two current drive processes leads to a further reduction.

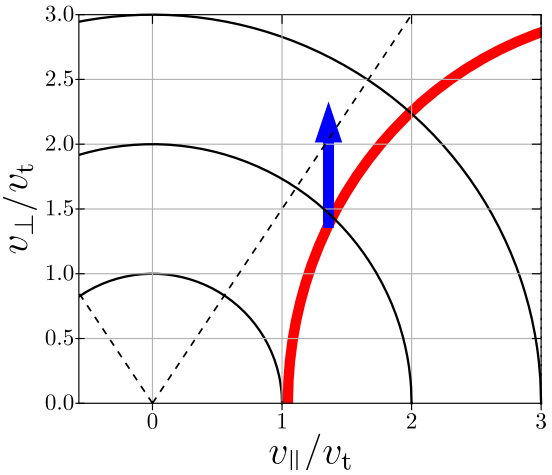

Figure 3.7: Velocity space diagram of ECRH; Shown in red is the resonance condition for the particles, here for a case with non-zero $k_{\parallel}$; The blue arrow indicates the movement of electrons to higher $v_{\perp}$ in this case for Ohkawa current drive

ECRH at AUG

AUG features an ECRH system [56] [57] with eight gyrotrons with a power of up to 1MW each for the entire length of a discharge. All of these sources are injected into the machine via steerable mirrors, that can be moved even during a discharge. This allows for precise control over the position of the resonance location. The same system also allows to change how much current is driven, enabling to reduce it effectively to zero and to adjust the direction of the current drive. In order to protect the machine from stray radiation, which is caused by the non-absorbed power of the ECRH system, a suit of detectors is present to shut down systems, if this power gets too high. Additionally, if the measured temperature in a gyrotron becomes too high,

or a substantial drop of the output power is detected, indicating a problem with the gyrotron, individual systems are switched off to protect them.

Simulation

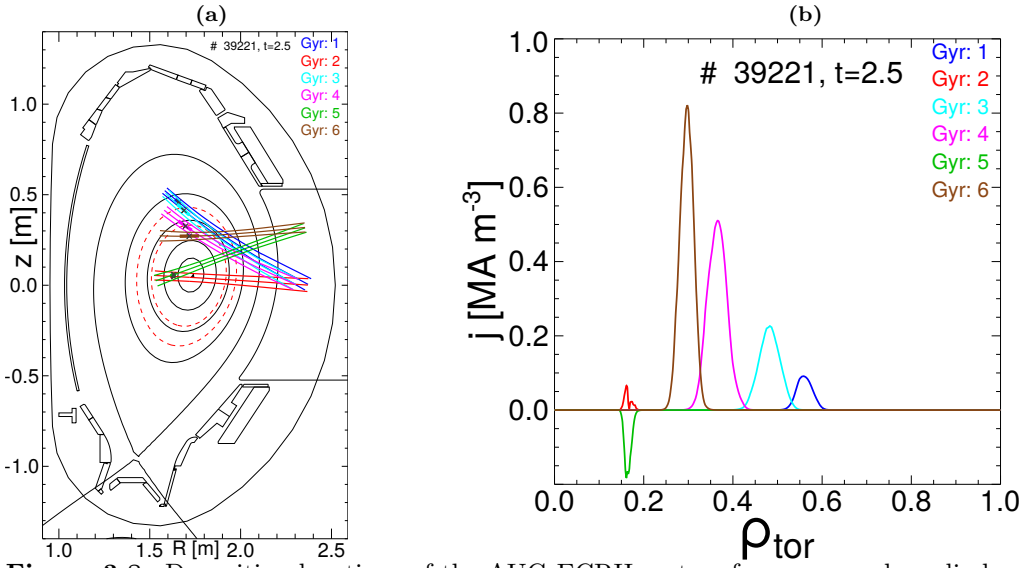

Figure 3.8: Deposition locations of the AUG ECRH system for an exemplary discharge **(a)** in a cross-section view and corresponding driven current **(b)** as calculated by TORBEAM

The beam tracing code TORBEAM [58] is capable of calculating the propagation and absorption of a Gaussian electron cyclotron beam for arbitrary launching position and angles for a given plasma equilibrium. To this end, a set of ordinary differential equations, describing the propagation of the beam axis and the evolution of the curvature and amplitude profiles of the beam front due to diffraction, is solved numerically. Using this code, the current drive and deposition location can be calculated based on the launching angles. The results for an exemplary discharge are shown in figure 3.8a, showing the AUG cross section and the deposition locations of the respective systems. Note that not all systems are active. Figure 3.8b shows the corresponding driven current. The drop in efficiency, when going outwards can clearly be seen. Note that these systems are operating at the same $k_{\|}$. The two gyrotrons closest to the core (at $\rho_{tor} \sim 0.15$) are setup not to drive current.

3.4 Diagnostics

In order to gain information about the processes happening inside the plasma, tokamaks are equipped with a large set of diagnostics systems, measuring a large variety of different parameters. As providing a complete overview on these systems is beyond the scope of this work, only the systems measuring the plasma quantities of interest will be introduced in the following. An overview on the AUG system is displayed in figure 3.9, showing the location of the respective systems in a top-down and poloidal cross section view. Since the working principle of these systems is the same at JET, explicit examples are only given for the AUG system.

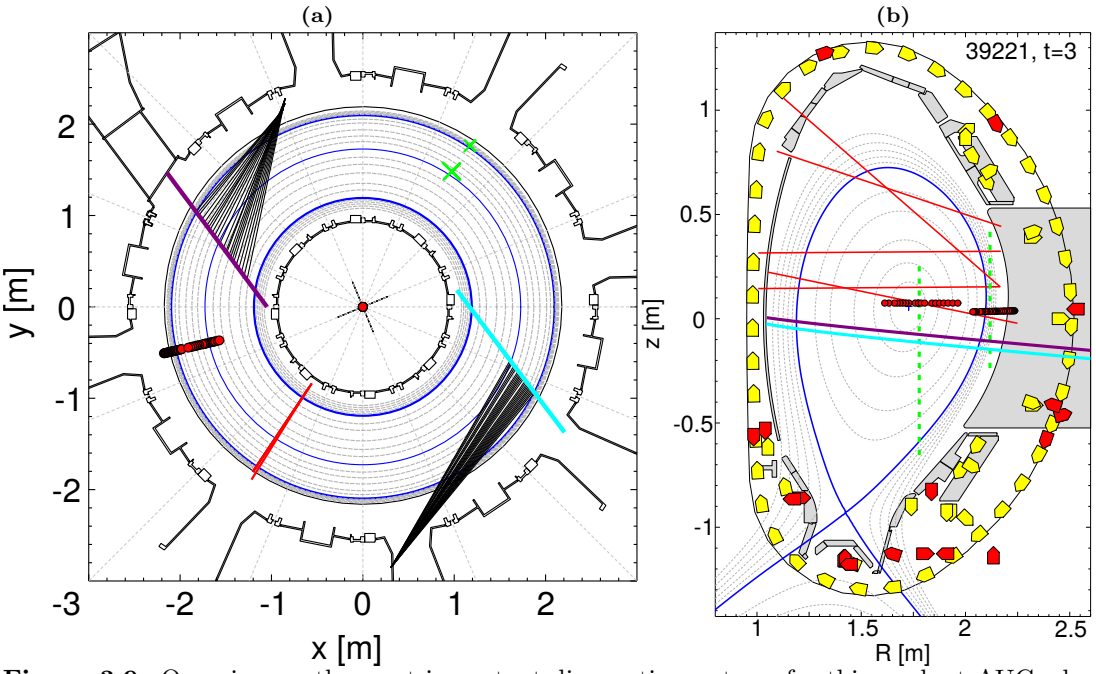

Figure 3.9: Overview on the most important diagnostics systems for this work at AUG, showing a top-down toroidal view **(a)** and a poloidal cross-section **(b)**; Visible in both are the DCN-paths (red), the ECE measurement locations (red circles), the NBI-systems observed by the CXRS-system (cyan and purple), and the TS-lines (green), the toroidal view also shows the CXRS sightlines, the poloidal view shows the location of the magnetic probes (yellow) and the manometers (red boxes)

3.4.1 Electron cyclotron emission

While waves at the cyclotron frequency can be used to heat electrons, due to the permanent acceleration through their gyromotion they also emit at this frequency.

This process is called Electron Cyclotron Emission (ECE) As already mentioned in section 3.3.2, the frequency depends on the location in the plasma. Assuming the plasma is optically thick for this frequency, meaning its density is sufficient for practically all of the radiation to be reabsorbed by neighboring electrons, essentially all of it is emitted as black-body radiation. In tokamak plasmas this condition usually holds at the cyclotron frequency. The emission intensity can then be approximated by the Rayleigh-Jeans law:

$$I = \frac{\omega_c^2 k_B T_e}{8\pi^3 c^3} \tag{3.10}$$

As this intensity is dependent on the temperature, a system measuring at frequencies corresponding to different positions in the plasma can infer profiles of the T_e [59].

A NTM causes a flattening of the temperature profile through its O-point, while the gradient is mostly maintained through its X-point (see figure 2.13), and is rotating along with the plasma in front of the detector. This leads to an almost sinusoidal perturbation of the measured temperature, which results in a 180° phase-jump between channels inside and outside the mode. For this reason, such a phase jump can be utilized in order to determine the location of the mode [41].

The ECE at AUG measures 80 channels (see red dots in figure 3.9), leading to a spacial resolution of $\sim$ 1cm at a sampling rate of 1MHz [60].

3.4.2 Thomson Scattering

For Thomson Scattering (TS) a high intensity laser pulse is sent through the plasma. Some of this light is then scattered by the electrons in the plasma and observed by several detectors along lines of sight perpendicular to the initial beam. Assuming a Maxwellian distribution of the electron velocity, the electron temperature at the intersection of the line of sight and the laser gives rise to the Doppler broadening of the measured spectrum. It can thus be deduced from the width of the peak ($T_e \propto \mathrm{FWHM}^2$). The intensity of the measured spectrum provides information on the electron density (n_e) at the same location ($n_e \propto I$).

AUG operates two Thomson systems (green in figure 3.9): One looking into the core and another one at the edge. These systems achieve a resolution of 25mm for the core system and 3mm for the edge system. Limited by the repetition rate of the lasers of 20Hz, the core system samples at 80Hz with four lasers and the edge system at 120Hz with six. [61]

3.4.3 Interferometry

A measurement of the line integrated electron density can be obtained by sending a laser beam through the plasma. Under the assumption of it being far from its cut-off, this beam then experiences a phase shift $\Delta\phi$ depending on the density along its path l:

$$\Delta\phi = \lambda \frac{e^2}{4\pi\epsilon_0 m_e c^2} \int n_e dl \tag{3.11}$$

with the electron charge e, the vacuum permittivity ϵ_0 and the electron mass m_e. This phase shift can be deduced from the interference pattern of the beam with an unshifted reference beam. As the phase shift depends linearly on the wavelength, usually high wavelength options are chosen to improve the signal to noise ratio. Using multiple lines of sight, density profiles can be constructed.

At AUG a Deuterium Cyanide (DCN) laser system is used. Using interferometry very fast measurements (sampling rate of 50kHz at AUG) can be obtained. [62]

In addition, the laser beam is also affected by the magnetic field parallel to its path, which is mostly the poloidal magnetic field if it travels in a poloidal plane. This magnetic field component gives raise to a rotation of the polarization of the laser beam, the so called Faraday rotation. The rotation angle is provided by

$$\gamma_f = \lambda^2 \frac{e^3}{8\pi^2\epsilon_0 m_e^2 c^3} \int n_e B_\parallel dl \tag{3.12}$$

and can be measured by a polarization detector or simply a detector behind a rotating slit.

3.4.4 Charge Exchange Recombination Spectroscopy

Charge Exchange Recombination Spectroscopy (CXRS) [63] uses the fact, that injected atoms (usually deuterium, D) of the neutral beam system (see section 3.3.1) interact with impurity ions (I^{Z+}) in the plasma via charge exchange reactions, transferring an electron.

$$D + I^{Z+} \rightarrow D^+ + I^{(Z-1)+*} \rightarrow D^+ + I^{(Z-1)+} + h\nu \tag{3.13}$$

The impurity ion is left in an excited state ($I^{(Z-1)+*}$), which emits radiation at a characteristic frequency (ν) when it decays back to the ground state ($I^{(Z-1)+}$). Using a set of lines of sight, the impurity ion temperature and density can be inferred in the same way as for Thomson scattering, where the Doppler broadening yields the temperature and the intensity the density. In addition, based on the Doppler shift

of the spectral lines when using a line of sight with a toroidal view, the rotation velocity can be deduced. Since it can be assumed that all main ion species are in thermal equilibrium, the impurity temperature can generally be equated to the main ion temperature. In principle, the same is also true for the rotation, as the impurities follow the flow of the main ions, although due to friction, their speed is slightly lower. From quasi-neutrality, the main ion density can be calculated under the assumption, that the density of each relevant impurity species is known. If this is more than one, multiple systems are required. It is then given by

$$n_i = n_e \frac{Z_{\text{eff}} - Z_{\text{imp}}}{1 - Z_{\text{imp}}} \tag{3.14}$$

with the impurity ion charge (Z_{imp}) and the effective ion charge (Z_{eff}),

$$Z_{\text{eff}} = \frac{\sum_k n_k Z_k}{n_e} \tag{3.15}$$

where k denotes the different species. If sufficient amounts of impurities are measured, Z_{eff} can be calculated directly. Usually, this is however not the case. The charge exchange data also includes information about the bremsstrahlung along the respective lines of sight [64]. If the values of the density and temperature are known, the effective charge can be calculated from this.

AUG operates multiple CXRS systems (see figure 3.9), looking at two different beams. These systems have a resolution of $\sim$ 2.5cm and usually integrate over 10ms, although faster rates are possible. A faster system, looking at the plasma edge is also available. [63, 65]

3.4.5 Magnetics

Information about the magnetic flux can be obtained by placing several coils around the torus. The voltage (U) induced into a coil of area A is given by

$$U(t) = -\frac{d\psi}{dt} = -\frac{d}{dt}\left(\int \vec{B} \cdot d\vec{A}\right) \tag{3.16}$$

By integrating this voltage over time, information about the magnetic flux (ψ) can be obtained. These coils are able to measure at a very high repetition rate (10kHz at AUG), allowing the detection of fast oscillations caused by rotating instabilities such as NTMs (see section 2.7.3) and providing information about the rotation frequency and growth rate of these modes. In addition, by analyzing the phase between coils located at different positions, the mode numbers can be determined.

3.4.6 Manometers

ASDEX-Upgrade features a set of linear hot cathode ionization manometers in order to measure the neutral pressure at various points in the machine. A cathode emits a stream of electrons, which are then accelerated, creating a current. These electrons interact with neutrals, ionizing them and creating an ion current. This current depends on the particle flux density, from which the pressure can be calculated if the thermal velocity is known. The measurement frequency is 2kHz. [66]

3.5 Data analysis

The various diagnostics systems presented in the previous sections have some overlap in so far as they measure the same parameter at a similar location, or use sight lines at different positions, that partially look at the same magnetic surface. In order to fully exploit the information provided by this portfolio of diagnostic systems, the data are mapped onto a common coordinate system, using a magnetic equilibrium (see section 3.5.2). Combining the data from the available sources improves resolution and increases reliability as it reveals inconsistencies between the systems.

3.5.1 Integrated data analysis at AUG

At AUG the Integrated Data Analysis (IDA) tool [67] combines data measured from the ECE, TS, DCN and Lithium-ion beam emission spectroscopy [68] to obtain T_e and n_e profiles. The combined uncertainty is estimated using a Bayesian approach. An additional source of uncertainty is the magnetic equilibrium used to generate the common coordinate system. The tool also includes forward modeling of the different diagnostics, to properly account for effects such as ECE shine-through, where the radiation is attributed to a different plasma position, if the plasma is not optically thick.

IDA calculates Z_{eff} based on the procedure presented in section 3.4.4. In a metal machine such as AUG, reflections from the wall and the divertor contaminate the Bremsstrahlung measurements. For this reason, usually only a few central lines of sight, chosen to minimize this contamination, are used for this calculation, yielding an average value for Z_{eff}, but no profile.

3.5.2 Equilibrium reconstruction at AUG

For a system mapping different diagnostics onto a common grid, a reconstruction of the plasma equilibrium is required. This is obtained by solving the Grad-Shafranov equation (equation 2.7) using numerical tools and the available data. At AUG, two such solvers are mainly used: The **C**ompLete **I**nterpretative **S**uite for **T**okamak **E**quilibria (CLISTE) [69] code obtains a solution by implementing a least squares fit to magnetic measurements. As magnetic measurements cannot provide reliable information about the core behavior, the reconstruction problem is underdetermined. In order to solve it, a regularization of both the pressure gradient and the poloidal current times its gradient is required, resulting in a solvable problem but a q-profile with a very large uncertainty.

Alternatively, the Integrated Data Equilibrium (IDE) code [70] generates additional constraints by using the pressure profile, obtained by the diagnostics and including the current diffusion equation [71]

$$\sigma_{\parallel}\frac{\partial\psi}{\partial t} = \frac{R_0 J^2}{\mu_0\rho}\frac{\partial}{\partial\rho}\left(\frac{G_2}{J}\frac{\partial\psi}{\partial\rho}\right) - \frac{V'}{2\pi\rho}(j_{bs} + j_{cd}) \tag{3.17}$$

describing how a plasma current distribution evolves with time. Here, $\sigma_{\parallel}$ is the parallel conductivity, J is dependent on the poloidal current inside a flux surface, and V' and G_2 are geometric factors. The bootstrap current j_{bs} is calculated self-consistently using the equilibrium and the experimental profiles. The externally driven current $j_{cd} = j_{\mathrm{ECCD}} + j_{\mathrm{NBCD}}$ is calculated by the TORBEAM (see section 3.3.2) and RABBIT (see section 3.3.1) codes coupled to IDE. If available, internal current measurements from the polarimetry system (mentioned in section 3.4.3) and the imaging motional stark effect diagnostic [72] can also be used to further constrain the results. When all diagnostics are available this produces a safety factor profile in very good agreement with the experiments and a very small error range. For the experiments carried out during this work, internal current measurements were not available. It has been shown in [73], that the behavior calculated by current diffusion fits well to internal measurements. While the error range increases significantly, the actually calculated value does not change systematically. Based on previous observations, a sufficiently precise description of the q-profile is expected. MHD-markers (mainly locations of modes) found during this work were found to be in good agreement with the profiles produced by IDE (see appendix A.5), and large MHD activity, that would lead to a redistribution of current not described by equation 3.17, is not present.

3.5.3 Equilibrium reconstruction at JET

The equilibrium reconstruction at JET is done with the Equilibrium FITting (EFIT) code [74]. The basic version only considers magnetics data as input with a significant regularization of q. As a result, the accuracy of the resulting q-profile is poor. A polarimetry system similar to the one at AUG is in principle available, but the resulting error range is still large. A version including internal measurements with a motional stark effect diagnostic [75] is available and produces high fidelity profiles. However, this diagnostics requires one specific neutral beam to be active and another one to be inactive to avoid contamination. Therefore it is not available in the early phase, where the q-profile is still developing, and not available at all, if the correct beam setup is not chosen. [76]

In principle, something similar to IDE could be done by using the simulation code TRANSP [77, 78] to provide a time evolution for the plasma safety factor and pressure profiles. These are then introduced as constraints in EFIT to generate an improved equilibrium. This process is then iterated until a sufficiently good result is produced. In contrast to IDE, this process is not automated, would require significant effort and is therefore usually not employed.

A code, which considers time evolution and produces a self consistent q such as IDE on AUG is not available. For this reason information about the q-profile could only be gained through MHD-markers, meaning the existence of modes, appearing in the magnetics and ECE diagnostics.

Chapter 4

Advanced Tokamak Scenarios

Advanced Tokamak (AT) scenarios have already been introduced in section 1.2.2. This chapter is devoted to a more thorough explanation and describes the actual operation of the various scenarios.

4.1 Background

As mentioned in section 2.1, the poloidal part of the magnetic field of a tokamak is mainly created by the plasma current. In conventional tokamaks, at least part of the plasma current is supplied by the central transformer coil. This is realized by decreasing the flux through said coil, which in turn induces a loop voltage at the edge of the plasma, driving the current. In this setup, the plasma essentially acts as the secondary winding of a transformer. Since the flux cannot be decreased indefinitely, even in a superconducting coil, eventually a limit is reached, forcing tokamaks into pulsed operation. The current induced in the plasma will be called "inductive current" throughout this work, although it is acknowledged that the term "ohmic current" is also commonly used.

As a starting point, figure 4.1a, shows the current distribution of an arbitrarily chosen low power H-mode discharge at AUG.

This constitutes a "worst-case scenario", where most of the current is driven inductively and contributions from the external heating systems are low. Reducing the fraction of the induced current, possibly allows for steady state operation, or would at least prolong the pulse duration. While driving the plasma current purely through external sources is in principle possible, maximizing the bootstrap current ($j_{bs} \propto q\nabla p$), which is proportional to both, the safety factor and the pressure gradient, is desirable, as it comes "for free". To this end, advanced scenarios actively

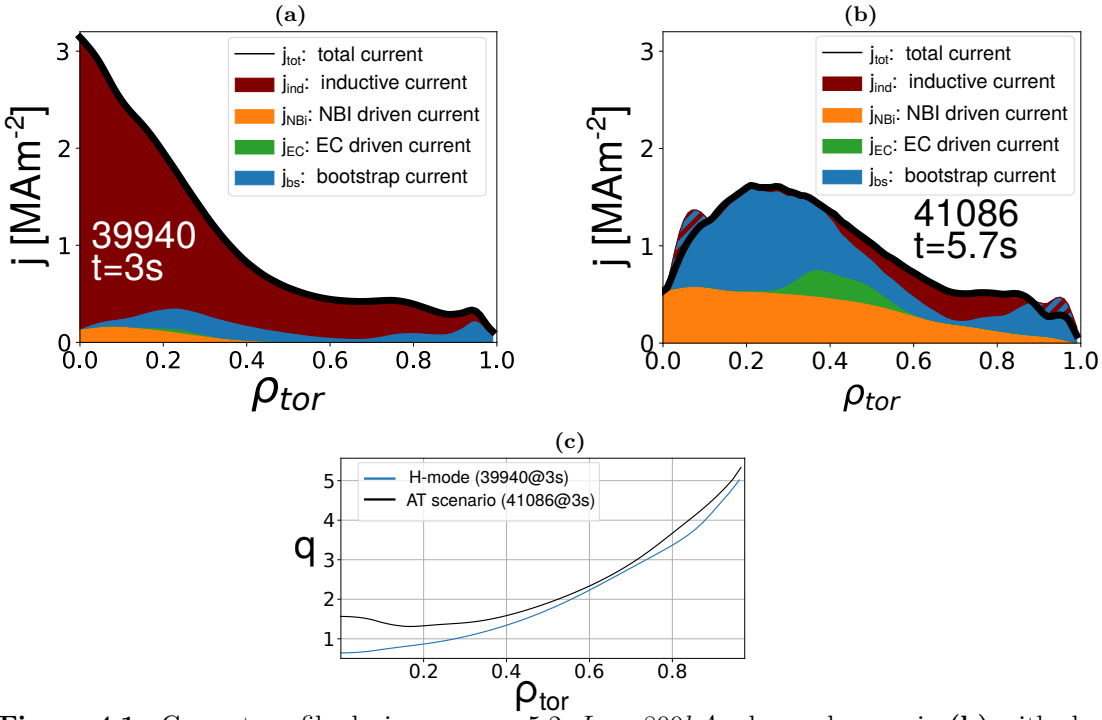

Figure 4.1: Current profile during a $q_{95} \sim 5.2$; $I_p \sim 800kA$ advanced scenario **(b)** with shaded regions denoting a negative contribution compared to the current profile in an arbitrarily chosen H-mode **(a)** and the corresponding q-profiles **(c)**

shape the q-profile to increase the bootstrap current. This is done by using the external heating systems to drive current, thereby altering the current profile, which impacts the poloidal magnetic field and thereby the bootstrap current. Increasing the safety factor from a behavior as is shown in figure 4.1c in blue (this corresponds to the current density profile in figure 4.1a) to the behavior shown in black allows to achieve a current distribution as is shown in the figure 4.1b, where a large part of the inductive current has been replaced by a combination of externally driven current and bootstrap current.

The negative inductive current (shown by the brown hatched area) region close to the core is a combination of a real contribution and uncertainty in the bootstrap current calculation. Due to the small plasma volume in the affected region, the impact of this phenomenon is low. The negative inductive current region close to the edge is a result of uncertainties in the pedestal data.

Raising the minimum of the q-profile (q_{min}) has the additional benefit of improved resistive MHD stability, when the resonant surface of low-helicity modes is no longer

present. The most notable effect here is the sawtooth instability (see section 2.7.1), which is no longer present if q_{min} stays above unity. Depending on the exact q-profile used, the magnetic shear can be reduced, especially around q_{min}, reducing the ideal MHD stability and thereby the β-limit (see section 2.7.2).

Increasing the bootstrap current can also be done by increasing the pressure gradient in the plasma, which can be done by raising the heating power. However, doing so by definition raises β bringing the plasma closer to its stability limit and making NTMs or ideal instabilities more likely to occur.

4.2 Late heating and early heating

Conventionally, the plasma in a tokamak is generated by decreasing the flux through the transformer coil until the induced loop voltage becomes sufficiently high for a breakdown to occur, where the neutral gas in the chamber ionizes, creating the plasma. The current through the plasma is then continuously increased, until a predefined value is achieved. The phase of constant plasma current is called flat-top. Starting from the edge, where the loop voltage is applied, the current diffuses inward during the ramp-up phase towards a peaked current profile where $j \propto \sigma \propto T_e^{3/2}$. This process happens on the timescale of the current diffusion time (τ_r). As the poloidal magnetic field is generated by the plasma current, it is small in the beginning, strongly increasing as the plasma current is increased. This leads to central values of q, that are very high in the beginning and then drop to a standard profile.

The simple option to transition into an advanced scenario setup is to wait for the plasma to reach a stationary state before applying additional actuators. This procedure is called "late-heating" and it usually means waiting for the plasma current to reach its maximum value.

The resulting behavior of q at a representative location around mid-radius is shown in figure 4.2 in blue for an example discharge. Also shown is the time, when the additional heating starts. The initial sharp drop in q stems from the ramp-up. As can be seen, even after the additional heating starts, some time is required before q starts rising again. The slope of this increase is dependent on the current diffusion time (see equation 3.17), which is at $\tau_r \sim 1.5$s for the example shown here. The resulting scenario is not optimal, since it looses a considerable part of the discharge length until interesting regimes are reached, but it is acceptable. A problem arises when extrapolating to future machines such as ITER or even a reactor, where current diffusion times are projected to be at $\tau_r \sim 350s$ (calculated based on estimations from [7]). This would lead to very long times, until a targeted scenario is achieved, making this approach not desirable.

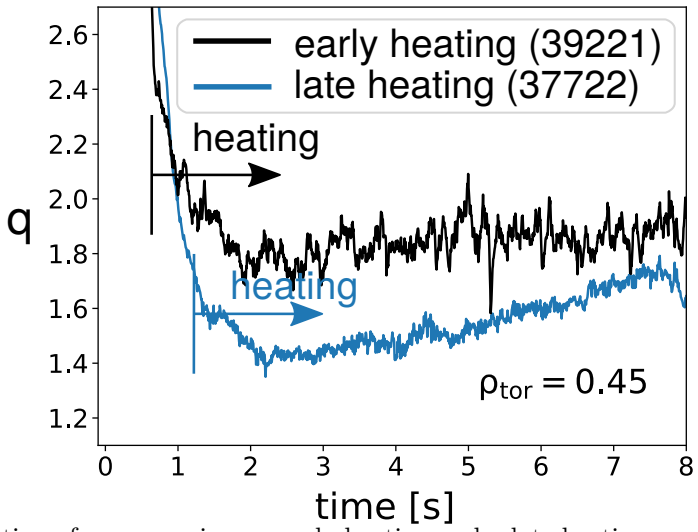

Figure 4.2: Evolution of q, comparing an early heating and a late heating case; Also shown is the time, when the first heating system is turned on

The alternative is to apply the additional heating while the plasma current is still below its maximum value. This approach is called "early-heating". Since the additional current drive affects q before it reaches its minimum, the intermittent drop can be avoided and the desired value can be achieved from above, rather than from below. An example for the evolution of q in such a case is shown in figure 4.2 in black. Additionally, the heating during the early phase increases the conductivity of the plasma and thereby the current diffusion time. The diffusion of the current into the center is thereby slowed down, leading to a broader current profile, which in turn leads to a higher q-profile.

In current day non-superconducting devices early heating scenarios are of interest to better utilize the limited discharge duration, while they might be required in future machines to reach an elevated q-profile in a reasonable amount of time.

The downside of the early heating approach is a high sensitivity to the exact timing of the heating and fueling systems. Further, the impact of initial conditions, which may not be fully known due to dependency on the exact machine conditions (meaning dependency on previous discharges) reinforces this problem. In addition to that, a reduced stability towards tearing modes (see section 2.7.3) in the early phase can lead to stability issues.

4.3 Hybrid vs advanced

As mentioned in the introduction, for scenarios departing from a mostly inductively driven current, one distinguishes between the hybrid scenario, where no shear reversal of the q-profile happens and it terminates at the axis slightly above one, and the advanced scenarios, where a shear reversal does occur and the minimum of the safety factor can be considerably above one.

Hybrid scenarios can be achieved with a lower amount of external current drive than AT-scenarios, as the required change to the q-profile is smaller. This makes them more interesting for machines, where the available power is a limiting factor. Further, the region of low magnetic shear at high pressure gradient is reduced, leading to a higher stability towards ideal modes and thereby usually a higher ideal β limit.

Advanced scenarios require a higher amount of current drive and, as mentioned previously, potentially current drive during the ramp up phase, leading to a more complex operation. Due to the higher requirement of external current drive, they are often operated at reduced plasma current, reducing the available confinement. The benefit is that the significantly higher q-profile causes the bootstrap current to make up a much larger portion of the plasma current, allowing for potentially fully or at least close to fully non-inductive operation [79]. In devices with large amounts of external current drive [80] as well as at rather low plasma current [81] steady state operation has been demonstrated. Another advantage is that increasing q_{min} completely eliminates the resonant surface of low helicity modes, potentially leading to an improved resistive MHD stability.

An additional potential benefit is that the existence of a shear reversal leads to formation of an Internal Transport Barrier (ITB) caused by a localized suppression of turbulence through the negative magnetic shear. A more in depth review of this process can be found in [82]. For the discharges considered during this work, the location of the shear reversal is close to the core, resulting in the affected volume being small enough to safely be ignored. It is however possible to generate ITBs at a location further outwards, enabling a considerable improvement of confinement in the core, allowing to potentially reach confinement values much larger than H_{98}=1 [83]. This increase in confinement can potentially counteract the reduction resulting of a reduced plasma current. The q-profile can then reach very large values inwards of the ITB, leading to discharges with a very high bootstrap current fraction [84]. The downside of this setup is, that a large pressure gradient associated with the ITB drives MHD instabilities, usually limiting their operation to lower β. An additional point of concern is the fact that an ITB limits transport of impurities outwards and could therefore potentially cause an issue related to impurity accumulation in the

core [85]. [86]

An interesting type of the hybrid scenario is the so-called flux pumping scenario: Here a dynamo effect caused by a 1/1 quasi-interchange mode [87, 88], which appears once a β threshold is exceeded, causes a redistribution of current outwards. As this mode becomes weaker for $q > 1$, it is self regulating to keep q close to one. This allows to apply current drive on-axis, where the efficiency is considerably larger, and it removes the necessity of active tailoring of the q-profile, qualifying it as an attractive approach for future operation. Experimental evidence of flux-pumping has recently been shown on AUG [89] and motivated experiments on JET, discussed in chapter 8.

4.4 Previous work on AUG and other machines

Both for ITER [90] and DEMO [91], operation in both hybrid or advanced regimes is considered, aiming for steady-state or at least increased pulse duration. This is important, as it allows for a reduction of cyclic loads on the machine and improves the economics by reducing down-time. For the reasons mentioned previously, early heating will likely be a requirement. Further, using a scenario with an increased bootstrap fraction as the target scenario has been identified as an option for reducing the size requirement of the central solenoid in DEMO, which would allow for a smaller machine and thereby lower complexity and cost [38]. So far however, only rather low bootstrap fractions ($f_{BS} < 40\%$) are considered due to a lack of validation cases with reactor relevant parameters [38]. For this reason, those scenarios are being studied in current day machines.

Some work on advanced scenarios has been carried out on most of the contemporary machines, such as JET , DIII-D, JT-60U, and EAST.

High confinement and bootstrap fraction have been demonstrated on DIII-D in a variety of scenarios and at relevant plasma current [92]. However as DIII-D features a carbon wall, some questions remain towards applicability in tungsten wall devices. The carbon wall also allows for operation much closer to the wall, since impurity influx from the wall is less of a concern. This allows to utilize the stabilizing contribution from the wall [93], which future devices may not be able to.

Using a current overshoot technique, i.e. a fast current ramp up followed by a small ramp down in order to achieve an elevated q-profile has been seen to produce an improved confinement at JET [94], but fails to achieve a very large bootstrap fraction.

Alternatively, it has been shown at JET, that strong heating in the early phase can lead to a strongly reversed shear, allowing for the formation of ITBs [95]. Using

this approach, a scenario with both very high confinement and bootstrap fraction has been demonstrated transiently on JT-60U [96].

While AUG still had a carbon wall in the past, the impact of variations of the current profile in the ramp-up phase has been studied [97]. Utilizing the early heating approach, a high confinement with a bootstrap current fraction around 40% at a relevant plasma current has been achieved [98]. Good confinement and a large non-inductive fraction in the presence of an ITB have also been demonstrated [99].

Operation of a very long pulse with high bootstrap fraction has recently been demonstrated at EAST [81], albeit at a rather low plasma current.

Both on DIII-D [100] and recently on AUG [89] good confinement and operation with a large non inductive fraction has been demonstrated, using the flux-pumping approach.

AUG is well positioned to study AT-scenarios in a full tungsten machine and at a high plasma current, due to its high ratio of external power to plasma volume. While early heating advanced scenarios have been studied on AUG in its carbon phase in the past, recent work [101, 102] has focused on the late heating approach due to the difficulties in scenario design. As will be shown in the following chapters, the modeling approach, developed during this work, is well positioned to reduce these difficulties.

While the model presented here does not include effects of ITBs, it could still be used to guide the path to a q-profile desirable for the effect to occur. As the model does not include effects of the flux pumping phenomenon, its divergence from experimentally measured profiles can potentially be used to identify the phenomenon by giving information about how the plasma would be expected to behave without it.

4.5 Experimental approach on AUG

As AUG is a full tungsten machine, tungsten influx into the plasma through sputtering from the wall can become an issue since tungsten does not fully ionize, even in the core, leading to significant radiative losses [103]. This effectively sets a minimum on the density in order to keep the tungsten fraction in the core sufficiently low. As a mitigation measure, the plasma facing components of AUG are regularly coated with boron, which has been shown to significantly reduce the sputtering of tungsten [104].

As the current drive scales inversely with the plasma density, AT scenarios preferably operate at low collisionality in order to maximize the available current drive. To achieve relevant performance at low density, operation shortly after the boronization

is necessary. Tungsten inflow through sputtering is further reduced by setting up the plasma shape in a way as to have a large wall clearance (see figure 2.2).

It was found in [105], that the global confinement depends on the divertor neutral density ($n_{0,div}$), which is correlated with the separatrix density. For this reason, $n_{0,div}$ is kept as low as possible and fueling is done via feed-back control on it.

In order to avoid an ELM-free phase after the L-H transition, which usually leads to problematic tungsten accumulation in the core [106], the pedestal pressure needs to be large enough for the ELM-stability to be sufficiently low to cause ELMs. As the heating power in the low collisionality case triggers the L-H transition at a relatively low value, sufficient fueling needs to be provided to achieve the target ELM-frequency, putting a lower limit on the plasma fueling and thereby density. This is particularly relevant in tungsten devices, where the wall stores fewer particles, than in a carbon machine. The resulting behavior is visualized in figure 4.3 showing the evolution of the line integrated density of the outermost sightline of the DCN interferometer for a set of discharges. Note that all of these discharges have one NBI beam starting at $t = 0.65$s and a second one at $t = 0.85$s. The clearly visible oscillations are caused by ELMs and after they disappear (timing marked with vertical lines) a strong density increase can be seen. The figure shows the difference between failed and successful cases: The discharges in orange and red start out with insufficient density, causing an ELM-free phase to appear. The discharge in black has an increased density after $t \sim 0.65$s, but this drops back to a value comparable to the orange case at $t \sim 0.8$s,

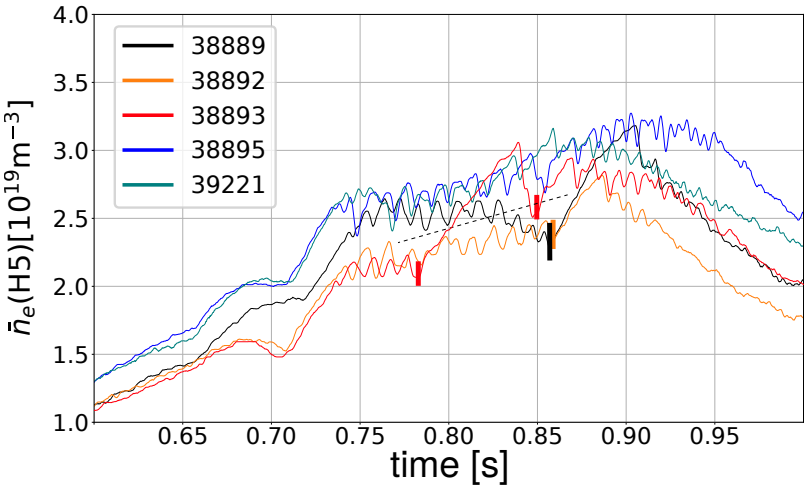

Figure 4.3: Line integrated density measured by the outermost line of sight of the DCN interferometer (see figure 3.9b). The clearly visible oscillations are caused by ELMs and when they stop (marked with vertical lines), a strong density increase can be seen. The black dashed line acts as a guideline showing the separation between cases with and without an ELM-free phase

causing an ELM-free phase to appear. The discharges in blue and teal have more fueling from the beginning, as is visible by the density offset from the beginning and do not show an ELM-free phase, indicating them being above the threshold. The black dashed line acts as a rough indication of this threshold, based on the discharges shown here.

When the density becomes too large, before sufficient heating is applied a MARFE (see section 2.7.4) can appear, which puts an upper limit on the density. The range in which a stable H-mode can be achieved is thereby limited. For the case considered here this limit is not a large concern as it is desirable to keep the $n_{0,div}$ and thereby the density low. It can however happen, if there is more fueling than intended for technical reasons. Unfortunately, a clear and consistent precursor could not be seen in the available diagnostics for the cases considered here.

As central heating by ECRH has been shown to reduce impurities in the core [107], at least one gyrotron is used for central heating during the stationary phase of the plasma. To ensure sufficient off-axis current drive to reach relevant q-profiles, one of the off-axis sources is operated for the entire duration of the discharge. ECRH is used to do adjustments to the q-profile, or to do NTM suppression [42] by pointing at the respective flux surface of the mode of interest.

Chapter 5

Model

In this chapter, the system used for the simulations for this work will be presented. Note that most of the results shown here have already been published in [108]

5.1 ASTRA

The Automated System for Transport Analysis (ASTRA) [71, 109] is a transport code capable of simulating the behavior of a tokamak plasma by calculating flux surface averaged kinetic profiles from the axis to the separatrix. This is done by solving 1D fluid transport equations. Additionally, ASTRA is coupled to the 2D Grad-Shafranov equilibrium solver SPIDER [110], to provide a self consistent equilibrium. Due to this coupling of 1D and 2D parameters, ASTRA is usually referred to as a 1.5D code. Starting from an initial set of profiles that have to be provided as inputs, the user can specify if and which profiles are evolved. For the kinetic profiles, a transport model has to be provided from external sources. For the external heating sources, the RABBIT (see section 3.3.1) and TORBEAM (see section 3.3.2) can be coupled for NBI and ECRH heating and current drive respectively. In order to evolve the current and q profiles, ASTRA solves the current diffusion equation (see equation 3.17) assuming a neoclassical behavior of the bootstrap current as described in [17].

5.2 Model setup

A model has been created within the ASTRA framework to simulate the behavior of the relevant parameters, aiming at assisting in the design of experimental scenarios. Figure 5.1 shows a schematic overview of the model.

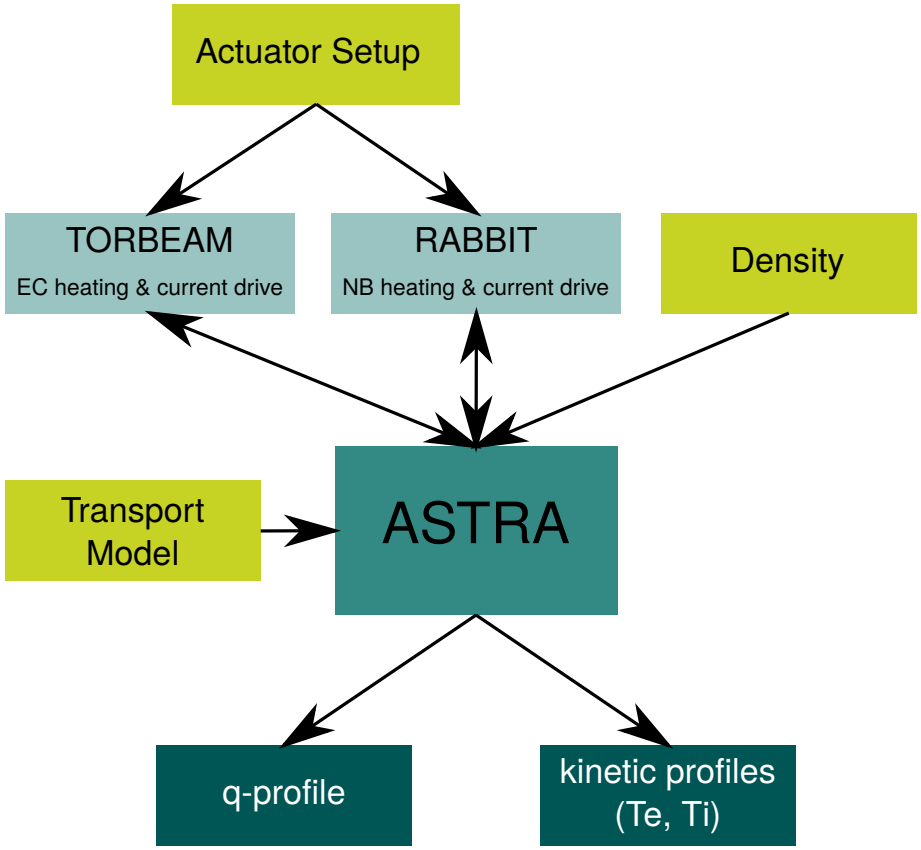

Figure 5.1: Schematic view of the model setup: Based on the applied transport model, ASTRA calculates the temperature and safety factor profiles from the inputs specifying the applied heating systems and underlying plasma density

The inputs are the actuator setup and the density. So far, the model only includes ECRH (see section 3.3.2) and NBI (see section 3.3.1) for heating and current drive, as these are the only systems capable of driving relevant amounts of current on AUG. The simulation of these systems is done by the RABBIT code for NBI and the TORBEAM code for ECRH, which provide the heating and current drive respectively. Both of these codes take their inputs from the previous time-step in ASTRA. Due to the modularity of the ASTRA setup, additional systems could easily be added in the future.

The plasma density is feed-back controlled (see section 4.5) in AT-discharges and does not change significantly between discharges subject to the same control scheme. For this reason, experimental data is used as input for the majority of this work. If the timing of the heating systems change, the time axis of the density evolution is

changed such that the same density is present at time, when the first NBI system is turned on. In appendix B, a density model based on the parameter used by the feed-back control ($n_{0,div}$) is discussed.

ASTRA then uses these inputs to calculate the temperature profiles, and solve the current diffusion equation based on them. As mentioned in the previous section, a transport model needs to be supplied, which is described in the next section.

5.3 The transport model

Due to the model's intended use in scenario development requiring iterative testing of different setups, as well as the potential interest to run the model between discharges, a short run-time is essential. In order to gain sufficient knowledge, modeling most of the ramp-up (starting from $t = 0.15$s corresponding to ~ 0.3 MA) in addition to multiple current diffusion times of the flat-top phase (usually up to $t = 4.5$s) is of interest.

First principle models (such as TGLF [111] or QuaLiKiz [112]) are available in ASTRA however, their run time of the the order of hours or more makes them incompatible with the purpose of this work. Instead, a comparatively simple, fully analytical Bohm/gyro-Bohm (see section 2.5) based model is used. This allows achieving a run time of only a few minutes on contemporary hardware (Intel Xeon Gold 6130, using 8 cores). The model is adapted from [113, 114, 24] and includes multiple free parameters, numbered c_n. The electron heat conductivity is given by:

$$\chi_e = c_1 \cdot T_e^{\frac{3}{2}} \cdot q^2 \cdot tem \tag{5.1}$$

including critical gradient theory (see section 2.4.3) via a simplified TEM threshold:

$$tem = \max\left(\sqrt{2\frac{r}{R}} \cdot \left(R\left|\frac{\nabla T_e}{T_e}\right| - c_2\right), 0\right) \tag{5.2}$$

The basic setup of the ion heat conductivity is similar to equation 5.1:

$$\chi_i = c_3 \cdot T_i^{\frac{3}{2}} \cdot q^2 \cdot itg \cdot f_{FI} \cdot f_{EM} \tag{5.3}$$

where the TEM threshold has been replaced with a simplified ITG threshold based on [115] and [116] (adapted to ITG):

$$itg = \max\left(R\left|\frac{\nabla T_i}{T_i}\right| - c_4 \cdot \left(1 + Z_{eff} \cdot \frac{T_i}{T_e}\right) \cdot \left(1 + c_5 \cdot \frac{S}{q}\right), 0\right) \tag{5.4}$$

including the magnetic shear S and effective ion charge Z_{eff}. It has been found empirically that the Bohm/gyro-Bohm setup with an ITG threshold does not sufficiently well describe the behavior. For this reason, additional terms for the fast-ion contribution (f_{FI}) and the electromagnetic contribution (f_{EM}) based on zero order results from gyrokinetic simulations [117] can improve the agreement. Those terms are given by:

$$f_{FI} = \exp\left(-c_6 \cdot \frac{P_{FI}}{n_i T_i} \cdot S_{norm}\right) \tag{5.5}$$

$$f_{EM} = \exp\left(-c_7 \cdot n_e \frac{T_e q^2}{B_{tor}^2} \cdot S_{norm}\right) \tag{5.6}$$

including the fast ion pressure P_{FI}, the normalized magnetic shear $S_{norm} = 1 - \frac{S}{\max(S)}$ and the toroidal magnetic field B_{tor}.

The behavior in the edge ($\rho_{tor} \sim 0.95 - 1.0$) is described by a scaling law, calculating the heat conductivity at the pedestal through:

$$\chi_{e,ped} = \left(\frac{P_{kin,ped}}{P_{crit,ped}}\right)^4 \tag{5.7}$$

including the kinetic pressure at the pedestal $P_{kin,ped} = k_B(n_{e,ped}T_{e,ped} + n_{i,ped}T_{i,ped})$ with the Boltzmann constant k_B and the critical pedestal pressure:

$$P_{crit,ped} = \frac{1}{2\mu_0} \cdot \beta_{pp} \cdot B_{pol,ped}^2 \tag{5.8}$$

where $B_{pol,ped}$ is the poloidal magnetic field at the pedestal, and the critically stable poloidal beta is given by the scaling [118]:

$$\beta_{pp} = 0.686 \cdot \kappa^{0.5}(1+\delta)^{1.68} q_{ped}^{1.61} \cdot \beta_{pol}^{0.33} \cdot \left(\frac{n_{e,ped}}{n_{gw}}\right)^{0.06} \cdot w_p^{1.29} \tag{5.9}$$

with the elongation κ, the triangularity δ, poloidal β (β_{pol}), the Greenwald density $n_{gw} = I_p/(\pi r^2)$, which is an empirical scaling for the operationally observed density limit [119] and a machine dependent scaling parameter for the pedestal width w_p, which is set to 0.11 for AUG.

The ion heat conductivity at the edge ($\rho_{tor} \sim 0.95 - 1.0$) is assumed to be equal to the electron heat conductivity.

The neoclassical contribution is calculated intrinsically in ASTRA, but its contribution is small for the cases studied during this work and only relevant for $\rho < 0.1$.

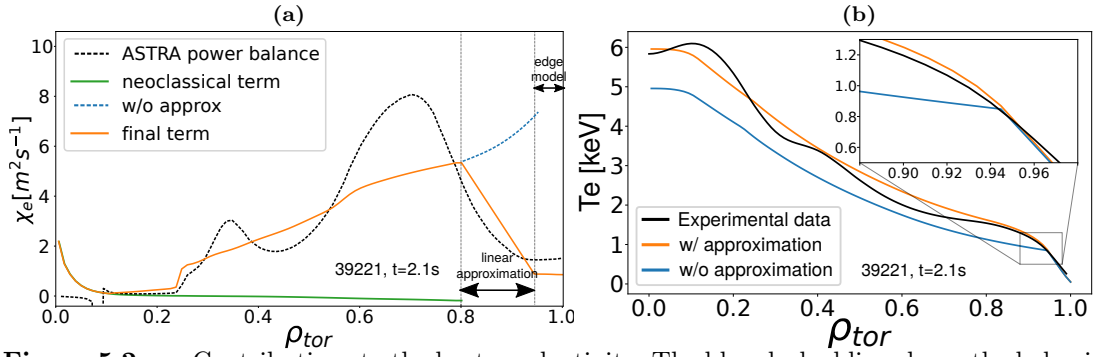

Figure 5.2: a: Contributions to the heat conductivity; The blue dashed line shows the behavior of the gyro-Bohm term towards the edge, a linear approximation towards the edge is used to improve agreement with experimental data. The black dashed line shows the heat conductivity calculated by ASTRA, when using experimental T_e-profiles and heating power as input
b: Effect of the linear approximation in the heat conductivity; The offset in the core between the case with and without the approximation could be mitigated by changing the free parameters; The insert shows a focus at the kink at the transition between edge and core model

A typical profile for the heat conductivity resulting of these contributions, is shown in figure 5.2a. It can be seen that the neoclassical contribution shown in green only has a comparably small impact and is only relevant below $\rho_{tor} \sim 0.1$. In the edge region (towards the right of the right dotted line) the heat conductivity is given by the edge scaling law. When comparing to the heat conductivity calculated in ASTRA from the experimental data based on the power balance (shown by the black dotted line) it can be seen that the gyro-Bohm term differs significantly in the region from $\rho_{tor} \sim 0.8$ to the edge. Instead of the expected drop, it shows an exponential increase, which would then generate a very sharp drop-off at the switch to the scaling law. Figure 5.2b compares the resulting T_e profiles. If the gyro-Bohm term is used up to the edge, a pronounced kink appears in the temperature profile at the location of the switch (shown in blue, the insert focuses on this location). This behavior disagrees with the experimental observation shown in black. In order to reproduce the experimental data, a linear connection between an empirically determined cutoff point and the edge is used. This solution then generates the behavior shown in figure 5.2a in orange, corresponding to the orange curve in figure 5.2b, which has a much better agreement with the experimental behavior. It was found empirically that the best agreement can be achieved when setting the cut-off to $\rho_{tor} \sim 0.8$, although it has to be noted that this value sometimes appears to moves to slightly lower values during a discharge. The dependencies of this parameter are unclear and might be explored in future work. The reason for this discrepancy is likely the increasing temperature gradient at $\rho_{tor} > 0.8$ causing the threshold term in equation 5.2 to increase as the

critical gradient approach is no longer valid in the region around the pedestal. The experimentally measured normalized temperature gradient as it appears in equation 5.2 is shown in figure 5.3. A strong increase starting at $\rho_{tor} \lesssim 0.8$ can clearly be seen, which according to the equation would lead to an increasing heat conductivity and can therefore not be generated, requiring a different description for this range.

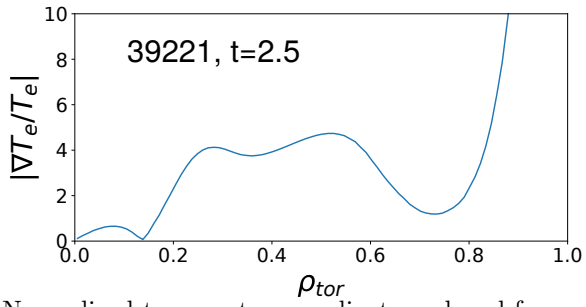

Figure 5.3: Normalized temperature gradient produced from measured data

As no profiles for Z_{eff} are available in the standard data evaluation on AUG, this value is assumed to be radially constant, and since no impurity transport is included, it is also assumed to be temporally constant. Typically, it is in the range of $1.3 \lesssim Z_{\text{eff}} \lesssim 2.0$. This parameter depends mostly on the machine conditions and has to be set manually for each discharge. In order to test the impact of this parameter, a comparison of the resulting behavior of q when setting Z_{eff} to the two outer edges of the typical range, was done. As can be seen in figure 5.4 the impact of this parameters on the time evolution of q is small and decreases over time.

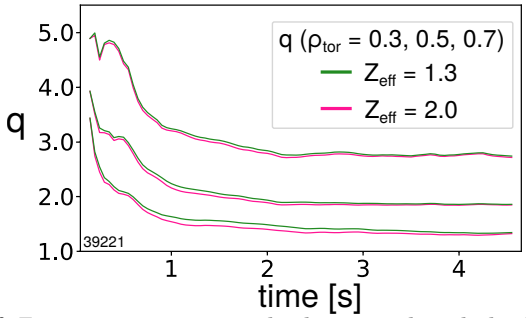

Figure 5.4: The effect of Z_{eff} on q comparing the lower end and the higher end of the typically expected range

To be able to include the ramp-up into the simulation, a description of the L-H transition is required. The transition is assumed to happen once a threshold (P_{L-H}) in the heating power crossing the separatrix (P_{sep}) is surpassed.

$$P_{sep} > P_{L-H} = c \cdot n_e(\rho_{tor} = 0.9) \cdot B_{tor} \cdot S_{lat} \tag{5.10}$$

This threshold is adapted from [120], where the exponents have been simplified and the prefactor has been turned into a free parameter (c) to better match the experimental behavior and account for uncertainties. The equation includes the electron density at the pedestal top location in H-mode, which is set to $\rho_{tor} = 0.9$, and the surface area of the plasma (S_{lat}). Figure 5.5 shows the comparison of these parameters for an exemplary discharge. The free parameter has been adjusted such that for the discharges considered during this work, the L-H transition reliably does not occur in the phase where only one NBI source is active (green shaded area), but in the phase after the second beam is turned on. The used value of $c = 0.0075$ is at the lower end of the viable options. As the heating power crossing the separatrix increases significantly during the L-H transition for discharges considered during this work, this parameter could be increased, moving the blue curve up and still produce a similar behavior.

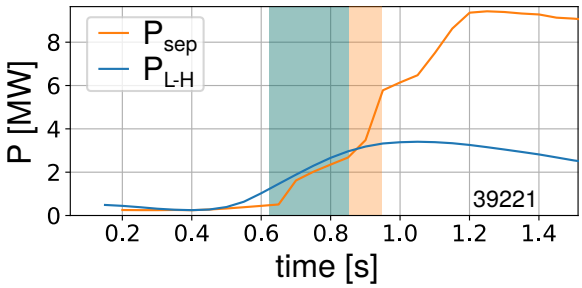

Figure 5.5: L-H transition threshold compared to power at the separatrix; The green shaded area highlights the phase, where one NBI is on, the orange shaded area highlights the strong increase after the second NBI system is turned on

In the gyro-Bohm model, some of the free parameters have distinct values when in L-mode. Due to the invalidity of the edge scaling in L-mode, the heat conductivity at the edge is instead set to an arbitrary large freely selected value, and the linear approximation is not used. An example for a heat conductivity profile in L-mode is shown in figure 5.6. The neoclassical contribution causes the nonzero behavior inwards of $\rho_{tor} \sim 0.15$.

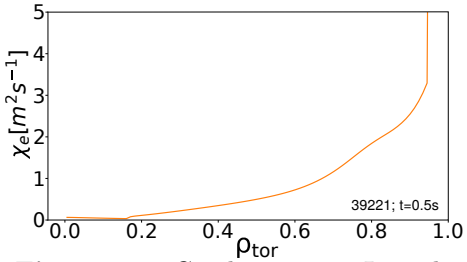

Figure 5.6: Conductivity in L-mode

It turned out that the initial conditions only have a small impact on the simulation. This is likely due to the low energy confinement time in the early phase and is consistent with findings from [121]. Figure 5.7a shows the impact of the initial T_e, comparing cases of ten times and ten percent of the initial value. Note that the very large difference is required to see any difference past $t \sim 0.2$s. It can be seen, that the impact of lower values disappears after a very short time, while higher values stay visible longer. The effect in the center at ρ_{tor}=0.1 for the much higher value stays visible for ~ 0.5s, although as the volume in this area is low, this is expected to have low impact. The impact of the safety factor is shown in figure 5.7b, where it can be seen, that a much smaller difference is sufficient to see an effect. Still, for a change of the initial profile of $\pm 20\%$ the effect mostly disappears as the safety factor starts to enter its stationary phase at $t \sim 1$s.

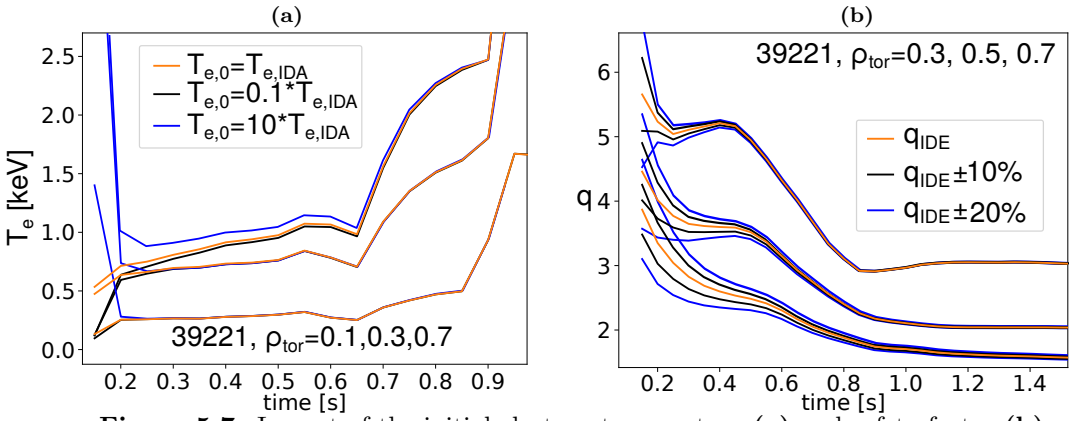

Figure 5.7: Impact of the initial electron temperature **(a)** and safety factor **(b)**

5.3.1 Parameter fit

To determine appropriate values, a scan over the free parameters was performed. Beginning from an arbitrary initial estimate, the quality of the fit was determined using a reduced χ^2 metrics:

$$\chi^2 = \frac{\sqrt{\sum_i^{N_i} \frac{(f_{exp,i} - f_{m,i})^2}{\sigma_{exp,i}^2 + \sigma_{m,i}^2}}}{N_i} \tag{5.11}$$

For the point of interest i, with a total amount of points N_i, f_{exp} is the experimental value, f_m is the simulated value and σ^2 is their respective variance. In this metrics, a value close to one is considered as a good fit, while a value much larger than one indicates a poor description of the data set. The variance for the experimental data is determined based on the known error ranges. For the modeled data, as ASTRA

simulations are deterministic, no error estimate is available and the corresponding variance is therefore set to zero.

A set of reference discharges was chosen. These are all 800kA, late heating discharges, keeping as many parameters as possible close to the intended use case, in order to be able to ignore possible dependencies of the free parameters. This setup does however limit the generalizability of the model. Based on these discharges, the optimal value for each parameter was determined. To that end, the χ^2 metric was minimized for the radial locations of $\rho_{tor} = 1/3$ and $\rho_{tor} = 2/3$. These locations were chosen since the area closer to the edge is largely determined by the scaling law, and the area closer to the core is of reduced importance due to the low volume and higher errors on the measurements.

The objective of the model is to predict the time evolution of the plasma. This approach is therefore designed to match the experimental data over time. This setup effectively reduces the influence of fluctuations, noise, and the utilization of actual density data as input on the results. Due to experimental noise and the measurement uncertainties, there is a range, in which the fit parameters can be changed without a large change to the quality of the fit (change in χ^2 is less than 10%).

The best value of χ^2 achieved for the electron temperature, averaged over the set of reference discharges, was found to be $\chi^2 \sim 1.2$, which indicates a good quality fit. As T_e has a large impact on the conductivity and therefore on q, this is important for the main goal of the model. The fit quality for T_i is considerably worse, only achieving a value of $\chi^2 \sim 3.6$. This quality is however still acceptable as T_i has only a small impact on the other parameters. In order to address this inaccuracy, a study of the impacts of T_i is done in section 6.2.

	c1L	c1H	c2L	c2H	c3L	c3H	c4	c5	c6	c7
mean	0.1	0.54	3.4	4.5	0.04	1.4	0.6	-	2.8	0.32
range	±0.05	±0.2	±0.5	±1	±0.03	±0.5	±0.3	-	±1	±0.1
used	0.1	0.5	3	4	0.04	1.4	0.5	0.5	3	0.3

Table 5.1: Mean of the best fitting parameter for each discharge of the reference set, the range in which the parameters can be altered without significantly changing the quality of the fit and the values actually used in the model

It was found that the parameters $c4$ and $c5$ have almost the same effect. Therefore the fit was done for $c4$, while $c5$ was set to a fixed value. For each of the reference discharges, the best fit is achieved for slightly different values of the free parameters although these values are close to each other for the entire set and there is an overlap of the region where the quality of the fit is similar. This provides confidence, that the

model can be used predictively. Table 5.1 shows the mean of best fit values. Further, the range in which the parameters can be altered without changing the quality of the fit by less than 10% and the values actually used, are shown. In some cases, where it was found that the value finally used improves the agreement for a majority of the reference cases, these differ from the mean, although they lie within the range of low impact on the quality of the fit. A plot of the fit for each of the reference discharges can be found in appendix A.4.

5.4 Model limitations

The linear connection between Bohm/gyro-Bohm transport and edge/pedestal transport enhances agreement with experimental behavior. However, this correlation lacks a firm physics foundation. Moreover, the cut-off value that would achieve the best agreement can vary over time, indicating that some physics is missing.

The transport model solely incorporates TEM and ITG turbulence. Consequently, if other phenomena play a significant role in plasma behavior, the resulting scenario cannot be replicated accurately.

The model does not account for magnetohydrodynamic (MHD) effects, which means that the simulated behavior might not be adequately stable towards Neoclassical Tearing Modes (NTM) for experimental feasibility. As has been shown in [122], avoiding low-magnetic shear regions around rational flux surfaces can improve this situation. Additionally, effects caused by MHD activity such as a drop in core temperature caused by the presence of a large NTM, cannot be captured.

The current version of the model lacks the incorporation of experimentally found density limitations around the L-H transition (mentioned in section 4.5). As a consequence, a specific density configuration that yields valid results in the simulation, might not be feasible in real experiments. Therefore, experimental tuning of the density may become necessary to achieve a successful discharge.

The model does also not account for experimental fluctuations, particularly those induced by Edge Localized Modes (ELMs, see section 2.6), leading to a less accurate agreement of profiles between simulation and experiment at certain points in time. When experimental density data is utilized as input, these fluctuations are transmitted, impacting other quantities in the simulation.

The parametrization of the model is based solely on AUG discharges, all of which share the same plasma current, magnetic field, and plasma geometry. Therefore, it cannot be ruled out that the model's free parameters might depend on these quantities. A more comprehensive physics-based model that considers a broader range of discharges is available [123], and might be used in future work.

Chapter 6

Model application

To test the applicability of the model for scenario design, a new scenario for AUG has been developed. Based on a late-heating reference discharge, the target for this scenario was to achieve a q-profile as high as possible using the early heating approach. Note that similar to the previous chapter a large part of the results presented here are also published in [108].

6.1 Designing a new early-heating AT scenario

A late heating scenario (AUG discharge 37722) with a plasma current (I_p) of 800 kA, corresponding to $q_{95} \sim 5$ was used as a reference. This discharge is also part of the set used to determine the model parameters. The magnetic configuration used in these discharges forms the X-point (see section 2.1.2) at $t \sim 0.6$s. The external heating systems can be applied slightly after that, since increasing heating power during the limiter phase before the X-point formation would lead to unacceptable tungsten influx from the wall.

The setup of the density control is shown in figure 6.1. In the earliest phase (blue shaded) during the L-mode, the density is feed-backed controlled based on the core density. Around the L-H transition (orange shaded) this is switched to the edge density with the parameters set up such, that the fueling valves are essentially maximally open, which can be seen by the strong increase in the fueling rate (shown in red). Afterwards, the control switches to the divertor neutral density ($n_{0,div}$), the target of which (dashed line) can be seen in figure 6.1 as compared to the measured data (solid line). The values before the control is active are set to a rough approximation of the expected behavior in order to not introduce unwanted behavior through the integral term of the controller. The increase after ~ 6s is caused by outgasing from the wall,

as it can be seen that the fueling at this point is at essentially zero. Figure 6.2 then shows the resulting density evolution of the newly designed scenario, compared to the reference case at a representative location and the time when heating starts.

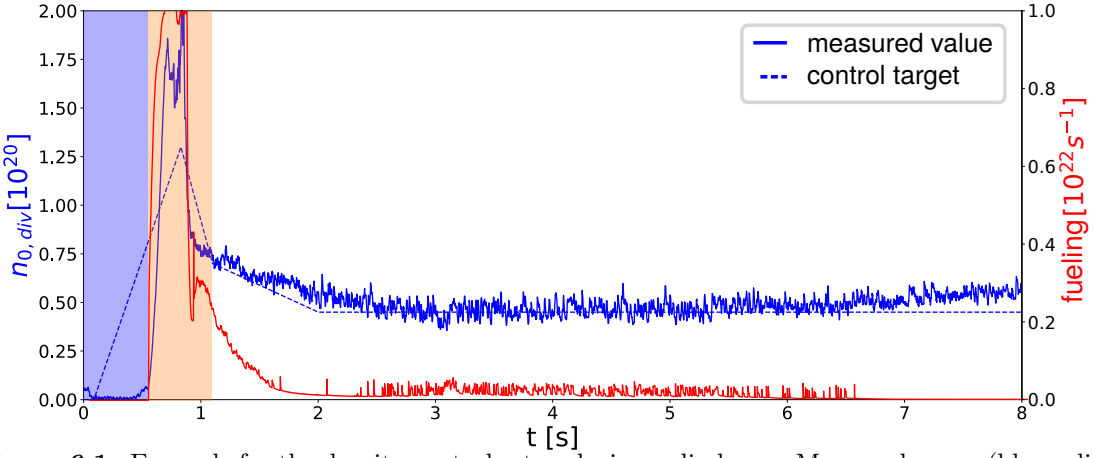

Figure 6.1: Example for the density control setup during a discharge; Measured $n_{0,div}$ (blue solid) and control target (blue dashed); Also shown is the resulting fueling rate

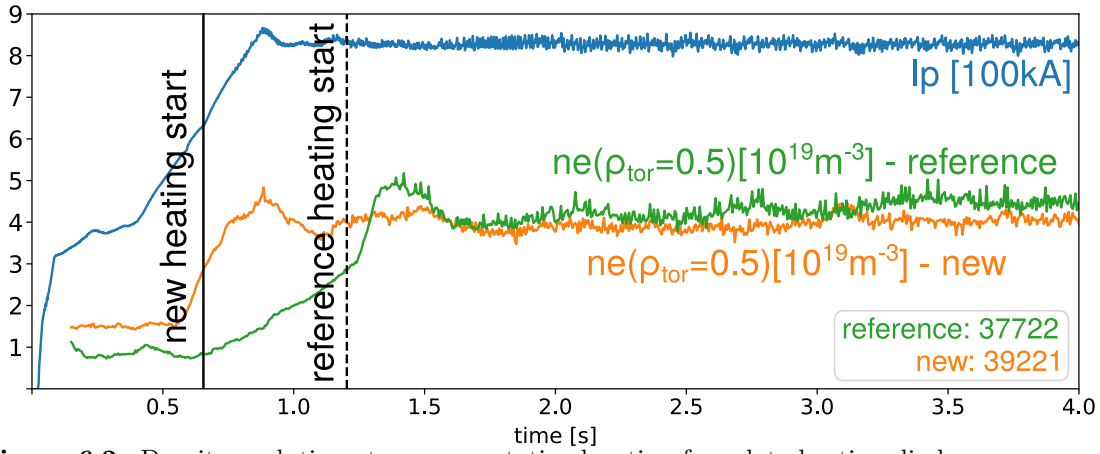

Figure 6.2: Density evolution at a representative location for a late heating discharge compared to an early heating discharge in comparison to I_p. The density at the time, when the heating starts is at a very similar value for both discharges.

The requirements for the new scenario were to avoid local minima in the time evolution and profiles of the safety-factor. Further, the jumps in the first derivative of the safety factor were minimized. The goal was then to achieve a q_{min} as high as possible, that can still be maintained throughout the discharge with heating power comparable to the reference scenario. It is possible to change the timing of the

heating systems, the specific NBI source and the deposition locations for the ECRH system.

The initial current drive setup was chosen arbitrarily, based on the reference discharge. The simulation was then run based on these inputs and the resulting behavior was evaluated. In order to comply with the previously stated criterion, iterative changes to the heating setup were implemented until a setup satisfying the requirements was found.

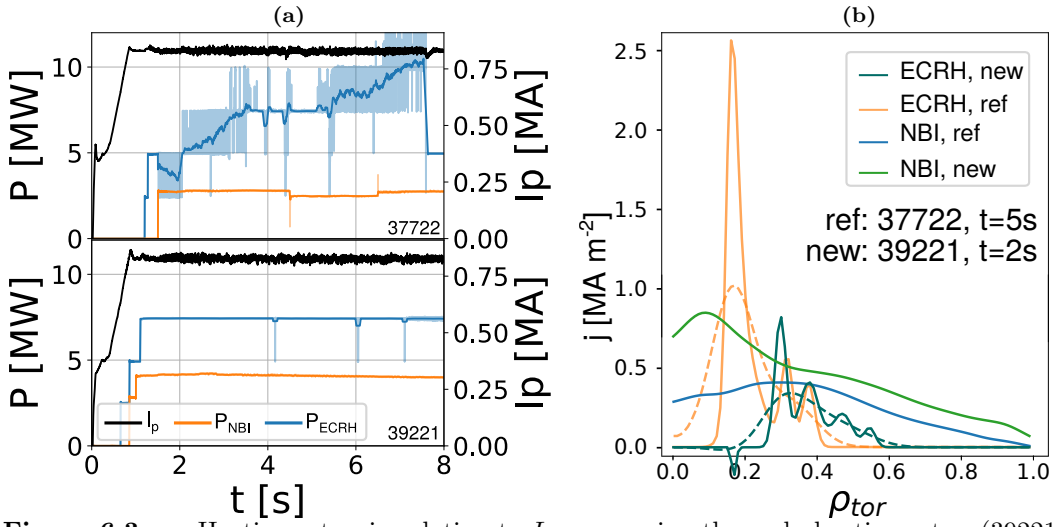

Figure 6.3: **a:** Heating setup in relation to I_p, comparing the early heating setup (39221) in the lower plot, with the late heating setup (37722) in the upper plot; **b:** distribution of driven current in both scenarios after all heating systems are turned on, the dashed line shows a smoothed version of the ECRH driven current

Figure 6.3 shows the resulting setup for the heating systems. The first NBI starts at t =0.65s, which was found to be the time, where the X-point is reliably established. The NBI power is then increased to three beams, adding an additional beam every 200 ms, which is the empirical limit, found not to cause NTM stability issues. ECRH is added in two steps in order to keep the time evolution of q continuous and prevent it from dropping. One of the gyrotrons is used for central heating (see section 4.5) and is added in the first step. Figure 6.3b shows the corresponding profile of the driven current, comparing the new scenario to the reference scenario. It can be seen, that the NBI system drives more current, although considerably less localized. ECRH driven current is considerably more localized, allowing for a more precise shaping of the q-profile, even though the absolute amount is lower. The ECRH systems in AUG all have the same power, the significant decrease in current drive efficiency towards higher values, mentioned in section 3.3.2, can clearly be seen. In the new setup, the

gyrotron used for core heating is setup to have no current drive, but does generate the small negative contribution. The outermost gyrotron is used for suppression of the 2/1 NTM and only has a low impact on q. The dashed lines show a smoothed version of the ECCD, which preserves the surface integral. This setup is done in IDE to account for broadening of the ECRH beam through turbulence in the edge. The sharp ECCD-peaks would lead to some visible features at the location of the peaks however, the impact on the overall q-profile is very low and it could likely not be seen with the available resolution of the measurement. A comparison of representative q-profiles for a case with and without smoothing is shown in figure 6.4. It can be seen that the difference between the two profiles is very low.

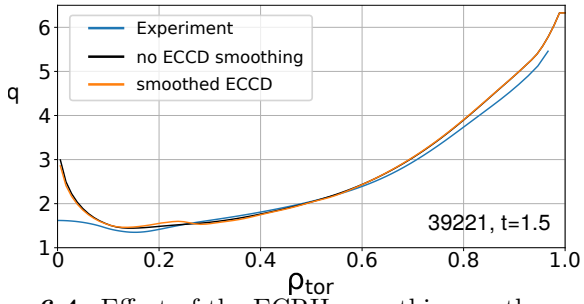

Figure 6.4: Effect of the ECRH-smoothing on the q-profile

Comparing to the reference case, the NBI contribution has been changed to drive more current, although more peaked in the center. To counteract this, keeping the shape of the q-profile away from a peaked setup, the ECRH deposition locations have been moved further outwards.

6.2 Experimental results

The new setup was run successfully on AUG. Some tuning of the fueling around the L-H transition was done to provide sufficient density (mentioned in section 5.4, density control from previous section), after which a stable discharge (39221) was achieved. A comparison of the design goal for the scenario to the experimental behavior is shown in figure 6.5. It can be seen, that the experimental behavior (shown in black) follows well the prediction by the model (shown in orange) while being at a considerably larger value than the reference case (shown in blue).

A comparison of the electron temperature between the modeled behavior and the simulation is shown in figure 6.6. Excluding experimental noise and fluctuations (see section 5.4), which are clearly visible in the time evolution, the simulated behavior matches the experimental data very well and agrees within the error range. The

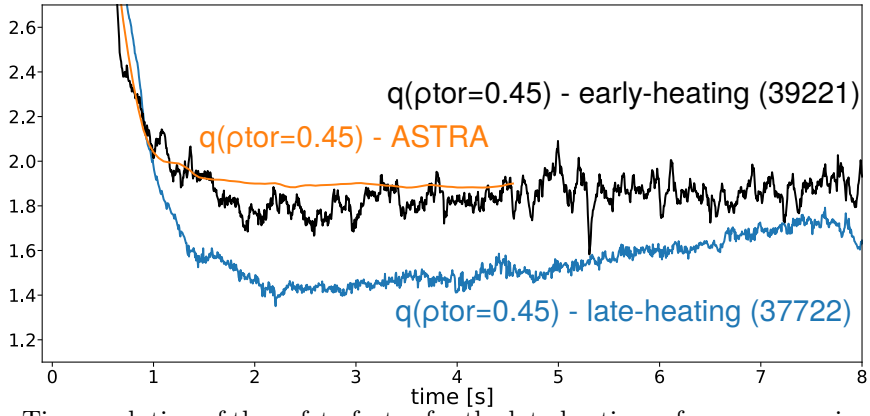

Figure 6.5: Time evolution of the safety factor for the late-heating reference scenario, the scenario prediction in ASTRA, and the experimental result of that scenario. The experiment reproduces the behavior, predicted by the model

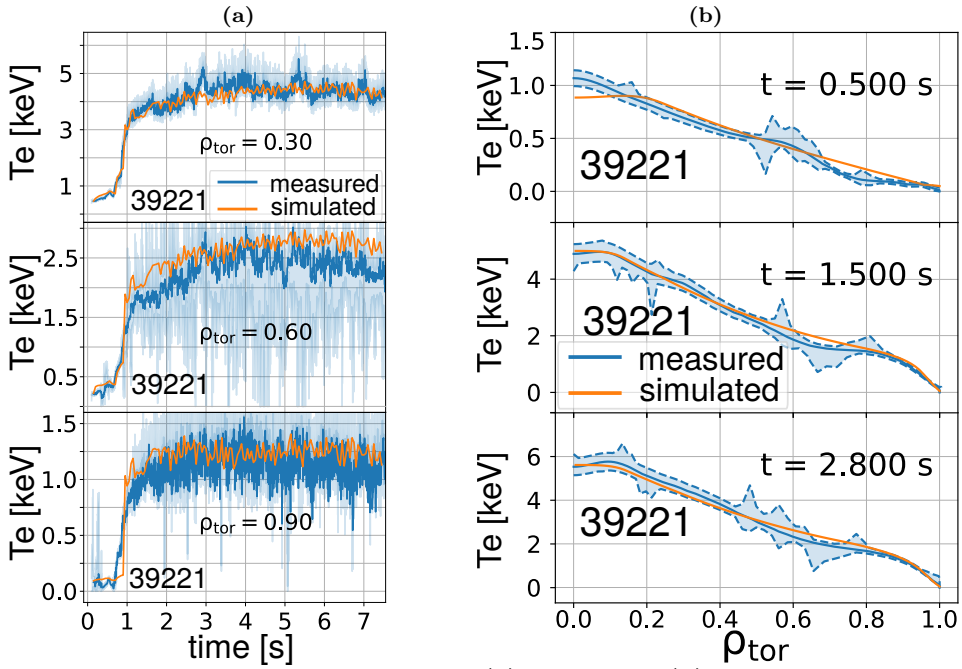

Figure 6.6: Electron temperature time evolution **(a)** and profiles **(b)**, comparing the experimental results of discharge 39221 with the modeled behavior. An agreement within the error bars can be seen.

fluctuations in the modeled T_e behavior stem from the experimental density input. Both of these effects lead to the situation, where the agreement can be worse for some specific time-steps, which is the reason, profiles were not considered when

determining the free parameters of the model (see section 5.3.1). The q-profiles shown in figure 6.7 also show a good agreement with the experimental data both in L-mode (top left at $t = 0.5$s) and in H-mode (the other three). Some discrepancies are expected, since fluctuations are also present on the safety factor (see figure 6.5). It should be mentioned, that the agreement in the core ($\rho_{tor} < 0.2$) is somewhat worse, possibly due to effects from reversed shear not being included in the model. Due to the small volume in the affected region, this discrepancy does not rise concerns.

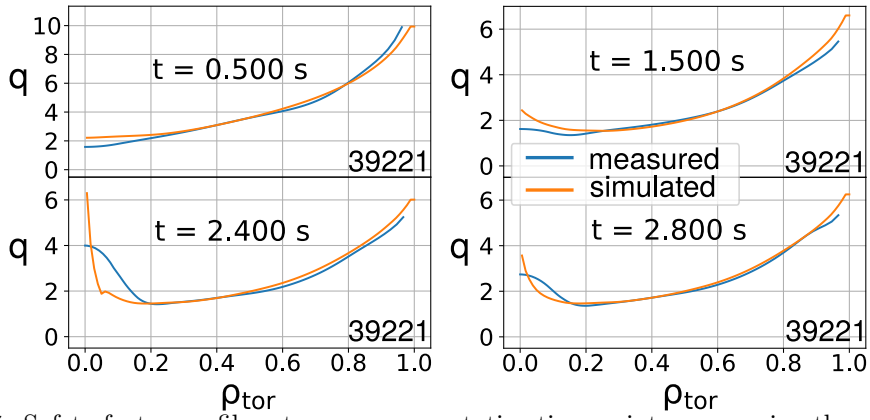

Figure 6.7: Safety factor profiles at some representative time-points, comparing the experimental results of discharge 39221 with the modeled behavior. A good agreement can be seen. The discrepancy at 2.4s is caused by different temperature profiles due to fluctuations.

As could have been expected from the inferior quality of the free-parameter fit for the ion temperature (see section 5.3.1), the modeled behavior of T_i shown in figure 6.8 shows an increased discrepancy to the experiment. Trends and profile shape are reproduced. However, while the fit in L-mode is good, the time evolution after the L-H transition is different, especially in the core, indicating some missing physics in the model. After $t \sim 3$s, the simulated behavior shows a better agreement, when the measured value reaches its flat-top.

The main effect on the ion temperature on the q-profile is through the ion-electron heat exchange term ($P_{i\to e}$), which is however small, when compared to the other heating sources ($P_{i\to e}/P_{e,tot} \sim 2.5\%$). As T_e shows a good agreement despite the difference in T_i, this discrepancy is not a concern.

A parameter study was done to test how much T_i impacts the q-profile. Since it was found that the model reproduces T_e, it was fixed during for this study to eliminate effects from the interaction term. T_i was set to the experimental value and multiplied in the following by a set of factors. The resulting time evolution of q at three different radial locations, comparing a cases when T_i equals the experimental value and when it is multiplied by the factor 1.5, is shown in figure 6.9a.

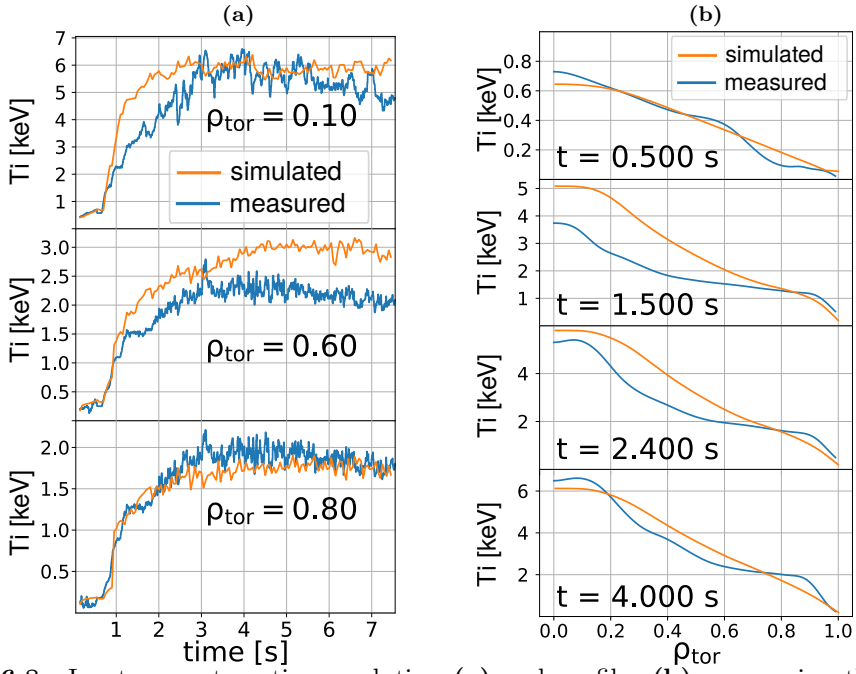

Figure 6.8: Ion temperature time evolution **(a)** and profiles **(b)**, comparing the experimental results of discharge 39221 with the modeled behavior. While the general trend is reproduced the general agreement is considerably worse than for the electron temperature

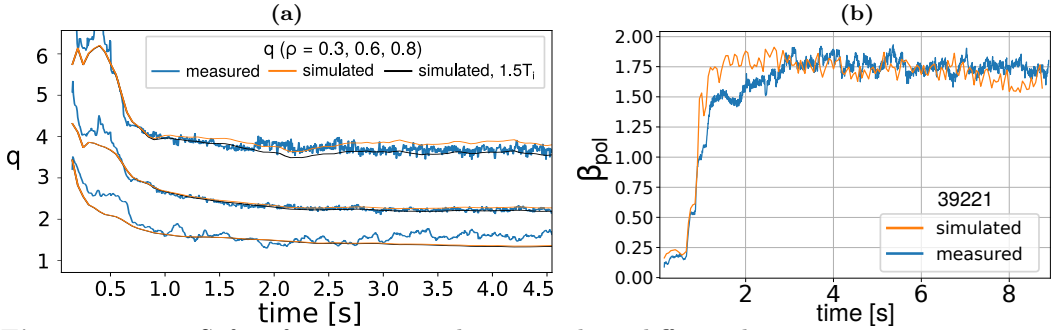

Figure 6.9: **a:** Safety factor time evolution at three different locations, comparing experimental data to a simulation with T_i fixed to the measured value and fixed to 1.5 times the measured value: **b:** Simulated β_{pol} compared to the IDE calculation, a very similar behavior as the core T_i can be seen

As expected, the effect is low. The reason is, that T_i only contributes to the safety factor through a small contribution in the bootstrap current and a small impact on the beam driven current due to a slightly altered fast ion response. As the the discrepancy in T_i is lower than a factor of 1.5 for most cases and the model is mainly

intended to predict the behavior of q, the inaccuracy of T_i was deemed acceptable.

The behavior of β, shown in figure 6.9b follows the behavior of the time evolution of T_i, showing a similar discrepancy in the phase after the L-H transition, indicating again, that some phenomenon slowing the increase in ion temperature is being missed by the model. After $t \sim 3$s the simulated behavior agrees well with the experiment.

6.3 Performance of the scenario

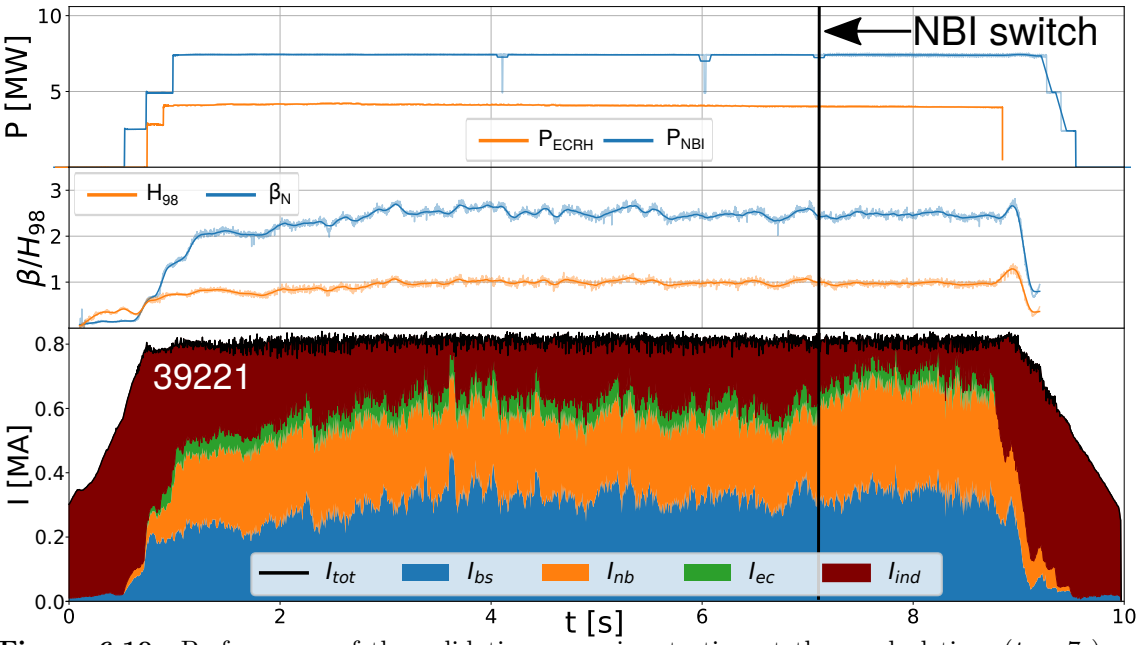

Figure 6.10: Performance of the validation scenario; starting at the marked time ($t \sim 7$s) an increase in I_{nb} can be seen without a corresponding change in P_{NBI} due to a change from an on-axis to an off-axis source

Figure 6.10 shows the current distribution for the successful scenario introduced in the previous section on the bottom, together with the corresponding time evolution of the confinement factor H_{98} and β_N in the middle, and the applied heating power on the top. It can be seen that the majority of the current is generated by bootstrap current, neutral beam driven current and inductive current, while ECCD only makes up a small fraction. The average bootstrap fraction in the stationary phase is at $\sim 41\%$ with a standard deviation of $\sim 4\%$. After ~ 7s, also marked by a black horizontal line in the figure, a switch from an on-axis NBI source to an off-axis source occurs. This is accompanied by an increase in NBCD from $\sim 30\%$ to $\sim 40\%$,

increasing the non-inductive fraction of I_p to $\sim 90\%$. A comparison of performance parameters can be found in appendix A.3.

6.3.1 Stability limits

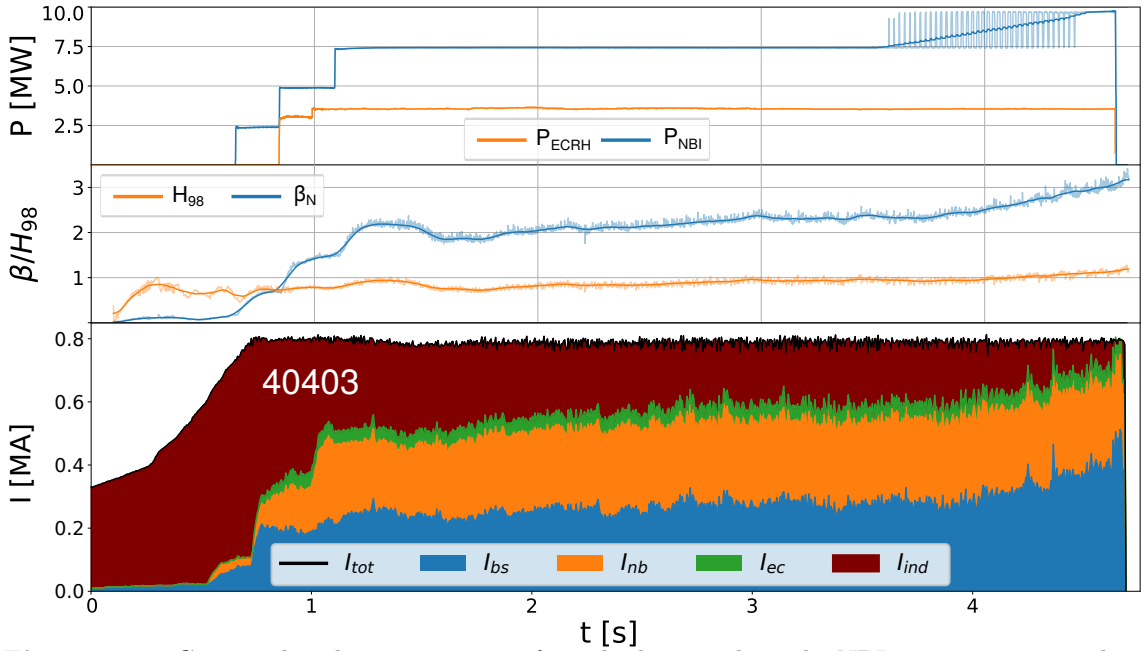

Figure 6.11: Current distribution over time for a discharge, where the NBI power was ramped up until disruption; The scenario becomes fully non-inductive at the end

As mentioned in section 2.3.1, the bootstrap current depends on the pressure gradient, which can be increased through β by increasing the heating power in the plasma. For this reason, it would be desirable to operate as close as possible to the β stability limit to maximize performance. In order to find this limit, an additional β ramp is introduced in the scenario, after β has been at its flat-top value for some time. The performance of this scenario is shown in figure 6.11, with the same style as for the previous discharge. The effect of the β ramp, leading to a considerable increase in bootstrap current can clearly be seen. At the same time, the confinement also goes up, while the NBCD does not change visibly due to the additional power coming from a low current drive on-axis source. After the discharge reaches a maximum at $\beta_N \sim 3.2$ at $t \sim 4.5$s, a disruption due to an ideal mode (indicating the ideal β limit) occurs, terminating the discharge. Just before, the discharge becomes transiently fully non-inductive. The disrupting mode is identified as ideal

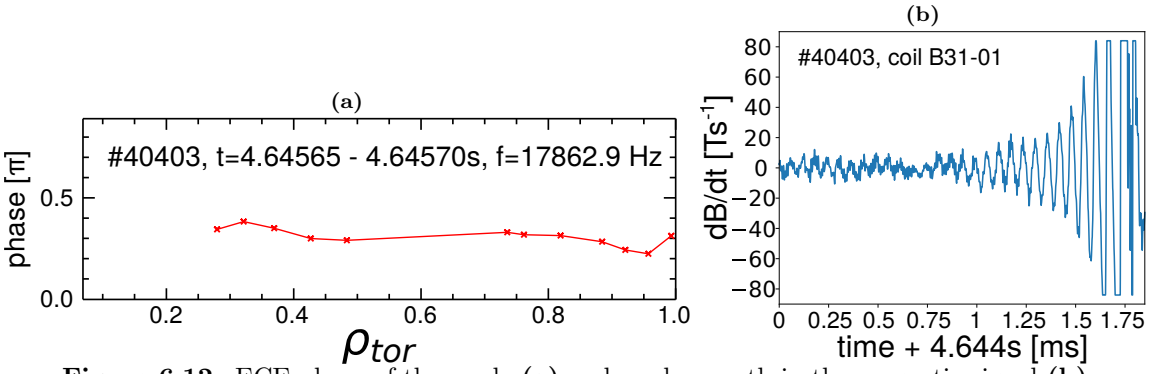

Figure 6.12: ECE phase of the mode **(a)** and mode growth in the magnetic signal **(b)**

since it satisfies both of the typical features. It features a constant phase in the ECE measurements (see figure 6.12a) and a very high growth rate $\gamma_{\text{MHD}} \sim 4.2 \cdot 10^6 s^{-1}$, calculated based on the magnetic signal shown in figure 6.12b through the procedure introduced in [124]. The corresponding growth time $\tau_{\text{MHD}} \sim 1.2 \cdot 10^{-7} s$ is comparable to the Alfvén time.

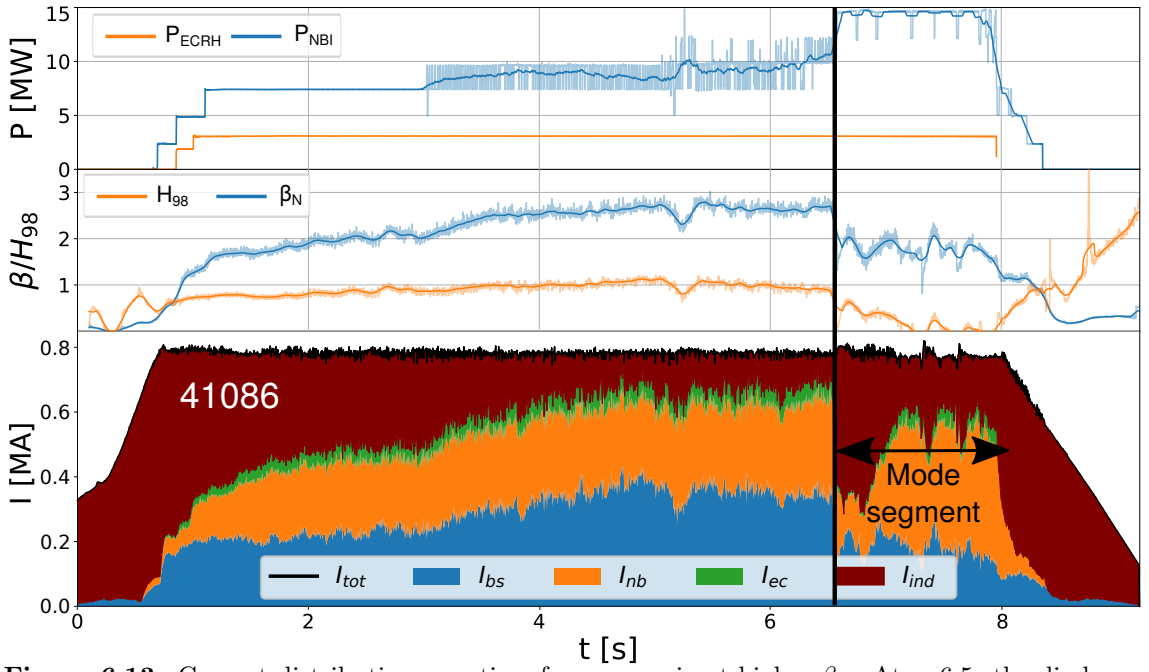

Figure 6.13: Current distribution over time for a scenario at higher β_N; At $\sim$ 6.5s the discharge switches to a piggyback segment with no relevance to this work after a locked mode appears

A further discharge was realized with the power feed-back controlled to reach $\beta_N \sim 2.7$, a value considerably below the previously found limit, but still higher than the initial setup. The results of this discharge are shown in figure 6.13. The power ramps up at $t \sim 3.5$s after which it stays constant for some time. At $t \sim 5.2$s, a clear drop can then be seen in the bootstrap current, confinement and β values. This is due to a NBI source being switched off because of overheating of the inner wall target tile. The controller does switch on additional power to correct for this however, a considerable drop in core-T_i (see figure 6.14a) can be seen and does not fully recover.

This causes a change in transport behavior, which can be seen from 6.14b, showing logarithmic profiles for both the electron and ion temperatures. T_e only shows an offset between the time before and after the event, while the T_i shape changes: The edge temperature is largely unaffected, while the core temperature shows a reduction. A larger change can therefore also be seen in the core region of the T_e/T_i profile.

After $t \sim 6$s, an attempt is made to further increase β_N, but a quickly locking NTM appears, effectively ending the discharge. Notably, this instability occurs at a level where the previous discharge was still stable, suggesting that the change in transport, resulting in altered profiles, has lowered the stability threshold. The discharge "survives", but looses most of the confinement, rendering the the remaining part irrelevant to this work.

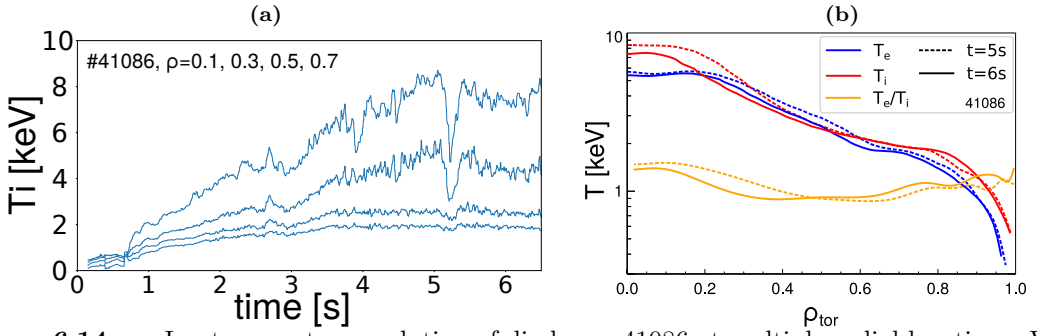

Figure 6.14: a: Ion temperature evolution of discharge 41086 at multiple radial locations. While the outer values are mostly unaffected, a significant drop in temperature at $t \sim 5.2$s can be seen for the inner values. **b:** Logarithmic temperature profiles and T_e/T_i before (dashed lines) and after (solid lines) the T_i drop at ~ 5.2s

Having a look at the performance of this scenario, the impact of the increased β on the bootstrap current can clearly be seen. In the phase before the NBI switch, a bootstrap current fraction of $\sim 48\%$ is achieved, while the average over the entire phase after β reaches a flat-top (from $t \sim 4$s to $t \sim 6.5$s) is at $\sim 46\%$, when excluding

the drop. This reaches a non-inductive fraction of $87\% - 90\%$. As mentioned in section 3.3.1, the second off-axis source was not available for this discharge. If a similar behavior as in the "baseline" case (figure 6.10) showing an increase in I_{nb} of $\sim 10\%$ is assumed, this scenario may be capable of becoming fully non-inductive. If the full configuration will be available in the next campaign, testing this possibility may be of interest.

Even at a non-inductive fraction of $\sim 90\%$ such a setup could be run for a very long time. As can be seen in figure 6.15 showing the current through the transformer coil, such a discharge stays at considerably lower flux-consumption compared to a standard H-mode discharge. The pulse duration in AUG is limited by the available power due to inefficiency of the copper coils. If the flux through the central transformer were the only limiting factor, such an advanced scenario discharge could run for a very long time: Assuming a consistent current increase as can be seen in the stable phase from $t \sim 2$s to $t \sim 6.5$s, as is indicated in the black dotted line in the figure, this scenario would run for ~ 70s until it reaches the same current as seen in the standard H-mode case.

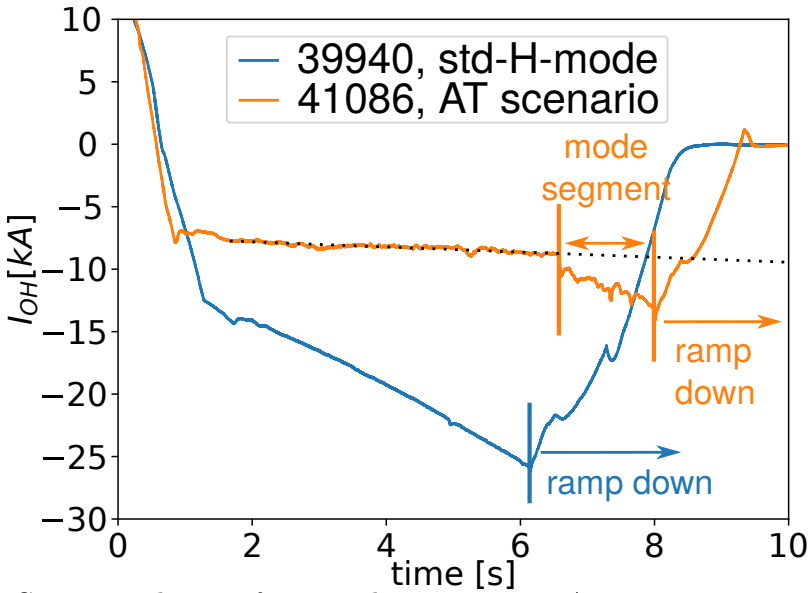

Figure 6.15: Current in the transformer coil, comparing an AT-scenario to a standard H-mode discharge; The black dashed line shows an extrapolation of the current increase during the stable AT-phase

Chapter 7

Application to a 1 MA scenario

In order to test the general validity of the setup and to account for the fact that, so far, only discharges at one specific plasma current were considered, the model was applied to a different scenario on AUG. This chapter presents this scenario, how the model was applied to it to solve some of the remaining problems and compares the model to a different system. This system was being worked on in parallel to this work, and the data from it presented in the following section was produced by an external collaborator [122, 125, 126].

7.1 The counter ECCD setup

The plans for the DEMO foresee AT operation at $q_{95} \sim 4.5$ [91]. In order to achieve comparable dimensionless parameters on AUG, a scenario with a plasma current of 1 MA resulting in $q_{95} \sim 4.1$ has been developed. Due to the reduced efficiency of ECCD off-axis (see section 3.3.2), q-profiles relevant to AT scenarios cannot be achieved with the standard setup, in which the current points in the same direction as the plasma current (co-current). However, directing the ECCD against the plasma current (counter-current) [127] allows to utilize the much higher efficiency on-axis for the shaping of the q-profile. An example for a current density profile and the corresponding q-profile calculated by IDE, as it can be achieved by this setup is shown in figure 7.1.

Here, the green shaded area denotes the negative ECCD, which is much larger, than in previous cases (see e.g. figure 4.1b). The final profile is similar to a profile as might be generated by a co-current setup, however the inductive current fraction is considerably larger. For this reason, while the counter-current setup allows studying the effect of such a combination of q-profile and q_{95} on currently available devices, it

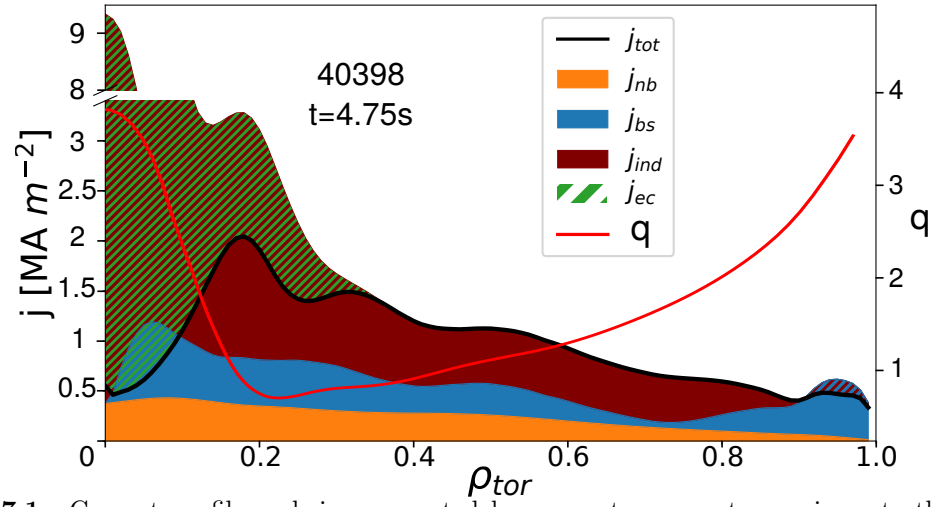

Figure 7.1: Current profile as being generated by a counter current on-axis; note the broken ordinate axis; the negative inductive current close to the edge is likely caused by uncertainties in the measurements and not real; Also shown is the corresponding q-profile as calculated by IDE

is not interesting for future devices intended to generate power.

The high counter-current ECCD on axis causes an additional problem: Both, ASTRA and the equilibrium code IDE used to generate the experimental q-profiles can experience transient negative values of the current at the magnetic axis ($\rho_{tor} \sim 0$). This would cause the plasma safety factor to diverge, which the systems are not designed to handle and usually causes a crash. The IDE code solves this issue by applying a significant smoothing to the Electron Cyclotron Current Drive, which does potentially cause discrepancies (see next section). In ASTRA this problem is solved by arbitrarily increasing the flux on axis. Doing so does however affect the behavior of q in the region of $\rho_{tor} \lesssim 0.2$, which is therefore not shown in the counter-ECCD cases.

It was found that the free parameters identified in section 5.3.1 describe the behavior of this scenario reasonably well, but underestimate the electron temperature in the core. In order to remedy this issue, a re-fit of the free parameters has been

	c1L	c1H	c2L	**c2H**	c3L	c3H	c4	c5	c6	c7
mean	0.1	0.4	2.75	5.25	0.035	1.6	0.5	-	2.75	0.2
range	±0.05	±0.2	±0.5	±1	±0.02	±0.5	±0.3	-	±1	±0.1
used	0.1	0.5	3	4 → **5**	0.04	1.4	0.5	0.5	3	0.3

Table 7.1: Results of the fit for the counter ECCD-scenario; the parameter that needed to be changed is marked in red, with the previous value shown in black

done. It should be noted that as the counter-current ECCD scenario is uncommon, a large set of reference discharges was not available. The results are shown in table 7.1, where it can be seen that only a change to the c2H parameter, corresponding to the TEM threshold was required. Previous studies [128] have found the TEM threshold to be dependent on the local magnetic shear, which is not included in the model. It is different between the two scenarios, which would make it a likely candidate for this required change. While a global observation of an increased q_{min} and reduced q_{95} would indicate a reduction of the shear, which would be a change in the wrong direction, the local shear between the two cases is sufficiently different to make a clear statement impossible without extending the model to include this effect. As the other effects known to influence the TEM behavior are similar between these cases, the local magnetic shear is still the most likely candidate for this required change of c2H.

7.2 Comparison to a RAPTOR model

The RApid Plasma Transport simulatOR (RAPTOR) code [129, 130, 131] is a 1D transport code, capable of simulating plasma density, temperature and poloidal flux (and thereby q). A similar, albeit somewhat simpler model [122] is available in this framework, for which comparisons to the ASTRA model was done. The RAPTOR model does not calculate T_i, which is expected to have a low impact (see section 6.2), but, in addition, it neither includes the pedestal nor its own equilibrium, and it uses a simplified setup for the heating power. These points reduce the trustworthiness of the model for predictive use, however it still allows a comparison to the ASTRA model, especially for post-discharge simulations, and thus enables to further validate the results of the two models. In addition to that, the RAPTOR model features a non-linear optimizer for relevant plasma parameters such as q, which would allow for more informed changes to the heating systems than the empiric workflow done in section 6.1. In order to verify that both setups are compatible, simulations were done in both models for the reference discharge of the counter ECCD-scenario (39342). The results are displayed in Figure 7.2: Shown are the T_e time evolution, the q time evolution and a representative profile for both of these cases. A good agreement can be seen for T_e between both the models and the experimental data. For the safety factor, the models agree well with each other with the exception that the RAPTOR model shows a somewhat faster drop in q during and shortly after the L-H transition. Both models converge to the same value. When looking at the T_e-profile, the agreement is good. For the q-profile, while the two models agree well with each other, a difference to the experimental data is observed. This difference is

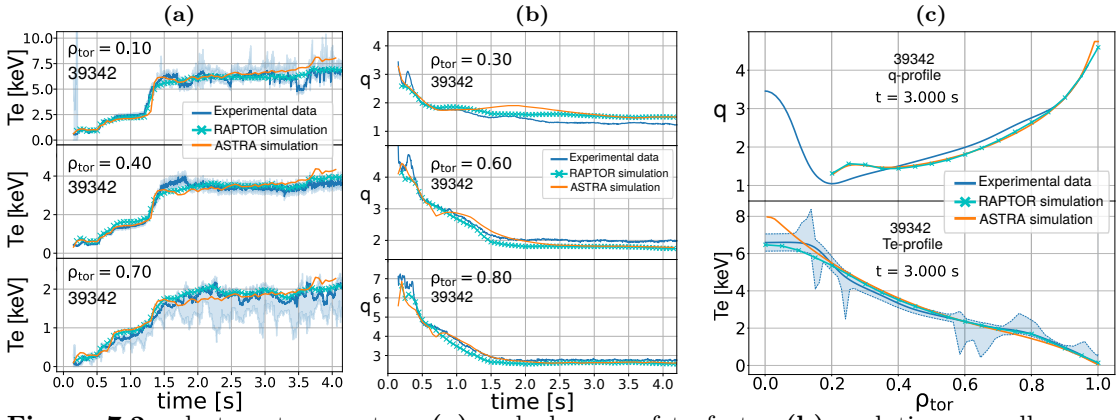

Figure 7.2: electron temperature **(a)** and plasma safety factor **(b)** evolution as well as representative profiles **(c)** for the reference scenario (39342) comparing the results of the ASTRA and RAPTOR models to the experimental data (RAPTOR data from [126])

attributed to the smoothing of the ECCD profiles in IDE, which is required to run it at all, but implies loosing some of the information. Overall, the agreement between the models is good, giving confidence in the applicability of the RAPTOR-optimizer for scenario development for AUG.

7.3 Improving the scenario

In previous campaigns, this scenario had stability issues and in the cases where it was executed successfully, NTMs were present, causing a considerably reduced confinement. The goal was therefore, to utilize the modeling framework to improve the stability of the scenario and to avoid the NTMs as much as possible. As a clearly visible local minimum close to $q = 1.5$ can be seen in figure 7.2c, a good explanation can be provided for this mode, which was previously not available due to the reduced resolution of the IDE profile.

An additional problem was that the NBI source not available for this work (mentioned in section 3.3.1) was previously used in this scenario, forcing a redesign of the heating setup. As mentioned in section 3.3.1, while the other systems are less efficient, they can replace the missing NBCD to some extent. Figure 7.3 shows the evolution of q for the reference discharge for different changes to the NBI setup. It can be seen that the loss of source 7 does not have a huge impact and can partially be replaced by source 2. Adding an additional source is not sensible, since this would increase β too much. In contrast, a loss of source 6 would have had a much larger impact. Contributing to this behavior is that source 7 was the last source being

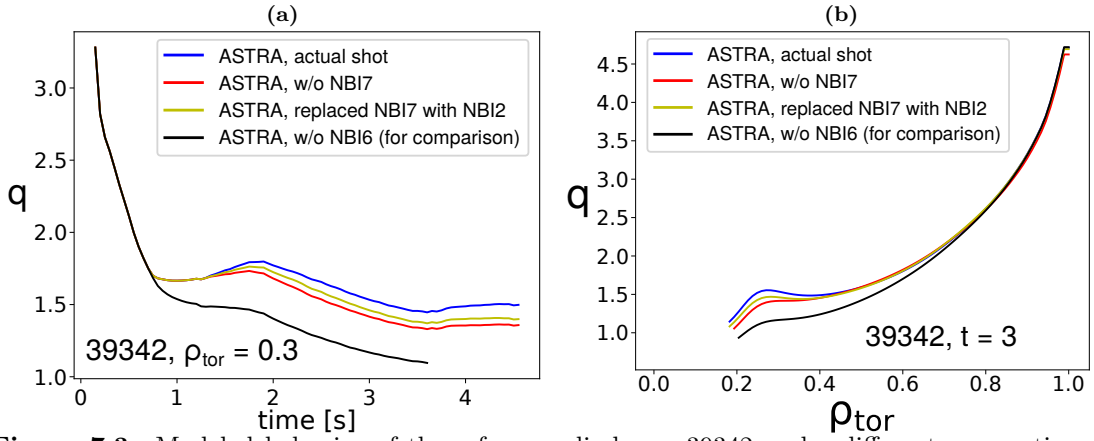

Figure 7.3: Modeled behavior of the reference discharge 39342 under different assumptions for changes to the NBI setup; Loosing NBI 6 would have been much worse

activated during this discharge. The difference in the q-profile between the setup with and without source 7 could in principle be made up for by adjusting the ECRH setup. However, since changing the q-profile is anyway of interest to remove the local minimum to increase NTM stability, the discrepancy caused by the NBI-switch is of no concern.

Using the RAPTOR-optimizer, a q-profile was designed with an increased shear at the $q = 3/2$ surface which goes through $q_{min} = 3/2$ earlier in the discharge and faster (shown in figure 7.4). The newly designed behavior compared to the previous discharge (both from RAPTOR) are shown in figure 7.4. As the NTM-stability

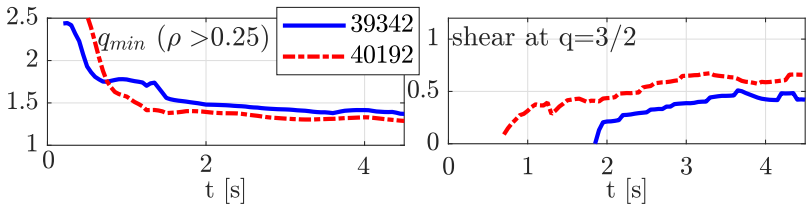

Figure 7.4: Time evolution of q_{min} and the shear at the q=3/2 surface comparing the reference discharge and the new discharge after the RAPTOR optimization (figure adapted from [126], similar to cases shown in [122])

depends on the shear at the resonant surface, this change should improve stability. The effect of moving the time of $q_{min} = 1.5$ to an earlier point in the discharge is that it would then appear at a time when β is lower, improving stability and the q-profile is higher, moving the mode inwards, reducing its effects. Additionally, a small change was done to the current ramp rate in order to improve MHD-stability

during the ramp-up.

The setup was run on AUG and the resulting behavior can be seen in figure 7.5.

When looking at the profiles (figure 7.5b) and time evolution (figure 7.5a) it can be seen that, using the same β-control, the same overall behavior is achieved after the change of the heating system. This gives confidence that the scenario was indeed reproduced. The agreement between the models is also good (As the models handle the edge differently, the agreement at $\rho_{tor} \sim 0.7$ is somewhat worse). As can be seen from the q-profile, the local minimum has successfully been eliminated. A clear improvement in confinement (see figure 7.5d) with respect to the reference discharge can be seen, while β_N remains similar. This is likely the case due to a reduced impact of NTMs. As can be seen in figure 7.5c, while the initial $n = 2$ mode is still present, it has been moved to an earlier point in the discharge and disappears without triggering another mode. No obvious impact of the mode on the confinement can be seen, indicating that the impact of it was successfully suppressed by moving the mode to lower β, by moving it earlier in the discharge, and to a lower radius. At $t \sim 2.5$s, a $n = 3$ mode, that was not optimized for, starts growing, eventually triggering a $n = 2$ mode that disappears again after ~ 1s before reappearing again. This behavior indicates a metastable situation of the scenario to the 3/2 NTM. A drop in confinement is already visible after the appearance of the $n = 3$ mode, followed by a larger drop after the appearance of the second $n = 2$ mode, which also has a clearly visible impact on the core electron temperature (figure 7.5a). Both of these values recover after the mode disappears and drop again once it reappears. This time, the mode triggers a quickly locking $n =1$ mode, disrupting the discharge. This different behavior is likely caused by the increased β at the time of this mode. As would be expected, the effect of the second and third $n = 2$ mode on the plasma is much larger as β has reached its flat-top value at that point, leading to a larger maximum size of the mode.

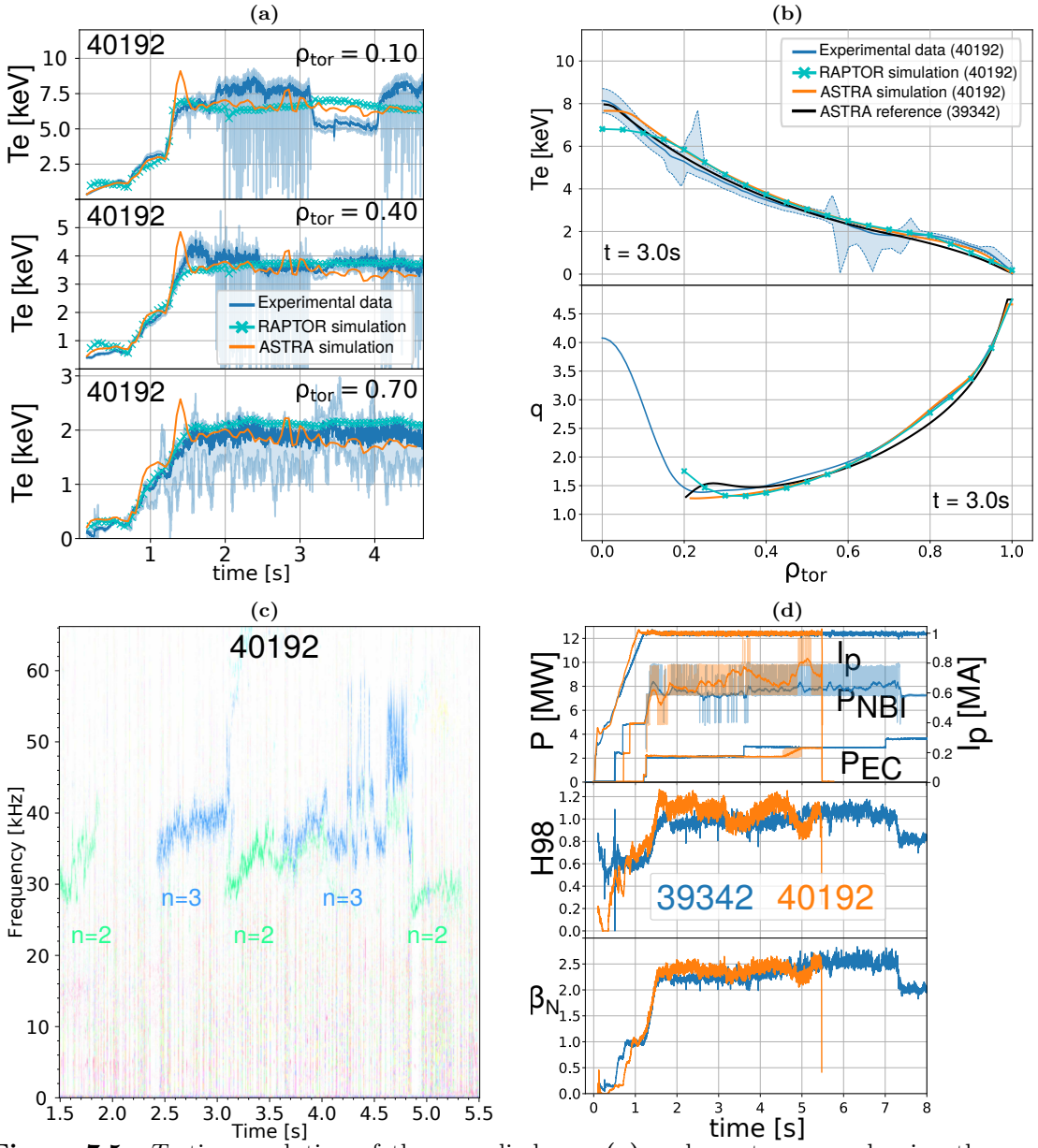

Figure 7.5: T_e time evolution of the new discharge **(a)** and spectrogram, showing the mode activity **(c)**; Comparison between the reference scenario (39342) and the new discharge (40192) of T_e and q **(b)**, and heating power, confinement (H_{98}) and β **(d)**; An increased confinement was achieved, while keeping both q and T_e behavior reasonably similar; The second appearance of the $n = 2$ mode causes a significant drop in core-T_e and confinement. (RAPTOR data from [126])

7.3.1 Further optimizations

In order to further improve the stability or at least reduce the impact of the 3/2 mode, the ECRH power was increased, in order to reduce the region of the q-profile below 1.5. The intended change of the q-profile is shown in figure 7.6.

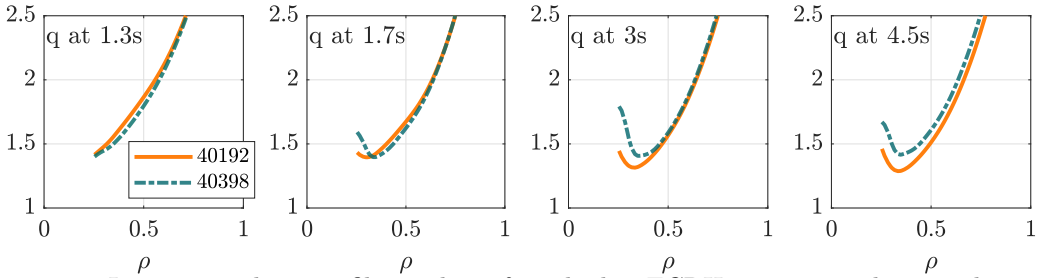

Figure 7.6: Increase in the q-profile resulting from higher ECRH power in order to reduce mode activity (figure adapted from [126], similar to cases shown in [122])

The behavior of the resulting discharge is shown in figure 7.7. The change in NBI power is due to the β controller acting to overcome different machine conditions. As can be seen in the spectrogram, the initial 3/2 modes appears at a comparable time to the previous case, again with no visible effect on confinement. The $n = 3$ mode

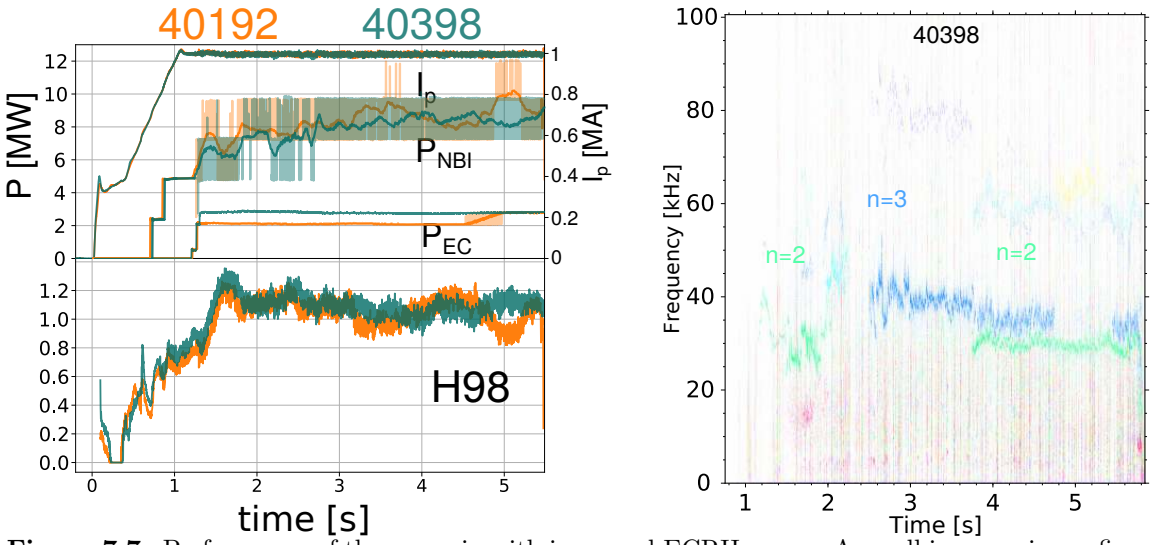

Figure 7.7: Performance of the scenario with increased ECRH-power; A small increase in confinement can be seen, as the 3/2 mode seems to drop the confinement more gradually and not abruptly as in the reference case

appears at a similar time, but the second appearance of the $n = 2$ mode is delayed by

$\sim$ 0.5s, indicating an improved stability. This is further supported by the fact that the sharp drop in confinement after the appearance of a mode is no longer present. Instead, a more gradual decrease in confinement can be seen. Overall, the discharge achieves a further improvement in confinement, although the gain is considerably lower than in the previous case.

7.3.2 Attempting to stabilize the 3/2 mode

In order to further improve the confinement, the ECRH-setup was modified in order to keep $q_{min} > 1.5$ thereby eliminating the resonance condition for the 3/2 mode. The final setup, which is used still has a time-window with $q_{min} < 1.5$ in the early phase, which disappears later in the discharge. As the initial $n = 2$ mode was seen to have an overall small impact, this was deemed acceptable. The resulting ECCD current setup is shown in figure 7.8b, comparing the result from a previous discharge (40398) with the new setup (40825). To achieve this, an additional gyrotron is added and at t =1.8s, a gyrotron aiming at the plasma core is turned off and replaced by one pointing further outwards. This change is responsible for the slight change in ECRH power seen in figure 7.9a. In later discharges, this setup is changed to moving the deposition location of a gyrotron instead of switching one off and another one on.

The target behavior of q_{min} is shown in figure 7.8a for the new gyrotron setup shown in figure 7.8b. Note, that the location of q_{min} is not constant and only values above $\rho_{tor} > 0.25$ are considered in order to avoid contamination from the required fix for the current on axis. It can be seen that the new setup with more power should now stay above q=1.5 after $t \sim$ 1.9s. Also shown is the prediction as generated by the RAPTOR optimizer. It can be seen, that ASTRA predicts a similar behavior. Before t = 1.5s there is some difference, which is consistent with findings from section 7.2, that the two models behave somewhat differently around the L-H transition. After $t \sim$ 1.5s, this difference disappears and the two models show good agreement. This is especially visible when looking at profiles (see figures 7.8 c,d,e) The remaining difference after $t \sim$ 1.5s comes from the fact, that RAPTOR uses a simplified setup to calculate ECCD. This is the reason, the RAPTOR prediction is double-checked with the ASTRA simulation.

Figure 7.9a shows an example of the performance for this discharge. It is immediately obvious that the duration of the new discharge is much shorter. This is caused by the appearance of a disruptive 2/1 NTM, that locks very quickly after appearing. This may indicate an effective trade-off in stability between the 3/2 and 2/1 modes. As can be seen in figure 7.9b, the early $n = 2$ mode is present throughout almost the

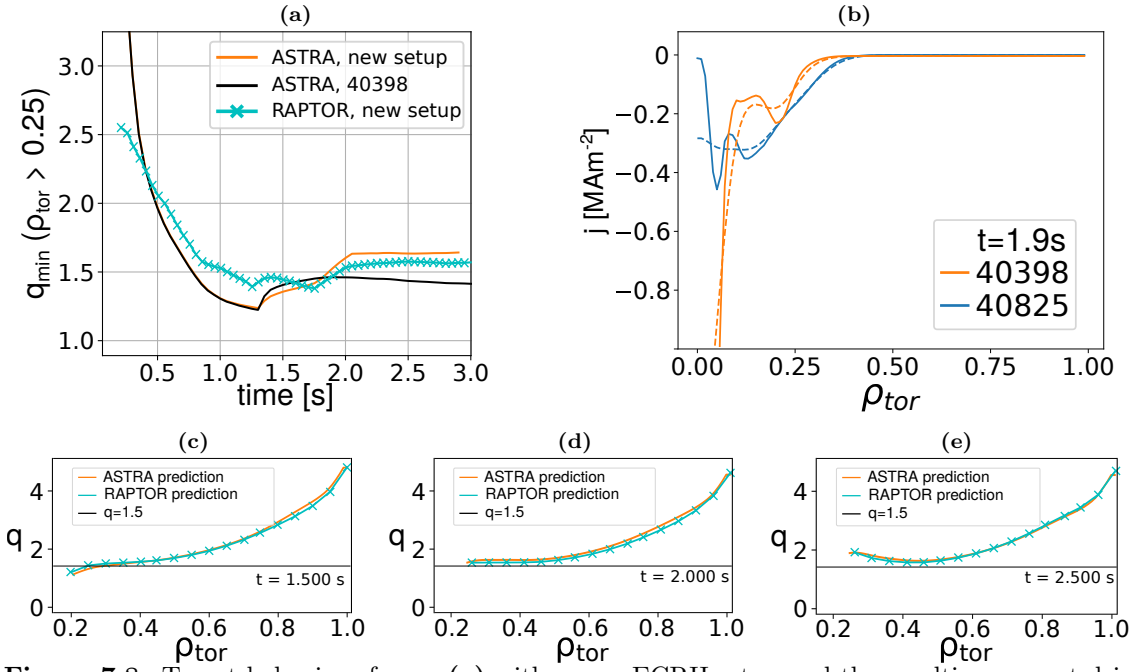

Figure 7.8: Target behavior of q_{min} **(a)** with a new ECRH setup and the resulting current drive compared to the previous scenario **(b)**; and corresponding q-profiles **(c,d,e)**

entire discharge.

The actual behavior of q_{min} as predicted by ASTRA and for comparison after running ASTRA with the actual density and heating timings from the shot, are shown in figure 7.10. The slight change in absolute values between the simulation pre and post shot comes from changes to the actual plasma density and the fact that the real heating systems do not provide exactly the same heating power as predicted. Also shown is the experimental data as generated by IDE. Similar to the situation mentioned in section 7.2, a difference between the simulated and the measured data is seen. For the same reason, this is likely due to the smoothing of the ECCD profiles in IDE. Still, the experimental data shows a similar behavior as predicted by the model, where it can be seen that $q_{min} > 1.5$ is achieved between $t = 1.5$s and $t = 2$s, which aligns with the timing of the disappearance of the $n = 2$ mode. However, as the discharge disrupts shortly after achieving q_{min}=1.5, a statement whether stable operation above q_{min}=1.5 is possible in these conditions, cannot be made.

When having a closer look at the spectrogram during such a discharge (see figure 7.9c), multiple $n = 1$ contributions can be seen. This mode appears and disappears multiple times at a comparatively small rotation frequency, before finally locking

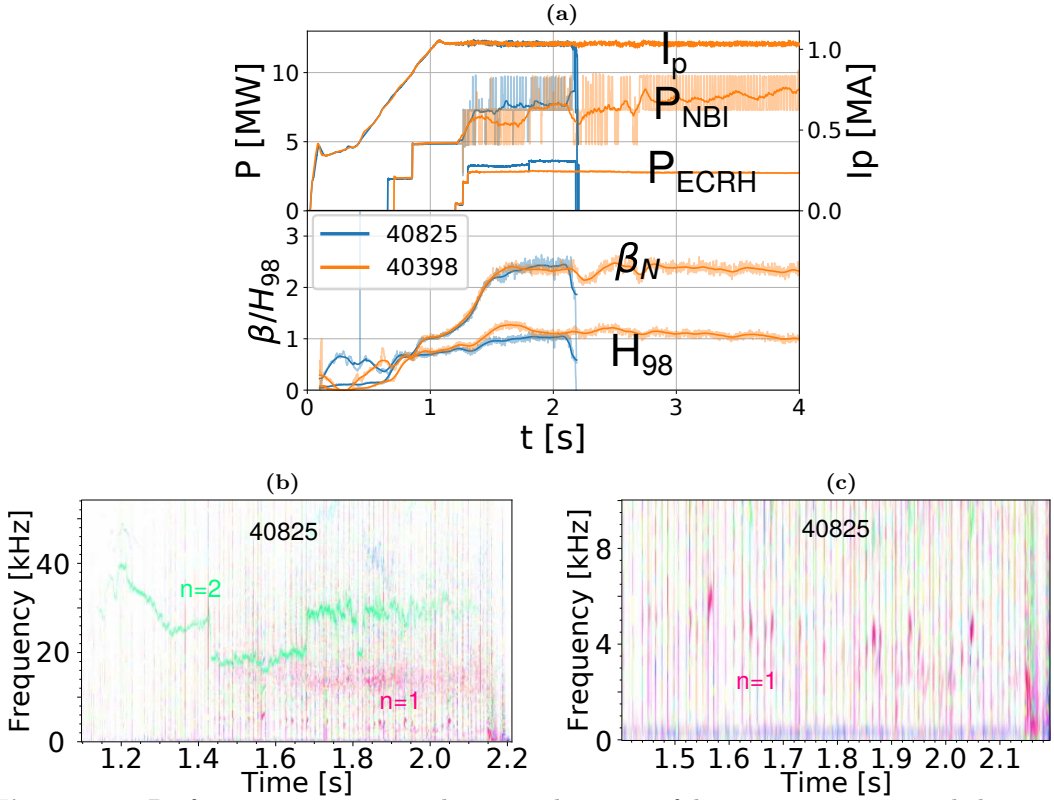

Figure 7.9: Performance comparison between the successful previous scenario and the attempted $q_{min} > 1.5$ scenario **(a)**; Spectrogram of the $q_{min} > 1.5$ scenario **(b)** and zoom into the spectrogram to better show the $n = 1$ activity **(c)**

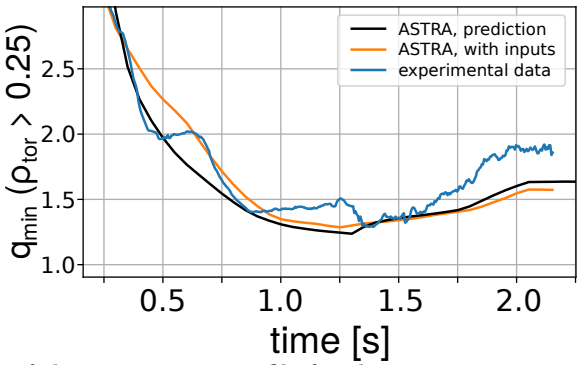

Figure 7.10: Evolution of the minimum q-profile for the scenario attempting to reach $q_{min} > 1.5$; While the agreement between experiment and simulation in worse than in previous cases, the general behavior of a phase below q_{min}=1.5 followed by an increase to a higher value between $t = 1.5$s and $t = 2$s is recovered

and causing a disruption at $t \sim 2.2$s. This behavior indicates that the scenario is metastable towards this mode with the minimum required seed island size being small. As NTM suppression by sweeping around the $q = 2$ surface is present in this discharge, the quick disappearance of the mode can be explained by the stabilizing effect of ECRH. As a real-time q-profile is not available, the location of the sweep is preprogrammed based on previous discharges and simulations. As this does not take into account fluctuations in the plasma, the deposition location is not always on target, giving the mode enough time to grow. The high frequency of occurrence indicates a high frequency phenomenon as the origin. This led to the formulation of the hypothesis that due to the proximity of the $q = 2$ surface to the edge, the ELMs can trigger a seed island of sufficient size. If this assumption is correct, moving the $q = 2$ surface away from the edge should improve the NTM-stability.

It should be mentioned that multiple unsuccessful attempts with small changes to the β-target, density and NTM-suppression at the q=2 surface were made to try and achieve a stable run of this scenario. As a redesign of the density control was required for technical reasons (see appendix A.2) between the previous discharges and the attempts at $q_{min} > 1.5$, an effect of an inferior density setup cannot be excluded.

Interestingly, this scenario does not seem to be inherently unstable. While trying to resolve an issue with the density control, an example was generated that stays mode-free (see appendix A.1). Unfortunately, this discharge does have a MARFE in the ramp-up, eliminating the reliable repeatability. The discharge recovers to comparable performance with a setup more comparable to a late-heating design. This discharge stays mode-free and reaches a high confinement, indicating that a good stable configuration can be achieved by this setup.

7.4 NTM stabilization through reduced current

By decreasing the plasma current, the q-profile is moved upwards entirely. Doing so does move the $q = 2$ surface further inwards. In order to test the hypothesis put forward in the previous chapter, the plasma current was reduced to 900kA. This increases q_{95} to ~ 4.5, which is still within the range of parameters foreseen for DEMO, although with considerably less margin. The new scenario was run, initially using the same ECRH setup as the reference case but no β feedback to avoid potentially overshooting the stability limit. It was found that the stability issues caused by the $n = 2$ mode disappear almost entirely. Similar to the procedure used in section 6.3.1, β was then optimized. The achieved performance will be presented in the next section. Figure 7.11 shows a comparison between simulated

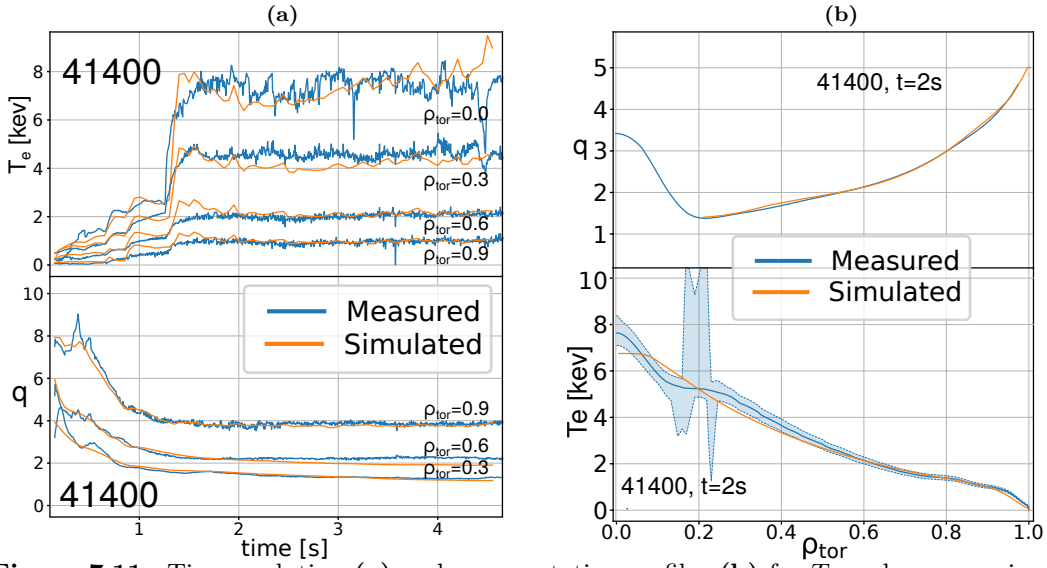

Figure 7.11: Time evolution **(a)** and representative profiles **(b)** for T_e and q comparing experimental results with the simulation; A good agreement can be seen for both

and measured data for T_e and q both the time evolution as well as some representative profiles.

A good agreement between the model and the experimental data can be seen both for T_e as well as for q. Notably a further change of the the free parameter c2H (see sections 5.3.1 and 7.1) was not required, indicating that the assumption of a dependency of this parameter on the local magnetic shear is a good candidate, as this value should stay close to the previous case, since the behavior of the q-profile is essentially the same. It is relevant to note here, that there are no previous reference discharges for this case, and the range, where the parameter does not significantly affect the agreement due to the temperature fluctuations is large enough, that the step from 1MA to 900kA may not be sufficient to see a clear difference.

The mode stability of this setup is considerably better than for the 1MA case. Figure 7.12 shows a comparison of the discharge at lower β and after the optimization. Additionally, β of two additional discharges is shown for comparison. As can be seen, the β of 41400 is in a comparable regime. Figure 7.12a reveals that the main difference of these discharges is the heating power and thereby β. The lower power discharge (see figure 7.12b) is entirely mode-free until some mode activity returns with an increase in input power, which was programmed to test the stability of this scenario. This increase in power triggers first a $n = 2$ and, shortly after, a $n = 1$ mode, disrupting the scenario. The higher power discharge (see figure 7.12c) shows

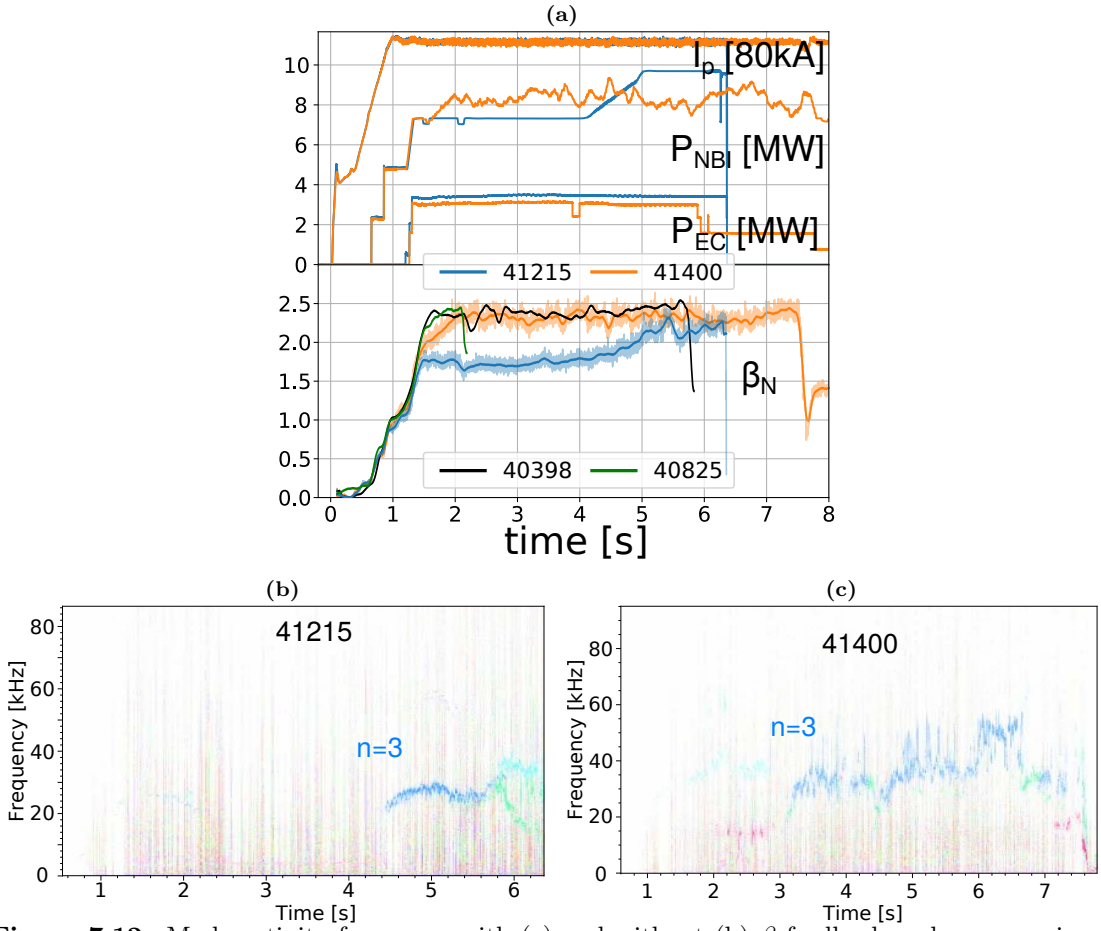

Figure 7.12: Mode activity for a case with (c) and without (b) β feedback and a comparison of the input power and performance (a)

some mode activity from the beginning, however only a $n = 3$ mode is present. This discharge develops a $n = 2$ mode and shortly after a $n = 1$ mode after the loss of two gyrotrons at $t \sim 6$s due to technical reasons.

While an improved stability in the lower β case would be expected, for the higher power case where β is increased to levels comparable to previous discharges the NTM stability remains much better than in the 1MA cases, indicating that the assumption of ELM-triggered stability issues may indeed be correct. It should me mentioned here, that the lower current may just sufficiently change the configuration, that the stability of the $n = 1$ mode is sufficiently increased to no longer appear.

The q_{min} target

In figure 7.11b, it can be seen, that the $q_{min} > 1.5$ target was not achieved. It should be noted here, that the simulation shown in this figure is using the density from this discharge and the actual heating setup as inputs. As mentioned earlier, the intended heating setup could not be realized because one gyrotron less than intended was active. An additional potential issue arises from the density. The optimization for the q-profile was done using a density similar to the one seen in discharge 40192. As can be seen in figure 7.13, the density actually present in the discharge is considerably different.

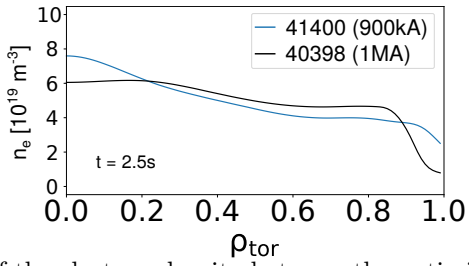

Figure 7.13: Comparison of the electron density between the optimized 900kA discharge and the earlier 1MA discharge, the q-optimization was based on

In order to test the effect of both of these differences, the simulation was run with the missing gyrotron active and with the density from 40192. The resulting effect on q is shown in figure 7.14.

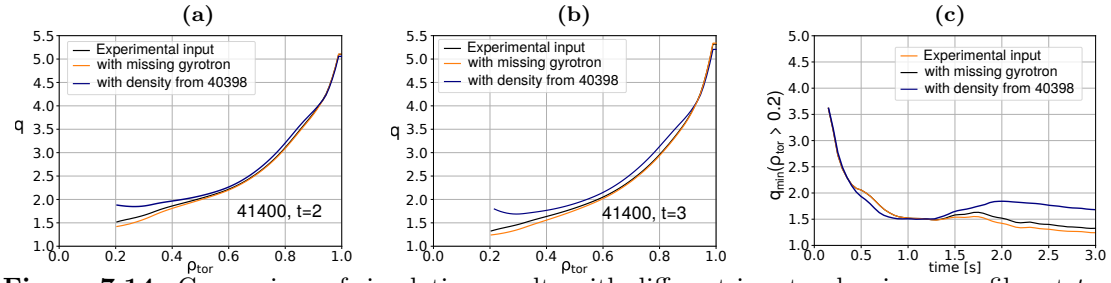

Figure 7.14: Comparison of simulation results with different inputs, showing q-profiles at $t = 2$s **(a)** and $t = 3$s **(b)** and the time evolution of q close to the minimum **(c)**

It can be seen, that at $t = 2$s, just having the missing gyrotron may have been sufficient to achieve $q_{min} > 1.5$. The exact cutoff of the reliability of the q-profile is unclear, but assuming continuous behavior, it seems likely that $q_{min} > 1.5$ would not have been achieved. Looking at the time evolution, there is a short region, where $q_{min} > 1.5$ is achieved with the additional gyrotron. However, the behavior is not

stable and q keeps dropping, yielding a q_{min} definitely not above 1.5 at $t = 3$s. In contrast to that, changing the density has a much larger effect, where after the drop around $t = 1$s, q_{min} would stay considerably above 1.5. This is the expected behavior as for an overall lower plasma current, the externally driven current makes up a larger fraction and should therefore have a larger effect.

The reason for the change in density is unclear and might be explored in future work. It does however highlight a potential weakness of the model-based approach, where it is required that the density is sufficiently similar to the reference case for the predictions to be applicable.

7.4.1 Performance of the lower current scenario

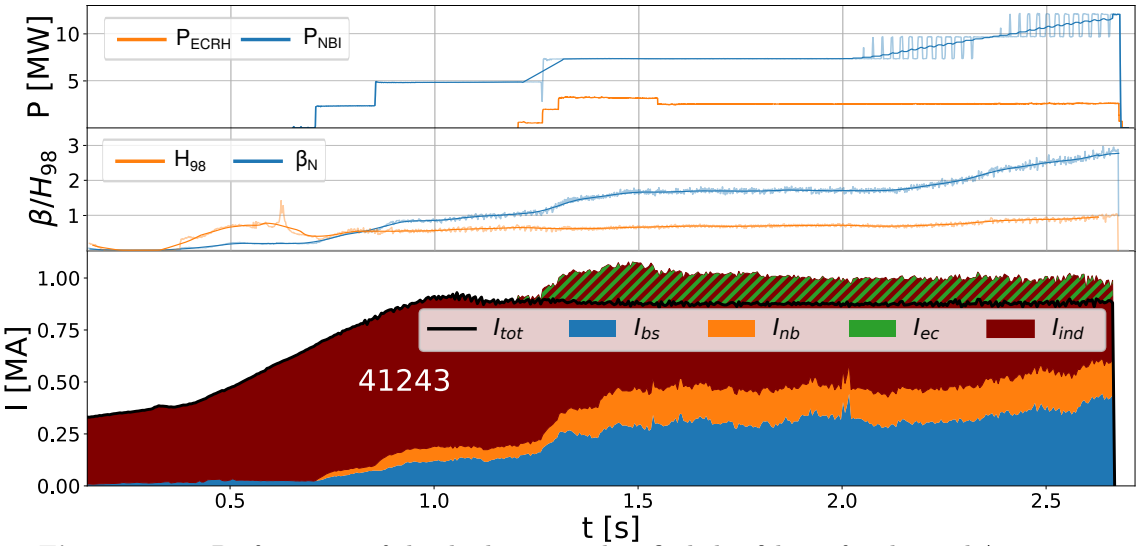

Figure 7.15: Performance of the discharge used to find the β limit for the 900kA scenario

With the same approach as in section 6.3.1 the β stability of this scenario was tested. As can be seen in figure 7.15, the NBI power was ramped up until an ideal mode disrupts the plasma at $\beta_N \sim 2.8$. Figure 7.16 shows that, similar to section 6.3.1, the mode has a very fast growth rate. This has been calculated to be $\gamma_{\text{MHD}} \sim 2.1 \cdot 10^6 \text{s}^{-1}$, yielding a $\tau_{\text{MHD}} \sim 4.8 \cdot 10^{-7}$s. As the fast ECE-system was not working for this discharge, the ECE-phase cannot be provided.

The green hatched area is the negative contribution of ECCD. Compared to the off-axis cases, the amount is much larger. Similar to the 800 kA co-current ECCD case, an increase in bootstrap current can clearly be seen at the time of the power ramp, which does agree with the β-ramp. At $t \sim 1.6$s, one gyrotron without

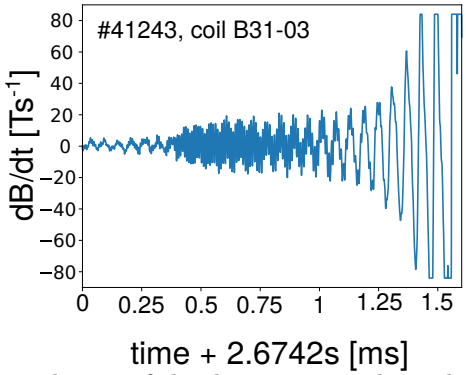

Figure 7.16: Growth rate of the disrupting mode in the magnetic signal

backup failed due to technical reasons. This had an impact on the q-profile and the overall performance of the scenario and may also affect the final β-limit. Since the motivation for determining this limit is to be able to set the control target for future discharges including a generous margin, this discharge was not repeated, in order to conserve experimental time.

The performance of the scenario, when staying below the β-limit at a value of $\beta_N \sim 2.3$, is shown in figure 7.17. As mentioned earlier, this discharge starts with one gyrotron less than intended, yielding a somewhat reduced q-profile and thereby

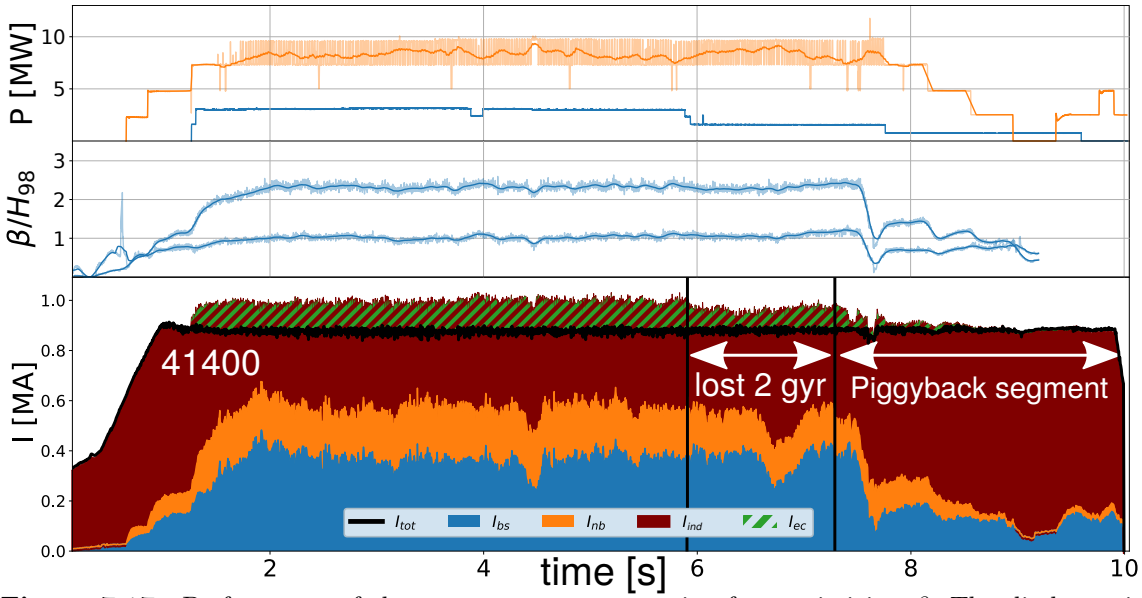

Figure 7.17: Performance of the counter-current scenario after optimizing β; The discharge is effectively lost at $t \sim 6s$, when two gyrotrons fail

bootstrap current. Still, a bootstrap fraction of 45 % is achieved in stable operation with transient peaks going up to 50%.

As explained in the previous section, shortly before $t = 6$s, a loss of two more gyrotrons caused an appearance of a 3/2 NTM, loosing stability and eventually causing a 2/1 mode to appear at $t \sim 7.5$s, after which the plasma lost most of the confinement. For the purpose of this work, the scenario is thereby effectively lost at $t \sim 6$s. The rest of the discharge is only shown for the sake of completeness.

As this discharge did not fully achieve its goal due to the initial loss of a gyrotron, repeating it to see, whether an even higher bootstrap fraction can be achieved, may be of interest for the future. This may be especially interesting in combination with a higher NBCD, if all sources are available.

7.5 Summary and discussion

It could be shown, that the model is also applicable to the considerably different scenario where ECCD is used in counter current direction when modifying just one free parameter. This gives confidence towards the general applicability of the model, although it also evidences that a reference case is required to verify free parameters, before predictions can be made. Good agreement with the RAPTOR model further increases the confidence in the results.

With a difference in the local magnetic shear, a possible explanation for the required parameter change is available, although it is unclear if this explanation is sufficient. Extending the model in future work to include this dependency may be of interest.

It was demonstrated, that the model can be used to generate alternative heating configurations for existing scenarios, potentially paving the way towards application for redesign in case of technical limitations (as it was the case in the present example).

It was found, that the confinement of the scenario can be considerably improved by relatively small changes to the q-profile, reducing the impact of confinement degrading NTMs. At the same time, complete stabilization of the offending mode was not possible at high β in the 1MA case as long as its resonant flux surface exists in the plasma. It was found that attempting to increase the q-profile above q_{min}=1.5 degraded the resistive stability of the scenario to a point, where stable operation was no longer possible, even when active NTM suppression through ECRH at the respective rational flux surface of the mode is attempted. While the plasma did follow the predictions reasonably well, the missing knowledge about NTM stability highlights a potential weak-point of the model. Including a term accounting for NTM stability might be of interest for future work.

In order to determine the stability of the scenario and exclude potential effects from the divertor neutral density, carrying out a more detailed MHD stability analysis for these cases should be considered.

It was found that decreasing the plasma current to 900kA (and thereby increasing the q-profile) leads to a significantly reduced NTM activity. This could potentially be explained by removing ELM triggered seed islands, alternatively the new profile might just be more stable towards NTMs. Again, carrying out a detailed MHD stability analysis may solve this question.

While the ideal stability limit could not be found experimentally for the 1MA scenario, since priority was given to finding a stable scenario, it was done for the 900kA case. It was found, that the ideal limit is considerably lower for the counter-current ECCD scenario, likely caused by the considerably higher q_{min} and thereby larger region of low shear. It should be noted, that the heating systems did not perform exactly as requested in this discharge and the actual limit may therefore be slightly different. While the scenario achieves a bootstrap fraction and confinement comparable to the 800kA co-current ECCD case, the considerably lower ideal β-limit (from $\sim$ 3.4 to $\sim$ 2.8) may limit the reactor relevance of such an elevated q_{min} scenario.

Chapter 8

Application to a bigger machine

While some parameters can be varied on AUG, some others, especially size, cannot. In order to gain a better understanding on how well a system can be generalized, it is usually compared to a machine of different size. In this chapter, it will be presented how the model was adapted to run for JET discharges and the results will be discussed.

8.1 Testing with older discharges

As JET is much larger than AUG and the discharges run at a higher current and a different magnetic field, the validity of the free parameters of the model were checked. This is especially relevant, as it was found (see section 7.1) that even comparatively small changes in AUG require a change of the free parameters. As the scientific goal of the discharges at JET was to find experimental evidence of the flux-pumping phenomenon ([89], mentioned in section 4.3), a new set of reference discharges was selected based on previous work [132] searching for promising candidates. As flux-pumping requires q_{min} close to one, discharges were selected, that have a q=1 surface and put sufficient heating shortly after its appearance in order to avoid the q-profile dropping further. To achieve a larger region with q close to one, a current overshoot [94] is used, meaning the plasma current is increased above the target value, kept there for some time and then ramped down to the target. This procedure generates a larger region of q close to one, which is thought to be beneficial for flux-pumping.

A new fit was done based on these reference discharges. It was found that, while all the exact values changed slightly, only c3L and c4 had no overlap with the previously found fit and therefore needed to be changed. The new values are given in table 8.1, with the values modified with respect to table 5.1 marked in red. c3L is

	c1L	c1H	c2L	c2H	**c3L**	c3H	**c4**	c5	c6	c7
mean	0.12	0.33	2.8	3.8	0.42	1.2	0.95	-	3.7	0.42
range	0.05	0.2	0.5	0.5	0.05	0.4	0.2	-	1	0.2
used	0.1	0.5	3	4	0.04 → **0.4**	1.4	0.6 → **1.0**	0.5	3	0.3

Table 8.1: The fitted values of the free parameters for the JET scenario; values that have changed from the baseline (see 5.1) are marked in red with the previous values shown in black

the prefactor for the ion heat conductivity in L-mode and c4 is a factor in the ITG threshold term. The cause for this difference is likely a dependency of the ITG on the impurity concentration, which has a stabilizing contribution thereby increasing the threshold. This effect is known from literature [133, 134], but neglected in the model. Since JET has a different wall material as compared to AUG (Beryllium instead of Tungsten), the plasma contains different impurities, meaning the impurity concentration can be different at the same Z_{eff}. This effect provides a good explanation for the increase of c4, but it is unclear if it can change the transport enough to have c3L change by a factor of 10. An influence of an additional effect seems

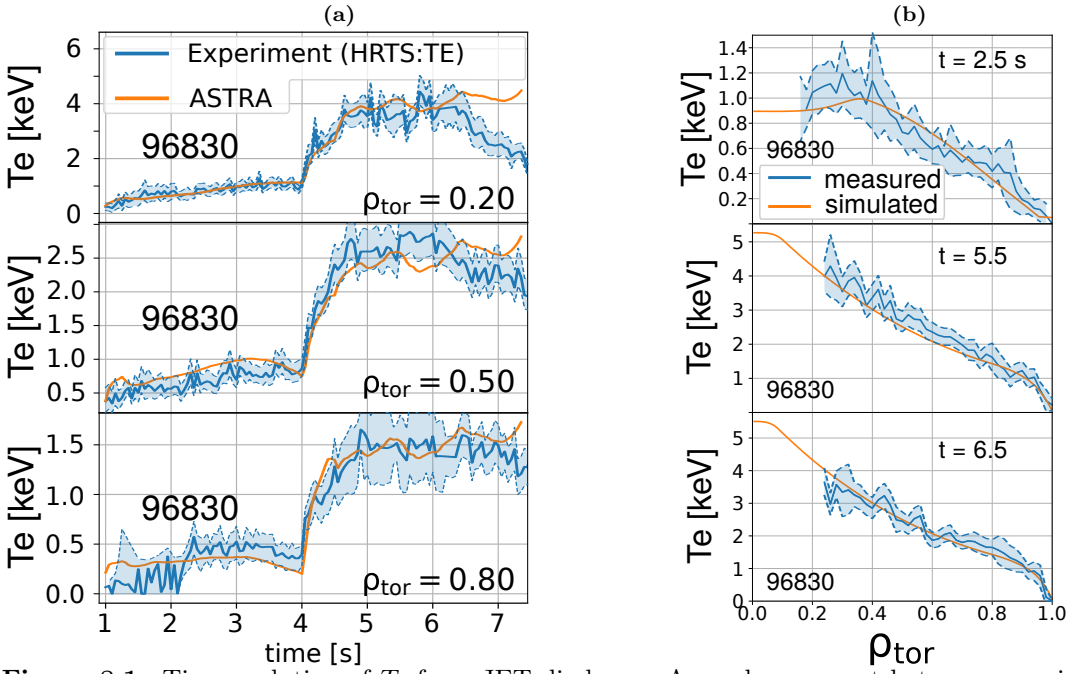

Figure 8.1: Time evolution of T_e for a JET discharge; A good agreement between experimental data and simulation can be seen. The discrepancy visible after $\sim$ 6s is caused by the appearance of a 3/2 NTM (see figure 8.3b)

likely, although a clear candidate is not available. Alternatively, the description of the transport in L-mode at the edge may not be directly applicable to the larger machine and the considerably longer time spent in L-mode, causing a difference that needs to be corrected by this parameter.

These values achieve a fit quality of $\chi^2 = 1.1$ for the electron temperature and $\chi^2 = 2.0$ for the ion temperature. This is a better quality than the values found for AUG, although it should be noted that the improvement is caused to a large part by the higher errors in the measurements at JET. A plot of the fit for each of the reference discharges can be found in appendix A.4.

Figure 8.1 shows electron temperature profiles and time evolution for one of the reference discharges. An agreement within the error bars can be seen. The profiles show that there is no experimental data inwards of $\rho_{tor} \sim 0.2$. This is due to the fact that the Thomson scattering diagnostics (see section 3.4.2) does not pass through the plasma core for the magnetic geometry used in this discharge. After $t \sim 6.5$s, a drop in the experimental core temperature, that is not reproduced by the model, is observed. This drop is caused by the appearance of a 3/2 NTM, which can clearly be seen in figure 8.3b.

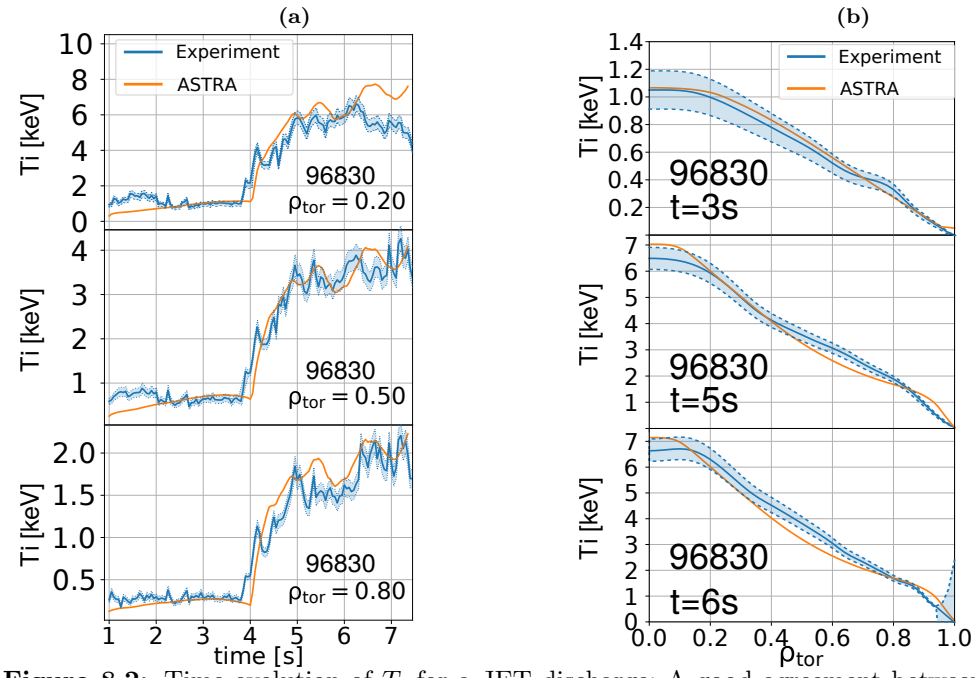

Figure 8.2: Time evolution of T_i for a JET discharge; A good agreement between experimental data and simulation can be seen. Similar to T_e, the effect of the mode appearing can be seen

Figure 8.2 shows a comparison of the simulated and the experimental ion temperature. This experimental ion temperature is deduced from a spline fit through the available data. Note that since the CXRS system does not run without the neutral beams, the error before $t \sim 4$s is likely underestimated. A reasonable agreement, for the most part within the error range, is evidenced. Similar to the T_e, the appearance of a mode causes a less good agreement for the core temperature after $t \sim 6.5$s.

Unfortunately, q-profile measurements are not regularly available at JET. For this reason, only MHD markers are available for comparison with the simulated plasma safety factor. Figure 8.3 shows q_{min} as calculated by the model and a spectrogram of the mode activity for the same discharge. As can be seen, the timing of the $n = 1$ mode in the experimental data at $t \sim 4.2$s is compatible with q_{min} crossing one in the modeled behavior.

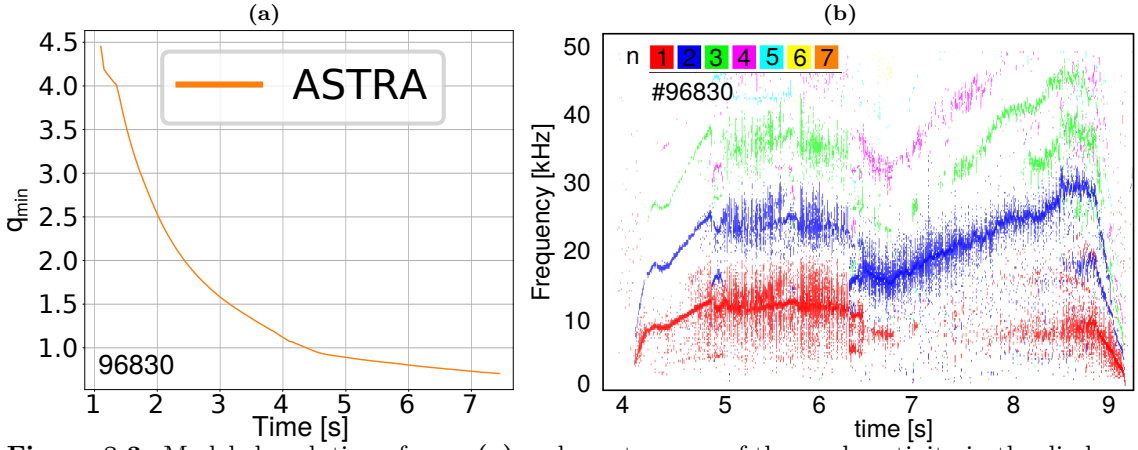

Figure 8.3: Modeled evolution of q_{min} **(a)** and spectrogram of the mode activity in the discharge **(b)**; The timing of $q_{min} \sim 1$ agrees with the experimentally observed mode activity

Another available option is to determine the location of the 3/2 mode, which is clearly visible after $t \sim 6.5$s, where the $n = 1$ mode disappears. As can be seen in figure 8.4 this is also compatible with the simulation. The q-profile generated by the simulation is shown in orange, with the abscissa set to major radius. It can be seen, that the q=1.5 surface lies inside the region where the ECE-phase (shown in blue with marked data-points linearly connected) has a clearly visible phase-jump (region marked in orange).

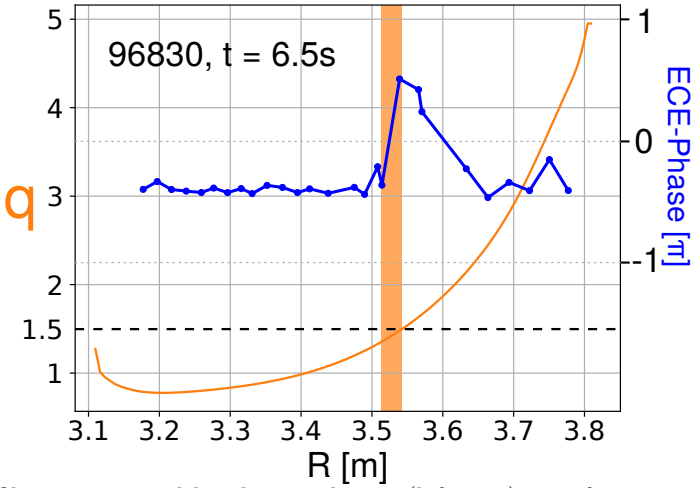

Figure 8.4: q-profile as generated by the simulation (left axis) as a function of major radius and corresponding ECE-phase (right axis) with points linearly connected. The region of the phase jump is shaded in orange.

8.2 Potential issues

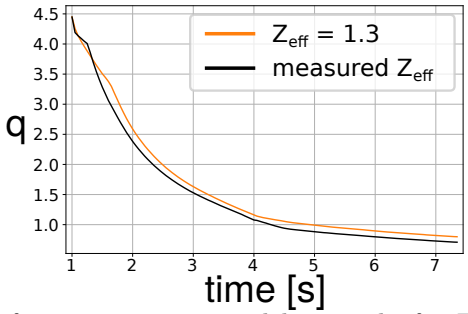

Figure 8.5: Time evolution of q_{min}, comparing modeling results for Z_{eff}=1.3 with the experimental data; A relevant difference of $\sim$ 0.5s at the time when q=1 is reached is observed

In contrast to discharges at AUG, it was found that Z_{eff} has a relevant effect on the q-profile as can be deduced from figure 8.5. Here, the time, when the q=1 surface is reached, differs by more than 0.5s between the simulation and the experimental data, which is considerably more than the effect observed for AUG-discharges. This shows, that the assumption that for Z_{eff} any reasonable value could be selected, is no longer valid and for predictive simulations, a suitable impurity modeling would need to be included. While an impact could also be seen for the AUG case, it was much smaller than in the JET case and disappeared after heating start. A possible explanation for this is that the q-profile at AUG is largely determined by ECRH after

the heating starts, and the early phase is short enough that the effect of Z_{eff} stays small. In contrast, the larger volume of JET and thereby longer initial phase allows the impact of Z_{eff} to grow large enough to no longer be negligible. As the external current drive on JET is only NBCD, which depends on Z_{eff}, the difference does not disappear after heating starts.

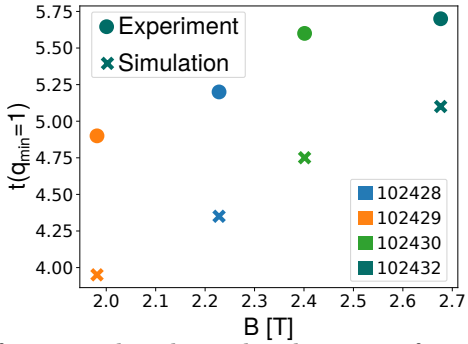

Figure 8.6: Comparison of measured and simulated timing of q_{min}=1 for a set of pulses with different magnetic field; While the trend is reproduced, absolute values are considerably different

Figure 8.6 shows a comparison of the simulated and measured timing of the appearance of the q=1 surface for a set of consecutive pulses with different magnetic field. While the overall trend between the discharges is reproduced, a considerable difference in the absolute values ($\sim$ 1s) can be seen.

The inaccuracies can in principle be corrected by scaling the neoclassical conductivity during the ramp-up, such that the timing of the q=1 surface agrees with experimental data. This could potentially make q-profile simulation usable however, the relevance of this is questionable as the accuracy of the simulation cannot be verified. Additionally, while the required change is constant for consecutive discharges, it is not constant for longer time-scales.

This behavior potentially aligns with findings from [135], where it was found, that neoclassical conductivity seems to not reliably describe the current ramp-up phase at JET. However, as there are pulses with a better agreement, this explanation seems unsatisfactory. Alternatively, variations in the machine conditions, having effects on the q-evolution, may explain the different behavior between discharges with a significant time in between. As there are no conclusive measurements at the time of writing, an effect of the Z_{eff}-profile cannot be excluded.

It has been seen in [136] that initial q profiles at JET can be very high. In order to judge the corresponding effect, a study was carried out, testing various different options for the q-evolution. The results are shown in figure 8.7.

The black curve shows the result assuming the initial low fidelity q-profile from

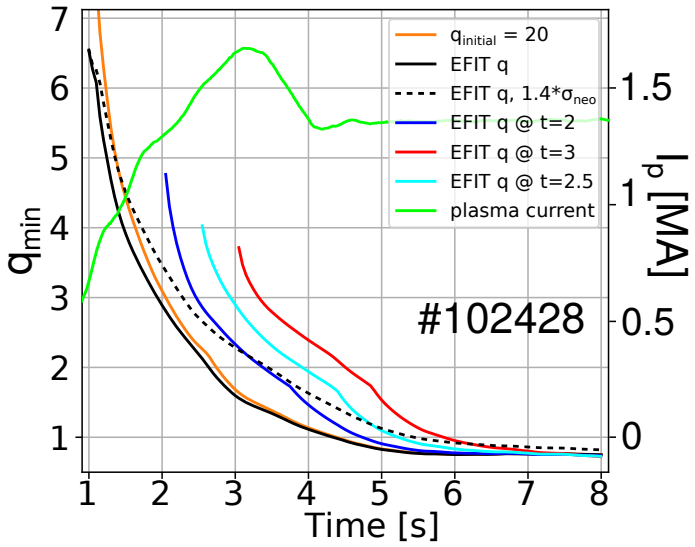

Figure 8.7: Various tests for discharge 102428 to see what is necessary to reproduce the experimental q_{min}=1 timing; at t=1s, the initial q has very close to no effect; at later points the impact of the effect increases; For comparison also shown is the effect of increasing the neoclassical conductivity by a factor of 1.4; For reference the plasma current is also shown

EFIT (see section 3.5.3), and the orange curve shows the behavior if the initial q-profile is set to a flat q=20. It can be seen that even for very high values the impact of the initial q on the q=1 timing is very low. For comparison, the plasma current is also shown. Note that no major change was made to the plasma current with respect to the earlier reference discharges. While Z_{eff} does have an impact on the q=1 timing, to reproduce the experimental result by only changing Z_{eff} would require a value below one. The black dashed line in the figure shows the behavior, using the initial q-profile from EFIT with the neoclassical conductivity scaled by a factor of 1.4, such that the q-evolution matches the observed q=1 timing.

In order to determine the required change to achieve the correct q=1 timing, the start of the simulation was delayed to a later time-point with the same initial q-profile. As q_{95} is fixed by the plasma current and the magnetic field, the minimum drops quickly to the value seen in the figure. It turned out that, in order to reproduce the experimental behavior of q_{min}=1 at $t \sim 5.2$s, the initial q would need to be delayed to $t = 2.5$s. This would indicate a q_{min} of ~ 4 at $t = 2.5$s, which is reasonably close to the value of q_{min} slightly below 6 seen in [136] at $t = 1.4$s. Such a behavior would be a plausible explanation for the experimental results [137], but it essentially eliminates any predictive capability of the model if no information on the initial q-profile is available.

8.3 Discussion

When applying the model to JET discharges, it was found, that it reproduces well both, the ion and electron temperatures for the analyzed set of reference discharges. To achieve this result, a change of only two free parameters was required, both of which affect the ion temperature and one only affects the L-mode. The reason for the need of theses changes is likely a dependency of the ITG on the impurity concentration, which is not included. The change to the L-mode parameter is large enough, that an additional dependency seems likely, although a clear candidate is not available. Notably, a change of the TEM threshold (as required in chapter 7) is not necessary. While this suggests that the local magnetic shear is sufficiently similar between these cases, as many parameters change when switching machines, counteracting influences cannot be excluded.

In order to gauge the exact dependencies of these parameters, a set of reference cases with a larger range of input parameters would be required. To this end, some work has already been done on AUG [123] which might be included in future upgrades of this model. With the new set of free parameters, the experimental behavior is well reproduced, indicating that the model can indeed be generalized to larger machines, provided that some reference data is available for validation and tuning of the free parameters.

The situation regarding the q-profile is unfortunately much less clear. While the initially considered discharges show a good agreement with MHD-markers, later cases exhibit a discrepancy. The most likely explanation seems to be that the initial behavior of q is not consistently reproduced, possibly caused by varying initial conditions or by a transport behavior in the early phase which is not fully understood and therefore not included. The initially matching behavior of q was thus likely just a coincidence. Since it was found that trends between consecutive discharges are reproduced and the correct evolution of q can be recovered by adapting the neoclassical conductivity, data from one discharge may be used to generate useful predictions for the subsequent discharges. With information of available MHD-markers, the timing of q reaching the given value can be adjusted such that an estimation of the q-evolution can be provided after each discharge. In absence of a predictable explanation for the discrepancy of the q-evolution, or some information on the behavior of q early in the discharge, general predictions can not be made.

In contrast to AUG, it was found, that the impact of Z_{eff} is no longer negligible. This discrepancy can likely be explained by the larger machine size and thereby longer current diffusion time giving the effect more time to develop, whereas it disappears at AUG after the heating starts, as the q-profile is then largely determined by ECRH.

In order to do predictive simulations it would therefore be required to include an impurity transport model to simulate the evolution of Z_{eff}. As Z_{eff} mainly depends on machine conditions, which tend to stay similar between consecutive discharges, and as the simulation of q requires input regarding the previous discharge anyways, using data from previous discharges for the Z_{eff} evolution may be sufficient.

Chapter 9

Summary and Outlook

Using the ASTRA framework, a model capable of predicting the behavior of temperature and safety factor has been developed. The required inputs for this model are the actuator setup, which is simulated, and the plasma density. The model has proven to be a very useful tool for the development of early heating AT scenarios by describing the q-profile in the current ramp-up phase, allowing to select the appropriate heating systems such that a targeted q-profile can be achieved. With this tool, a large part of the iterative approach usually present in the development of AT-scenarios can be moved to computational modeling only, allowing to both save experimental time and test potentially interesting configurations, that might otherwise be too hard to achieve. Using this approach, a high performance scenario achieving a bootstrap fraction of $\sim 50\%$ and a non-inductive fraction of $\sim 90\%$ was developed.

For the simulation of the electron and ion temperatures, a simple Bohm/gyro-Bohm model including simplified ITG and TEM terms is used in order to achieve a run-time short enough to enable the realization of the numerous iterations required for scenario design while keeping the overall calculation time at an acceptable level. This model includes multiple free parameters, which have been fitted based on a set of reference discharges, achieving a very good fit for T_e and an acceptable fit for T_i. It has been shown that the impact of the ion temperature on the safety factor is low. The initial set of reference discharges was chosen such that as many parameters as possible are already close to the targeted setup. Here it was found, that the deduced free parameters do not vary between discharges, which gives confidence towards the applicability of the model for predictive simulations.

Tests of the model for different setups and even a different tokamak have been carried out. In both cases it was found that not all of free parameters stay constant.

Staying at AUG, but increasing the plasma current from 800kA to 1MA, and using a more central ECRH heating setup to achieve a higher q_{min}, turned out to require a change of one of the free parameters affecting the electron temperature. No additional change was required when reducing the plasma current to 900kA while keeping a very similar heating setup. The most likely explanation for this observation is a dependency of the TEM threshold on the local magnetic shear, which is not included in the model. This would be consistent with the finding, that a further adjustment of the relevant free parameter is not required after lowering the plasma current, since the shape of the q-profile does not change. On the other hand, the second change of the plasma current may not have been large enough to generate a difference, distinguishable beyond the usual fluctuations. This is particularly relevant, since a large set of reference discharges was not available for these cases.

Going to the JET tokamak, a change to two parameters was required, both affecting the ion temperature, but one of them only in L-mode. The reason for the required change is likely the dependency of the ITG stability on the impurity concentration, which is not included in the model. The required change of the L-mode parameter is large enough, that an additional dependency seems likely, although a clear candidate is not available.

It is promising that after the free parameters are adjusted, no further change is required to correctly describe similar discharges. This shows that the model includes the most relevant physical processes and therefore is capable to accurately describe the transport behavior in these cases after the adaptation of the free parameters.

Switching the transport description to a neural network supported version of a higher fidelity model (such as [138]) could potentially eliminate the reliance on free parameters and further improve the agreement with the experimental behavior, while preserving the fast run-time. Implementing such a setup was considered. However, at the time of developing the presented system, a version trained on a parameter set relevant for advanced scenarios was not available. Once such a version becomes available, implementing it would be of interest. Alternatively, a more extensive model, including more physical effects and using a larger set of reference discharges [123], has recently become available. This model does include the missing dependencies mentioned above as the likely cause for the required parameter changes. However, it also features a much larger set of free parameters. Implementing this model would be a possibility, alternatively, starting by including additional parameters describing the processes identified to cause discrepancies, may be a better approach.

The model has successfully been employed to guide a path to a new advanced scenario at AUG, operating at $q_{95} \sim 5.2$ (corresponding to 800kA) using the early-heating approach. This scenario was found to reach a bootstrap fraction of close

to 50%, operating at $\beta_N \sim 2.7$ with $q_{min} \sim 1.3$ and a relevant confinement of $H_{98} \sim 1.05$. The ideal limit of β for this scenario has been found to be higher at $\beta_N \sim 3.2$, but above $\beta_N \sim 2.7$, the scenario was found to be increasingly unstable to NTMs. In the high performance discharge, this resistive limit was lower than in previous discharges, likely due to a change in the transport behavior caused by an intermittent drop in heating power. Testing whether stable operation at higher β can be sustained is an interesting topic to consider for future campaigns. This is especially relevant since the discharge with the highest bootstrap fraction did not have the full off-axis NBI-power available. Based on the increase in externally driven current observed in a previous discharges, with the full power fully non-inductive operation may be achievable in this scenario.

In order to be able to improve the actuator setup for a targeted q-profile, an optimizer running in the RAPTOR fast transport solver has been employed. Aiming at verifying its applicability, a comparison with a similar model running in said solver has been implemented, showing a good agreement. This result gives confidence for the reliability of the ASTRA model.

A secondary scenario at AUG, utilizing a higher current (1MA) and a counter-ECCD current drive setup to be able to achieve sufficiently high q-profiles at a more reactor-relevant $q_{95} \sim 4.1$ was also investigated. Starting from a reference case in a previous campaign, using the optimizer to increase the magnetic shear at the q=1.5 surface, a considerable improvement in confinement was achieved by suppressing $n = 2$ NTM activity. The mode could however not be completely removed while keeping a q=1.5 surface in the plasma. Increasing the q-profile to stay above q_{min}=1.5 was found to be unstable with respect to a disruptive 2/1 NTM.

Currently, a control system based on real-time q-profiles is under development for AUG. This system is expected to improve NTM stability by giving more precise control over active NTM suppression. A revisit of this scenario will be interesting once this system becomes available in the future.

To avoid the stability issue related to the disruptive 2/1 NTM, the plasma current was decreased to 900kA in order to move the resonant surface of the disruptive mode away from the edge. While this increases q_{95} to ~ 4.5, a remarkable improvement in general mode stability at a similar β could be observed, with the previously problematic $n = 2$ mode no longer present, even though $q_{min} > 1.5$ was not achieved. The reason for the latter turned out to be a different density profile than expected, in addition to technical difficulties with the heating systems. The origin of the different density is unclear and should be explored in future work. Due to a lack of available discharges, it could not be tested if the different density was caused by a systematic problem or if it is a feature of the scenario.

Work on this scenario is anticipated to continue in a future campaign to see if stable operation at such an elevated q-profile is possible, especially with all heating systems being operational as requested. A tentative ideal stability limit of this scenario was found at $\beta_N \sim 2.8$, however the determining discharge did not have the exact heating setup as requested for technical reasons, and will likely be repeated in the future. Even with one gyrotron less than intended, this scenario reached a bootstrap fraction of $\sim 45\%$ with a good confinement of $H_{98} \sim 1.05$. As the counter current ECCD increases the required inductive current to sustain the scenario, evaluating the non-inductive fraction, does not make sense.

In order to further evaluate the NTM-stability of this scenario and to increase the performance, operation at a plasma current in between the two tested cases such as 950kA is planned for future campaigns. The lower NTM stability at higher current was thought to be potentially caused by ELM triggered large seed islands, which are reduced when the resonant surface is moved inward at lower current. An alternative explanation could however also be that the q-profile at lower current is just more stable towards the offending 2/1 mode. In order to resolve this question, carrying out a detailed MHD stability analysis for these cases may be of interest.

Comparing the counter-current ECCD scenarios to the co-current cases it can be seen, that this setup allows to achieve a similar bootstrap current fraction and a higher total plasma current and thereby confinement. At the same time, the higher current scenario has considerably more problems with NTMs affecting the confinement and removal attempts were not fully successful. Reducing the current was found to significantly improve NTM stability, giving a promising path to further explore the parameter space. While an experimental analysis of the ideal β limit in the 1MA case was not be carried out, consistent operation only slightly below the 800kA cases (~ 2.55 instead of ~ 2.7) indicates it to be similar to the 800kA case. For the scenario with increased q_{min} at higher current the limit was investigated and found to drop from ~ 3.4 to ~ 2.8, which may limit applicability of this approach towards reactor operation. It needs to be noted here that the test discharge was affected by technical issues and may therefore not be representative. The reduced limit is expected from the elevated q-profile and highlights the trade-off between achievable β on one side and confinement and bootstrap current on the other in these scenarios.

As the dependency on the plasma density is potentially a weak point, an alternative approach, utilizing the actual control parameter as an input, is in principle available (see appendix B). However, this approach includes a fit with a very low coefficient of determination. Further expansion of this density model by finding a better scaling to describe the data and then doing a proper fit of the free parameters

of the transport model, would be of interest for future developments.

The stability with respect to NTMs was found to be a relevant factor for a large number of the discharges realized during this work, and it was found that the relatively simple stability consideration to take the impact of magnetic sheer into account, yields clearly visible improvements of the results. Therefore, a future expansion of the model should include a NTM stability term. Such an implementation would reduce the risk of producing a scenario not sufficiently stable towards NTMs to be experimentally relevant. Alternatively, carrying out a MHD stability analysis on profiles predicted by the model may be a potential solution.

In order to further generalize the model, tests were run for JET discharges. As mentioned previously, two free parameters needed to be changed, after which a good agreement for the temperature was achieved. Initial comparisons of the q-profile simulation to experimentally observed MHD-markers also show good agreement. However, a considerably worse situation was found for later discharges. While trends in the behavior of q are correctly reproduced for discharges initiated shortly after one another, absolute values are not reproduced. This different behavior would point to a possible dependency on machine conditions, causing the early q-profile to behave differently. Alternatively, this behavior would also align with findings from other studies stating that the JET ramp-up is not fully described by neoclassical conductivity. In contrast, this second option does not explain why in some cases a good agreement can be seen. In either case, the inconsistency in the behavior shows that the model cannot be used to predict q-profile evolution at JET. As consecutive discharges were found to show consistent behavior, predictions could be possibly based on a reference discharge with an additional free parameter in the neoclassical conductivity. This may be of interest for inter-discharge considerations. Additionally, it was found that, in contrast to AUG, where its effect is negligible, Z_{eff} can no longer be neglected. Introducing impurity transport to simulate the Z_{eff} evolution would therefore be a requirement for general application of the model.

The model offers the possibility to design new scenarios or make informed changes to existing ones. Both of these cases have been demonstrated during this work. While only application at AUG and JET has been demonstrated, in principle the setup can easily be adapted to different machines, given the required inputs are available. In addition, as the heating setup is not limited to an existing setup, alternative configurations can be tested. While currently only ECRH and NBI heating are included, the modular nature of ASTRA does allow simply adding other systems. This was not relevant for the work done here, but for future studies adding alpha-heating through fusion or additional current drive sources would allow to study potential setups for future machines. An arbitrary amount of heating power and/or

heating systems could be used in order to test effects of such a setup. This approach could be applied for design studies regarding future machines or heating system upgrades. In addition, for a given amount of heating power, different configurations can be tested in order to gauge trade-offs between bootstrap fraction and achievable confinement. Such an approach would however require additional inputs on NTM and ideal β stability. As it was found that the free parameters are not constant between sufficiently different scenarios, some reference cases would be required if a completely new scenario or a different machine was considered. During this work, only reference data from previous discharges was used. Data from high fidelity simulations should provide a comparable result, which opens up the possibility to apply the models to setups which are not possible to test experimentally.

Appendix A

Additional Information

A.1 A mode-free 1MA discharge

While working on the 1MA scenario, a potentially interesting discharge was discovered: Discharge 41102 has too much gas in the beginning due to a technical issue causing an erroneous reading for the density feed-back control in L-mode. This causes the appearance of a MARFE during the ramp-up, which is evidenced by the density spike at $t \sim 0.8$s in figure A.1a. It disappears quickly after the second NBI beam is turned on, but still has a significant effect on the discharge as can be seen in the considerably lower confinement shown in figure A.1b in the middle.

Since both β and the density are feedback controlled, the control system is able to stabilize the discharge, which reaches a confinement level comparable to previous discharges after around 4s. While the appearance of a MARFE makes this scenario not reproducible, it is still interesting because it is completely mode free as can be seen in the spectrogram shown in figure A.2a. The safety factor (see figure A.2b) is similar to previous results, at least in the second part of the discharge, indicating that this scenario is still comparable, while the bootstrap current is comparable as well, if not larger. Interestingly, the electron temperature stays at a higher level than the reference, likely due to the missing NTM and slightly higher input power.

While the increased density, as well as the reduced confinement and β caused by the MARFE might explain an improved NTM stability, reappearance of modes would be expected once these parameters return to values seen in previous cases. Since the discharge remains mode free at this point, it seems reasonable to assume that a a mode-free configuration was achieved. While this case behaves similar to a late-heating approach and the performance in the early phase is poor, it implies the existence of a stable regime. It should therefore be possible to achieve a similar

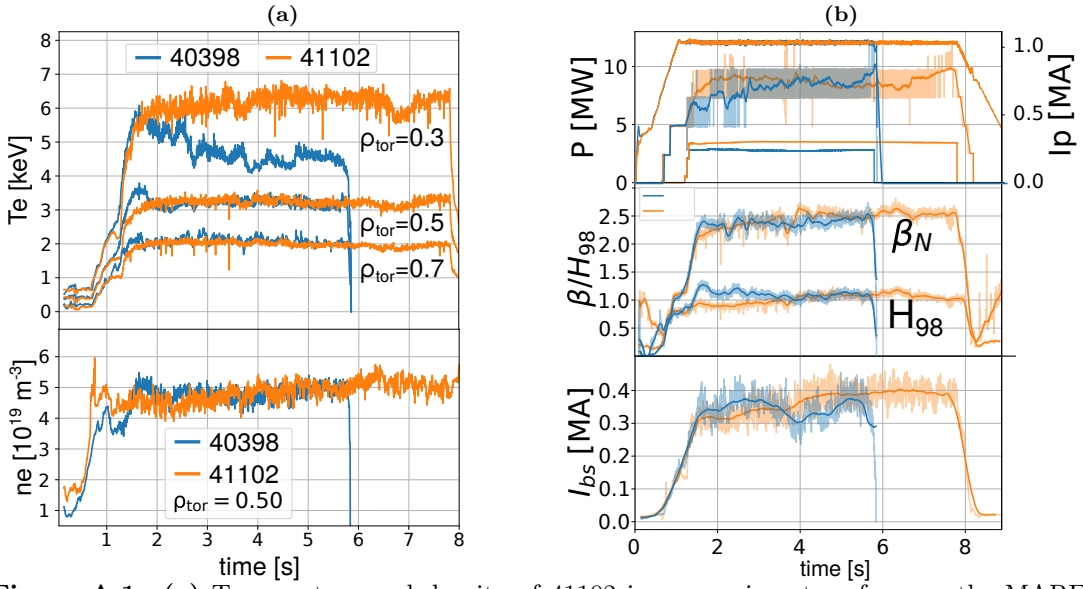

Figure A.1: **(a)** Temperature and density of 41102 in comparison to reference, the MARFE is responsible for the density spike between 0.5 and 1 s is; **(b)**: Comparison of heating setup, β_N, H_{98} and bootstrap current between 41102 and a previous discharge without issues (40398)

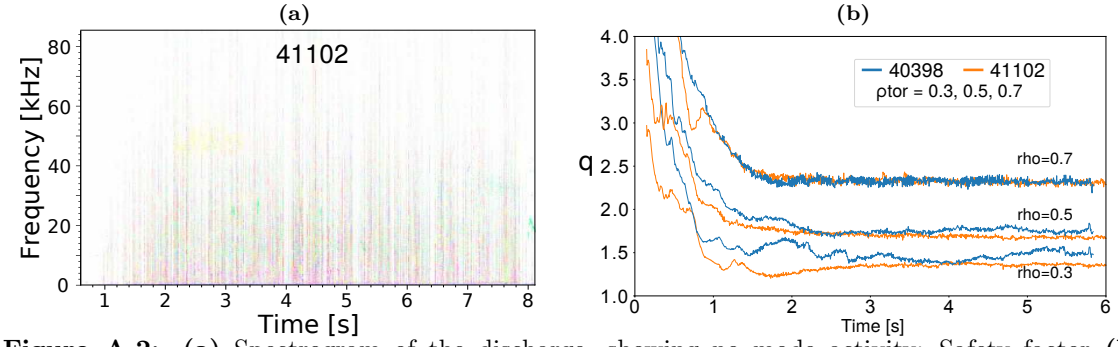

Figure A.2: **(a)** Spectrogram of the discharge, showing no mode activity; Safety factor **(b)** comparison of the discharge to a previous reference with no MARFE

result in a more reproducible configuration in the future.

A.2 An issue with the divertor neutral pressure

Usually at AUG the manometer number 4 (see section 3.4.6) is used for measurement of the divertor neutral pressure $n_{0,div}$. During the discharges performed for this work, an issue was encountered, where the behavior of this manometer changed with respect to a different manometer.

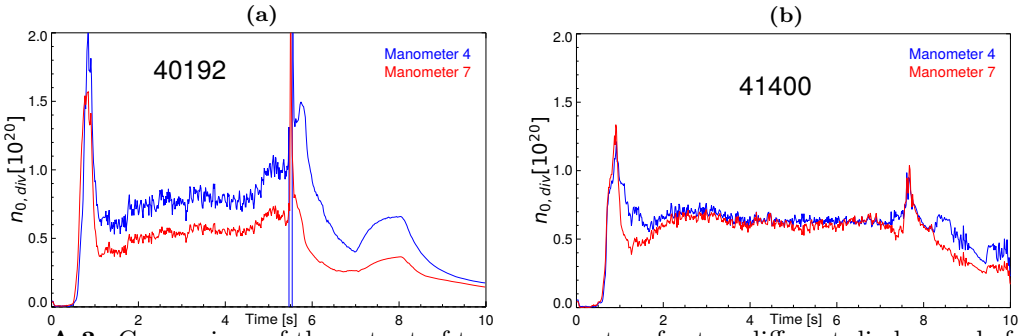

Figure A.3: Comparison of the output of two manometers for two different discharges before **(a)** and after **(b)** a clear change in behavior can be seen

Figure A.3 shows a comparison of the data from two manometers for a discharge before and a discharge after the change in behavior of manometer 4. It can be seen, that the measured density on manometer 4, while not changing substantially has considerably dropped in relation to manometer 7. As the density feedback for the discharges performed during this work rely on this quantity, a redesign of the control target was required. For the new setup, data from the manometer 7 was used. Although a similar performance was recovered, the stability issues observed during the 1MA discharges trying to achieve $q_{min} > 1.5$ (see section 7.3.2) may be in part caused by this redesign.

A.3 Performance of noteworthy discharges

Nr	q_{95}	$H_{98,max}$	$H_{98,av}$	$\beta_{N,max}$	$\beta_{N,av}$	$f_{bs,max}$	$f_{bs,av}$
39221	5.2	1.15	1	2.8	2.5	50%	41%
40403	5.2	1.2	-	3.2	-	60%	-
41086	5.2	1.15	1.08	2.9	2.7	52%	46%
40398	4.1	1.2	1.1	2.6	2.4	43%	36%
41102	4.1	1.2	1.1	2.7	2.55	45%	40%
41243	4.5	1.05	-	2.8	-	45%	-
41400	4.5	1.15	1.05	2.55	2.3	49%	43%

Table A.1: Performance characteristics for discharges mentioned, max refers to the maximum encountered value, av refers to average values during a stationary phase (not present for discharges to find β-limit)

A.4 Parameter fit

A.4.1 AUG, 800kA scenario

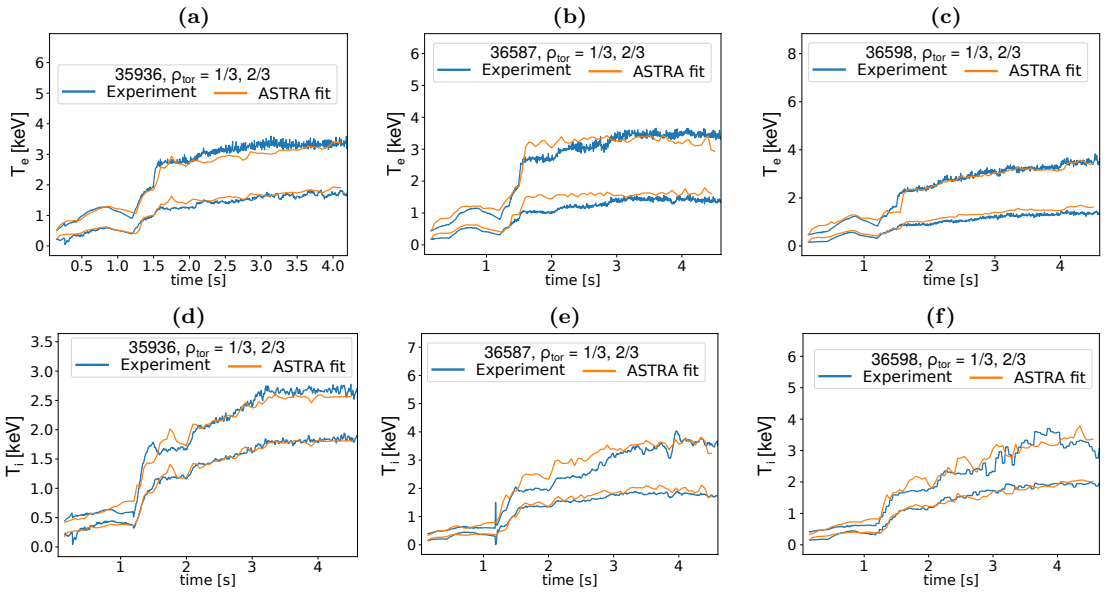

Figure A.4: Result of the best parameter fits as used in table 5.1 for AUG discharges

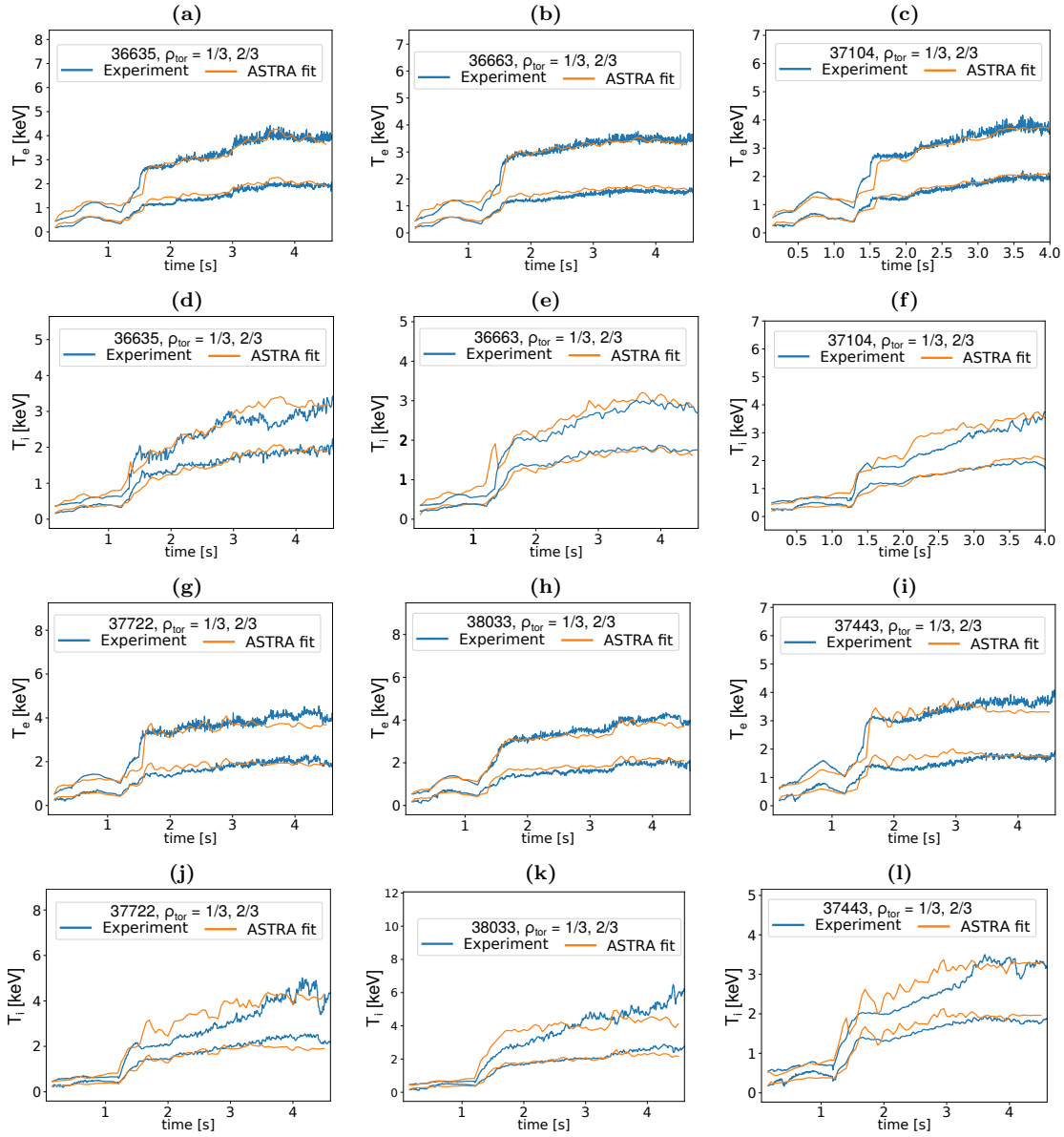

Figure A.5: Result of the best parameter fits as used in table 5.1 for AUG discharges (Figure A.4, continued)

A.4.2 JET

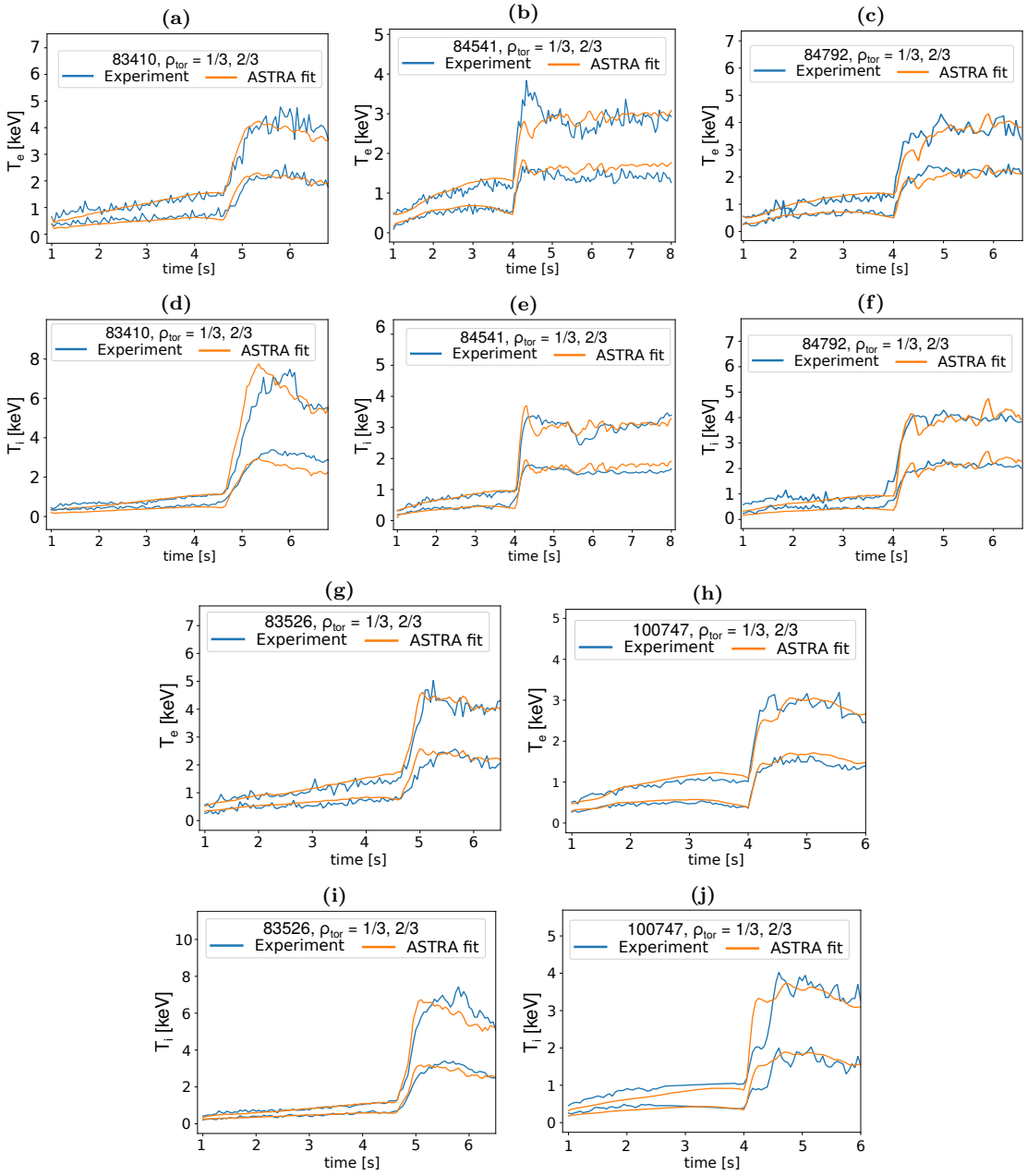

Figure A.6: Result of the best parameter fits as used in table 8.1 for JET discharges

A.5 Comparison of MHD markers to IDE

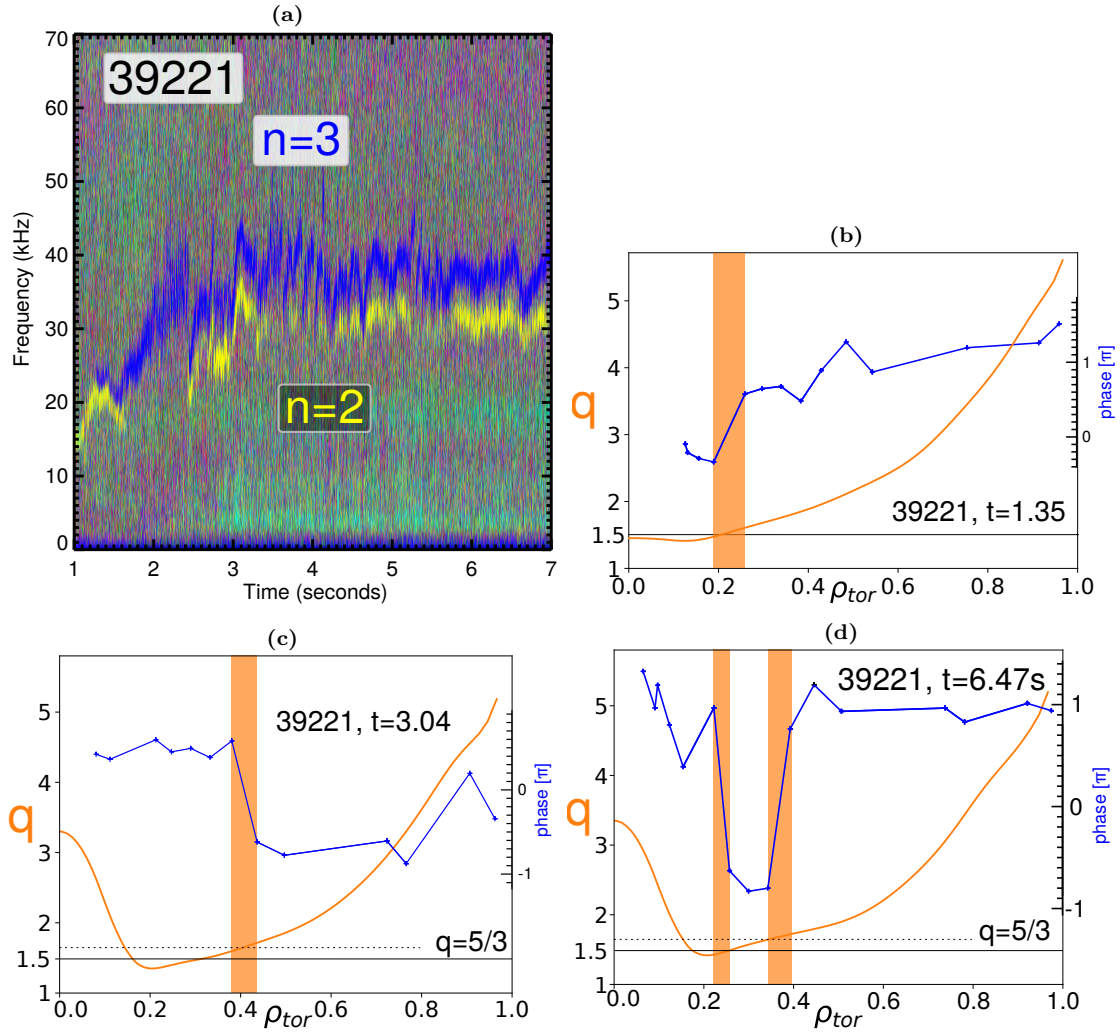

Figure A.7: Spectrogram **(a)** showing a clear n=2 and n=3 mode, and q-profiles generated by IDE compared to ECE-phase, with the region of a phase jump shaded **(c,d,e)** for AUG discharge 39221. A good agreement between the 3/2 mode location and the q-profile can be seen in **(b)**, in **(c)** the q-profile is compatible with a 5/3 mode; In **(d)**, both a 5/3 and a 3/2 mode can be seen

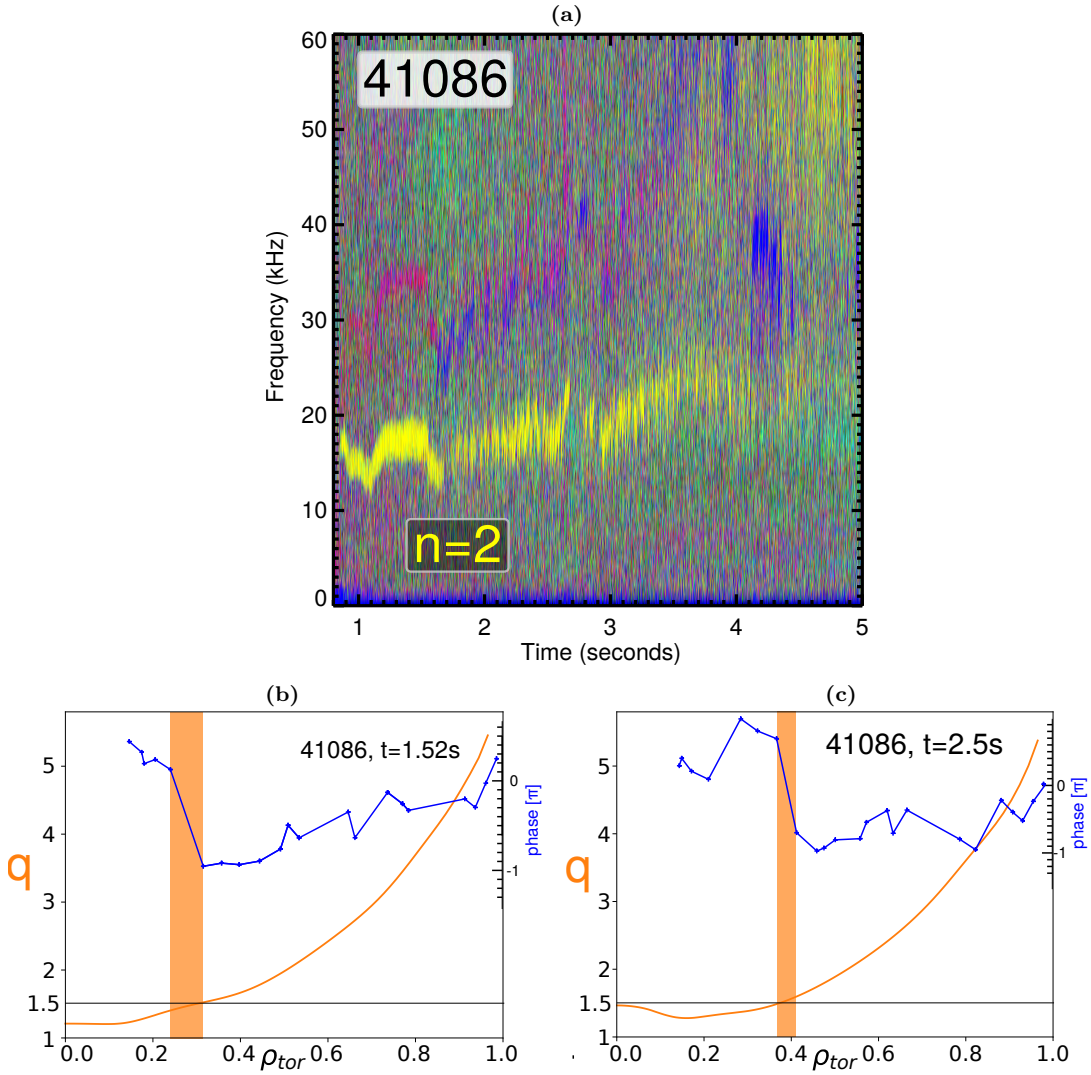

Figure A.8: Spectrogram **(a)** showing a clear n=2 mode, and q-profiles generated by IDE compared to ECE-phase **(b,c)** for AUG discharge 41086. A good agreement between the 3/2 mode location and the q-profile can be seen in **(b)** and **(c)**

Appendix B

A density model

So far, the density from previous, similar discharges was used in the simulation. As the density is a feed-back controlled parameter, this approach is reasonable. During the discharges performed for this work, it was found that this approach works well, and that the density is well described by the used setup. In this chapter, an alternative approach, where the electron density is modeled in ASTRA, is described.

B.1 The model

ASTRA can simulate the evolution of the plasma density analogous to the temperature, if the transport parameters are given. The particle diffusivity is assumed to be identical to the electron heat conductivity. An additional particle convection term is introduced to account for effects from critical gradients, shear, collisionality and β [139, 140, 141, 142].

$$C_n = -c_3 \cdot \frac{\chi_e}{R} \cdot \left(c_4 \cdot R \cdot \frac{\nabla T_e}{T_e} + c_5 \cdot S - c_1 \cdot \nu_{e,e} - c_2 \cdot \beta_e \right) \tag{B.1}$$

with the relative frequency of electron collisions $\nu_{e,e}$, and the local poloidal electron beta β_e. For the particle source, RABBIT outputs the fueling through NBI, however the influx from the edge cannot be easily modeled. Instead a scaling is used, to determine the density at the pedestal top, depending on the divertor neutral pressure $n_{0,div}$, which is the value used for the feedback control of the density in the experiment (see section 6.1). The pedestal top density is given by [143]:

$$n_{e,ped-top} = s_1 \cdot n_{e,vol} = s_1 \cdot n_{e,lin} \cdot r_{lin-vol} \tag{B.2}$$

with the volume averaged density $n_{e,vol}$ and the line averaged density $n_{e,lin}$ and a free parameter s_1. The scaling factor between the volume averaged and pedestal top density s_1 as has been determined through correlation with experimental data (see figure B.1: $s_1 = 0.9659$), where a linear dependency with a good agreement was found.

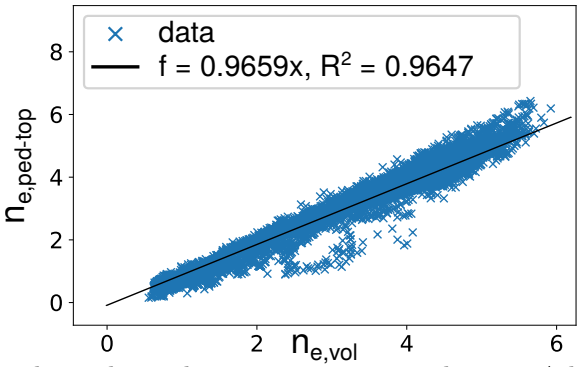

Figure B.1: Experimental correlation between $n_{e,ped-top}$ and $n_{e,vol}$; A linear dependency with a good agreement is found

The ratio between line averaged and volume averaged density can be determined through correlating with the density peaking from [144]

$$pk_{scl\ \nu} = 1.35 - 0.117 \log(\nu_{eff}) + 1.33\Gamma^*_{NBI} - 4\beta \tag{B.3}$$

with the effective NBI particle flux

$$\Gamma^*_{NBI} = 2T \frac{\Gamma_{NBI}}{Q_{tot}} \left| \frac{R}{T} \frac{dT}{dR} \right| \tag{B.4}$$

including the NBI particle flux Γ, and the effective collisionality

$$\nu_{eff} = 0.2 \langle n_e \rangle \frac{R}{\langle T_e \rangle^2} \tag{B.5}$$

where $\langle\rangle$ denotes a volume averaged quantity. All of these are available in ASTRA, leading to the scaling

$$r_{lin-vol} = s_2 \cdot pk_{scl\ \nu} + s_3 \tag{B.6}$$

The correlation factors s_2 and s_3 are also determined through experimental data (see figure B.2: $s_2 = 0.3255; s_3 = 0.3266$)

Once again a linear dependency is found, although the accuracy of this correlation is lower than in the previous case.

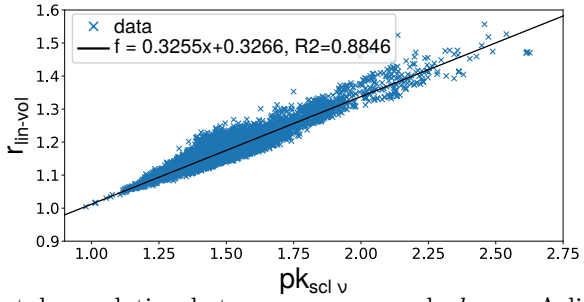

Figure B.2: Experimental correlation between $r_{lin-vol}$ and $pk_{scl\ \nu}$; A linear dependency with a good agreement is found

The line averaged density has been determined by using the scaling from [145] for a device with a tungsten wall:

$$n_e = 16.9 \cdot I_p^{0.858} \cdot B_{tor}^{-0.455} \cdot \delta^{0.274} \cdot n_{e,SOL}^{0.197} \tag{B.7}$$

The thermal loss power is negligible in this scenario and has been left out here. Since the scrape-off layer density $n_{e,SOL}$ is not available directly on AUG, the scaling was adapted to use the divertor neutral pressure $n_{0,div}$ instead:

$$sc = \frac{n_e}{16.9 \cdot I_p^{0.858} \cdot B_{tor}^{-0.455} \cdot \delta^{0.274}} = n_{e,SOL}^{0.197} \sim n_{0,div}^{s_4} + s_5 \tag{B.8}$$

The parameter s_5 is included as an acceptable fit with s_5=0 was not found. The result can be seen in figure B.3. While a trend can be seen, a large scatter is present in the data. The resulting fit achieves $R^2 \sim 0.19$ and RMSE ~ 0.2 (with $s_4 = 0.1154; s_5 = -0.265$) which is poor. As this fit still reproduces the density acceptably well (see figure B.4) and due to a lack of time to test other options, the approach was continued with this result. It may be of interest in the future, to find a different scaling, find additional dependencies or find some points, that can be excluded in order to improve the fit. Looking at a larger set of discharges may also be of interest.

In order to generate the source from the edge, a Gaussian source term is included at the location of the pedestal top. The value of this term is then adapted via feed-back control to have the pedestal-top density in the simulation match the value obtained from the scaling (see equation B.2). As the starting point at the edge is already sub-optimal, a detailed fit for the free parameters in equation B.1 was not done. It was found, that the following parameters: $c_1 = 5$, $c_2 = 10$, $c_3 = 1.5$, $c_4 = 0.2$, and $c_5 = 0.1$ produce a reasonable result.

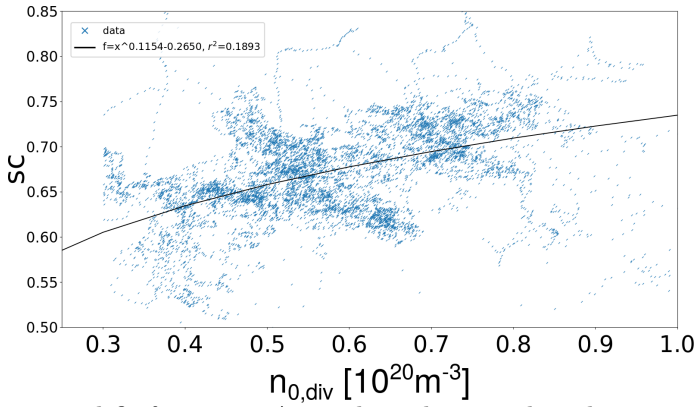

Figure B.3: Experimental fit for $n_{0,div}$; A trend can be seen, but the scatter is large enough to make any fit poor

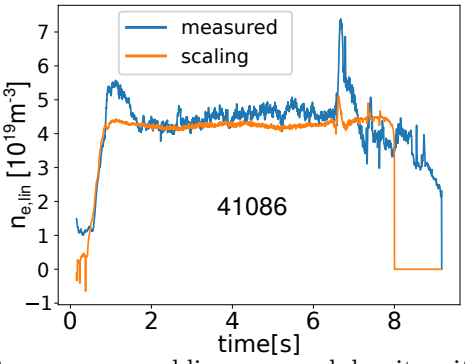

Figure B.4: Comparison between measured line averaged density with the result generated by the scaling

B.2 Results

The resulting density profiles and time evolution are shown for an exemplary discharge in figure B.5. In the time evolution, a good agreement can be seen for ρ_{tor}=0.6, while the regions further inward are underestimated. In addition to that, the density drop after the L-H transition is faster in the model. This does align with the behavior of $n_{0,div}$ and hints at possible missing physics in the transport model. This behavior could be "fixed" by making the controller for the density source less aggressive, though there is no physical motivation for that. When looking at the profiles, it can be seen that the agreement is reasonable outwards of $\rho_{tor} \sim 0.4$, becoming worse when coming closer to the core. In addition to that, due to the fluctuations in the experimental density, there are points in time where the fit is better and other where it is worse. Looking at the low density phase in the beginning of the discharge

(up to $t \sim 0.5$s) it can be seen, that the agreement is considerably worse. This does align with the behavior observed in figure B.4 and suggests, that this setup may not be applicable in this phase. It should however be mentioned, that the impact of the density in this phase on the other parameters, especially later in the discharge, is low.

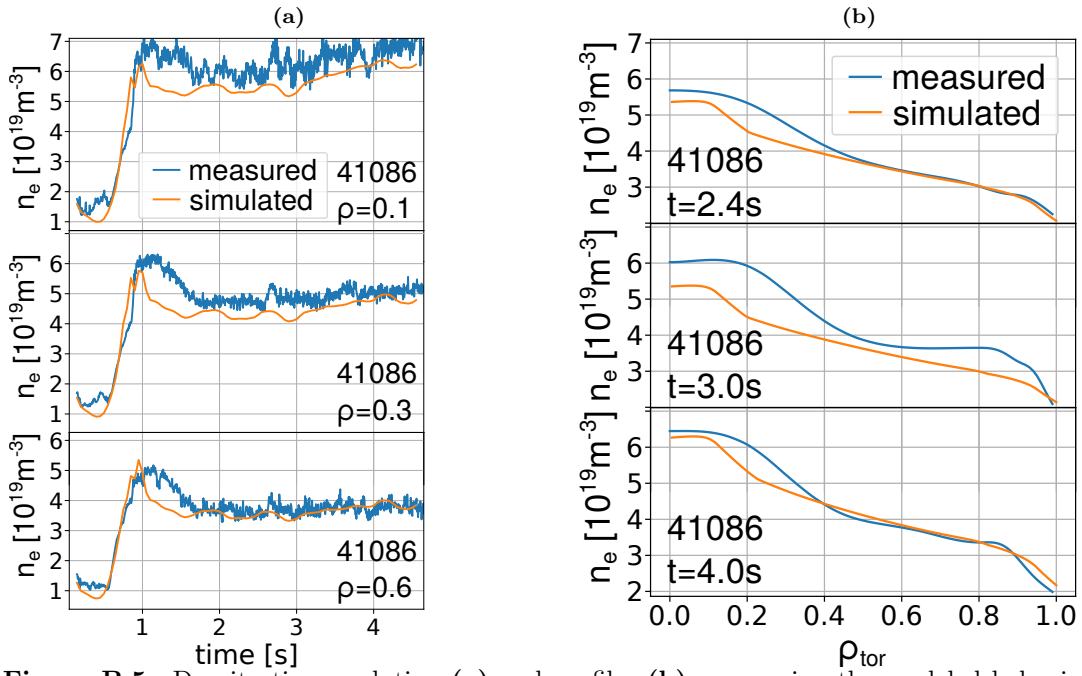

Figure B.5: Density time evolution **(a)** and profiles **(b)**, comparing the modeled behavior and the measured behavior

The impact of the simulated density on the other parameters can be seen in figure B.6, showing the time evolution of the temperature, and some representative profiles for both T_e and q. It can be seen, that the impact of the density, while not nothing is rather low. However on the minimum of q, an impact can be seen (this aligns with the behavior found in section 7.4). The same is the case for the time evolution of the electron temperature, where an increase for the ρ_{tor}=0.3 case is not recovered, possibly due to an increase in simulated density at that point. As this temperature increase is caused by an increase in NBI power, this may mean that the impact of the NBI source on the density may need to be reconfigured.

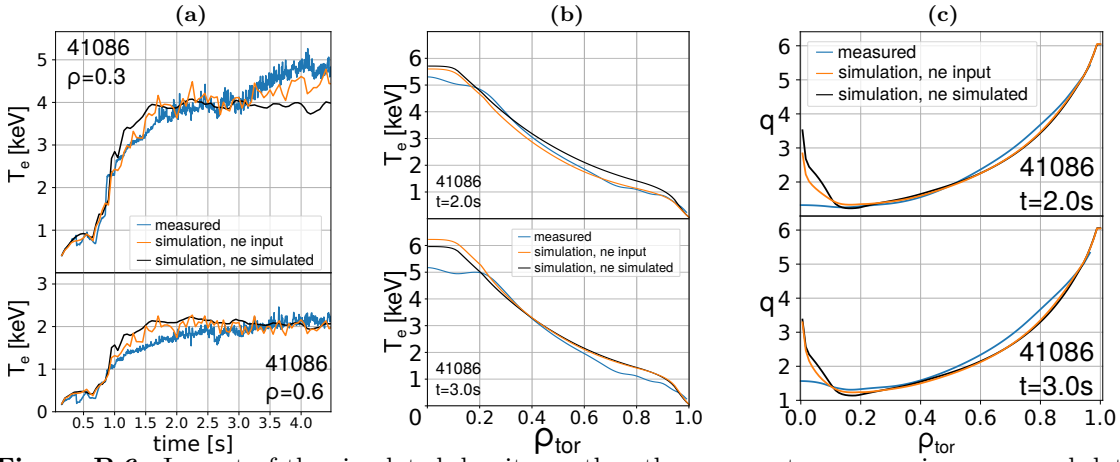

Figure B.6: Impact of the simulated density on the other parameter, comparing measured data with simulated data with and without density input

B.2.1 The density of 41400

It was found in section 7.4, that the density in discharge 41400 behaved differently than expected from previous discharges. When the density model was applied to this case, a behavior more similar to previous discharges was seen (see figure B.7), indicating either a systematic problem with the density measurement for this discharge or a different transport behavior for this discharge. The latter would put the applicability of such a density model in question.

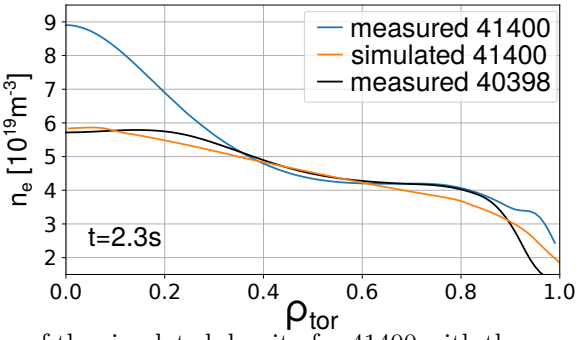

Figure B.7: Comparison of the simulated density for 41400 with the measured densities for 41400 and 40398

Glossary

AUG ASDEX Upgrade

JET Joint European Torus

DEMO European demonstration power plant

ITER International Thermonuclear Experimental Reactor

NBI Neutral Beam Injection

NBCD Neutral Beam driven current

ECRH Electron Cyclotron Resonance Heating

ECCD Electron Cyclotron Current Drive

ECE Electron Cyclotron Emission

TS Thomson Scattering

CXRS Charge Exchange Recombination Spectroscopy

DCN Deuterium Cyanide

IDA Integrated Data Analysis

IDE Integrated Data Equilibrium

EFIT Equilibrium FITting

AT Advanced Tokamak

ITB Internal Transport Barrier

HFS High Field Side

LFS Low Field Side

MHD magnetohydrodynamic

TEM Trapped Electron Mode

ITG Ion Temperature Gradient mode

H-mode high confinement mode

L-mode low confinement mode

ELM Edge Localized Mode

L-H transition Transition from L-mode to H-mode

NTM Neoclassical Tearing Mode

MARFE Multifaceted Asymmetric Radiation From the Edge

RABBIT Rapid Analytical Based Beam Injection Tool

ASTRA Automated System for Transport Analysis

RAPTOR RApid Plasma Transport simulatOR

T_i ion temperature

T_e electron temperature

q plasma safety factor

q_{95} safety factor at 95% of the flux

q_{min} minimum of the q-profile

S magnetic shear

Z_{eff} effective ion charge

β ratio of the total kinetic and magnetic pressure

β_N normalized β

β_{pol} poloidal β

I_p plasma current

ρ_{tor} normalized toroidal flux

ρ_{pol} normalized poloidal flux

τ_r current diffusion time

H_{98}	IPB98(y,2) confinement factor
n_e	electron density
$n_{0,div}$	divertor neutral density

References

[1] International Energy Agency. *World Energy Outlook 2022*. OECD, Oct. 2022. DOI: 10.1787/3a469970-en.

[2] World Meteorological Organization. *State of the Global Climate 2022*. United Nations, June 2023. DOI: 10.18356/9789263113160.

[3] *Country Nuclear Power Profiles*. Vienna: International Atomic Energy Agency, 2022. URL: https://www.iaea.org/publications/15285/country-nuclear-power-profiles.

[4] EUROFusion. *European Research Roadmap to the Realisation of Fusion Energy*. 2018. URL: www.euro-fusion.org/eurofusion/roadmap.

[5] *Positionspapier Fusionsforschung*. Bundesministerium für Bildung uns Forschung, June 2023. URL: https://www.bmbf.de/SharedDocs/Publikationen/de/bmbf/7/775804_Positionspapier_Fusionsforschung.html.

[6] J D Lawson. "Some Criteria for a Power Producing Thermonuclear Reactor". In: *Proceedings of the Physical Society. Section B* 70.1 (Jan. 1957), pp. 6–10. DOI: 10.1088/0370-1301/70/1/303.

[7] A.R. Polevoi et al. "PFPO plasma scenarios for exploration of long pulse operation in ITER". In: *Nuclear Fusion* 63.7 (May 2023), p. 076003. DOI: 10.1088/1741-4326/acd06f.

[8] Hartmut Zohm, ed. *Magnetohydrodynamic Stability of Tokamaks*. Wiley, Dec. 2014. DOI: 10.1002/9783527677375.

[9] Jeffrey P. Freidberg. *Ideal MHD*. Cambridge University Press, June 2014. DOI: 10.1017/cbo9780511795046.

[10] F Troyon et al. "MHD-Limits to Plasma Confinement". In: *Plasma Physics and Controlled Fusion* 26.1A (Jan. 1984), pp. 209–215. DOI: 10.1088/0741-3335/26/1a/319.

[11] ITER Physics Expert Group on Disruptions, Plasma Control, and MHD and ITER Physics Basis Editors. "Chapter 3: MHD stability, operational limits and disruptions". In: *Nuclear Fusion* 39.12 (Dec. 1999), pp. 2251–2389. DOI: 10.1088/0029-5515/39/12/303.

[12] Harold Grad and Hanan Rubin. "Hydromagnetic equilibria and force-free fields". In: *Journal of Nuclear Energy (1954)* 7.3-4 (1958), pp. 284–285. URL: https://citeseerx.ist.psu.edu/document?repid=rep1&type=pdf&doi=b464a18baf52ebbf9b9a1e5a3f526f87f79afa52.

[13] VD Shafranov. "Plasma equilibrium in a magnetic field". In: *Reviews of plasma physics* 2 (1966), p. 103.

[14] "The instability of a pinched fluid with a longitudinal magnetic field". In: *Proceedings of the Royal Society of London. Series A. Mathematical and Physical Sciences* 245.1241 (June 1958), pp. 222–237. DOI: 10.1098/rspa.1958.0079.

[15] VD Shafranov. "Stability of plasmas confined by magnetic fields". In: *Soviet Journal of Atomic Energy* 5 (1956), p. 38.

[16] A G Peeters. "The bootstrap current and its consequences". In: *Plasma Physics and Controlled Fusion* 42.12B (Dec. 2000), B231–B242. DOI: 10.1088/0741-3335/42/12b/318.

[17] O. Sauter, C. Angioni, and Y. R. Lin-Liu. "Neoclassical conductivity and bootstrap current formulas for general axisymmetric equilibria and arbitrary collisionality regime". In: *Physics of Plasmas* 6.7 (July 1999), pp. 2834–2839. DOI: 10.1063/1.873240.

[18] O. Sauter, C. Angioni, and Y. R. Lin-Liu. "Erratum: "Neoclassical conductivity and bootstrap current formulas for general axisymmetric equilibria and arbitrary collisionality regime" [Phys. Plasmas 6, 2834 (1999)]". In: *Physics of Plasmas* 9.12 (Dec. 2002), pp. 5140–5140. DOI: 10.1063/1.1517052.

[19] A. Redl et al. "A new set of analytical formulae for the computation of the bootstrap current and the neoclassical conductivity in tokamaks". In: *Physics of Plasmas* 28.2 (Feb. 2021). DOI: 10.1063/5.0012664.

[20] Paulett C. Liewer. "Measurements of microturbulence in tokamaks and comparisons with theories of turbulence and anomalous transport". In: *Nuclear Fusion* 25.5 (May 1985), pp. 543–621. DOI: 10.1088/0029-5515/25/5/004.

[21] F Romanelli. "Models of plasma transport based on microturbulence". In: *Plasma Physics and Controlled Fusion* 31.10 (Aug. 1989), pp. 1535–1549. DOI: 10.1088/0741-3335/31/10/005.

[22] Ulrich Stroth. *Plasmaphysik*. Springer Berlin Heidelberg, 2018. DOI: 10.1007/978-3-662-55236-0.

[23] C Angioni et al. "Particle transport in tokamak plasmas, theory and experiment". In: *Plasma Physics and Controlled Fusion* 51.12 (Nov. 2009), p. 124017. DOI: 10.1088/0741-3335/51/12/124017.

[24] X Garbet et al. "Profile stiffness and global confinement". In: *Plasma Physics and Controlled Fusion* 46.9 (July 2004), pp. 1351–1373. DOI: 10.1088/0741-3335/46/9/002.

[25] David Bohm. "The characteristics of electrical discharges in magnetic fields". In: *Qualitative Description of the Arc Plasma in a Magnetic Field* (1949).

[26] A Taroni et al. "Global and local energy confinement properties of simple transport coefficients of the Bohm type". In: *Plasma Physics and Controlled Fusion* 36.10 (Oct. 1994), pp. 1629–1646. DOI: 10.1088/0741-3335/36/10/003.

[27] B B Kadomtsev. "Tokamaks and dimensional analysis". In: *soviet journal for plasma physics* 1.4 (Jan. 1975).

[28] F. W. Perkins et al. "Nondimensional transport scaling in the Tokamak Fusion Test Reactor: Is tokamak transport Bohm or gyro-Bohm?" In: *Physics of Fluids B: Plasma Physics* 5.2 (Feb. 1993), pp. 477–498. DOI: 10.1063/1.860534.

[29] C. C. Petty et al. "Gyroradius Scaling of Electron and Ion Transport". In: *Physical Review Letters* 74.10 (Mar. 1995), pp. 1763–1766. DOI: 10.1103/physrevlett.74.1763.

[30] B. F. McMillan et al. "System Size Effects on Gyrokinetic Turbulence". In: *Physical Review Letters* 105.15 (Oct. 2010). DOI: 10.1103/physrevlett.105.155001.

[31] M Erba et al. "Validation of a new mixed Bohm/gyro-Bohm model for electron and ion heat transport against the ITER, Tore Supra and START database discharges". In: *Nuclear Fusion* 38.7 (July 1998), pp. 1013–1028. DOI: 10.1088/0029-5515/38/7/305.

[32] F. Wagner et al. "Regime of Improved Confinement and High Beta in Neutral-Beam-Heated Divertor Discharges of the ASDEX Tokamak". In: *Physical Review Letters* 49.19 (Nov. 1982), pp. 1408–1412. DOI: 10.1103/physrevlett.49.1408.

[33] ASDEX Team. "The H-Mode of ASDEX". In: *Nuclear Fusion* 29.11 (Nov. 1989), pp. 1959–2040. DOI: 10.1088/0029-5515/29/11/010.

[34] R. Bilato et al. "Heuristic model for the power threshold of the L-H transition". In: *Nuclear Fusion* 60.12 (Oct. 2020), p. 124003. DOI: 10.1088/1741-4326/abb540.

[35] *Combined Pressure and Current Driven Modes: Edge Localized Modes*. Wiley-VCH Verlag GmbH & Co. KGaA, Jan. 2015, pp. 83–102. DOI: 10.1002/9783527677375.ch6.

[36] ITER Physics Expert Group on Confin Transport, ITER Physics Expert Group on Confin Database, and ITER Physics Basis Editors. "Chapter 2: Plasma confinement and transport". In: *Nuclear Fusion* 39.12 (Dec. 1999), pp. 2175–2249. DOI: 10.1088/0029-5515/39/12/302.

[37] G. Verdoolaege et al. "The updated ITPA global H-mode confinement database: description and analysis". In: *Nuclear Fusion* 61.7 (May 2021), p. 076006. DOI: 10.1088/1741-4326/abdb91.

[38] C. Bachmanna et al. "Basic design of the EU DEMO with a low aspect ratio". In: *in preparation for Fusion Engineering and Design* (2023).

[39] R. J. Hastie. "Sawtooth Instability in Tokamak Plasmas". In: *Astrophysics and Space Science* 256.1/2 (1997), pp. 177–204. DOI: 10.1023/a:1001728227899.

[40] Claude Mercier. "A necessary condition for hydromagnetic stability of plasma with axial symmetry". In: *Nuclear Fusion* 1.1 (Sept. 1960), pp. 47–53. URL: https://doi.org/10.1088/0029-5515/1/1/004.

[41] J. W. Oosterbeek et al. "A line-of-sight electron cyclotron emission receiver for electron cyclotron resonance heating feedback control of tearing modes". In: *Review of Scientific Instruments* 79.9 (Sept. 2008). DOI: 10.1063/1.2976665.

[42] M. Reich et al. "Real-time Control of NTMs Using ECCD at ASDEX Upgrade". In: *Proceedings of the 25th IAEA Fusion Energy Conference, St. Petersburg, RF*. PPC/P1-26. IAEA Vienna. 2014. URL: http://www-naweb.iaea.org/napc/physics/FEC/FEC2014/fec2014-preprints/430_PPCP126.pdf.

[43] B. Lipschultz et al. "Marfe: an edge plasma phenomenon". In: *Nuclear Fusion* 24.8 (Aug. 1984), pp. 977–988. DOI: 10.1088/0029-5515/24/8/002.

[44] U. Stroth et al. "Model for access and stability of the X-point radiator and the threshold for marfes in tokamak plasmas". In: *Nuclear Fusion* 62.7 (Apr. 2022), p. 076008. DOI: 10.1088/1741-4326/ac613a.

[45] M. Weiland et al. "RABBIT: Real-time simulation of the NBI fast-ion distribution". In: *Nuclear Fusion* 58.8 (July 2018), p. 082032. DOI: 10.1088/1741-4326/aabf0f.

[46] T H Stix. "Heating of toroidal plasmas by neutral injection". In: *Plasma Physics* 14.4 (Apr. 1972), pp. 367–384. DOI: 10.1088/0032-1028/14/4/002.

[47] David R. Mikkelsen and Clifford E. Singer. "Optimization of Steady-State Beam-Driven Tokamak Reactors". In: *Nuclear Technology - Fusion* 4.2P1 (Sept. 1983), pp. 237–252. DOI: 10.13182/fst83-a22816.

[48] K. Okano. "Neoclassical formula for neutral beam current drive". In: *Nuclear Fusion* 30.3 (Mar. 1990), pp. 423–430. DOI: 10.1088/0029-5515/30/3/004.

[49] E Speth. "Neutral beam heating of fusion plasmas". In: *Reports on Progress in Physics* 52.1 (Jan. 1989), pp. 57–121. DOI: 10.1088/0034-4885/52/1/002.

[50] Bernhard Streibl et al. "Chapter 2: Machine Design, Fueling, and Heating in ASDEX Upgrade". In: *Fusion Science and Technology* 44.3 (Nov. 2003), pp. 578–592. DOI: 10.13182/fst03-a400.

[51] D. Ćirić et al. "Performance of upgraded JET neutral beam injectors". In: *Fusion Engineering and Design* 86.6-8 (Oct. 2011), pp. 509–512. DOI: 10.1016/j.fusengdes.2010.11.035.

[52] Alexei Pankin et al. "The tokamak Monte Carlo fast ion module NUBEAM in the National Transport Code Collaboration library". In: *Computer Physics Communications* 159.3 (June 2004), pp. 157–184. DOI: 10.1016/j.cpc.2003.11.002.

[53] R. Prater. "Heating and current drive by electron cyclotron waves". In: *Physics of Plasmas* 11.5 (May 2004), pp. 2349–2376. DOI: 10.1063/1.1690762.

[54] T. Ohkawa. "Steady-state operation of tokamaks by R-F heating". In: *Technical report, General Atomics* (1976). URL: https://library.psfc.mit.edu/catalog/online_pubs/tech_reports/GA-A13847.pdf.

[55] N. J. Fisch and A. H. Boozer. "Creating an Asymmetric Plasma Resistivity with Waves". In: *Physical Review Letters* 45.9 (Sept. 1980), pp. 720–722. DOI: 10.1103/physrevlett.45.720.

[56] J Stober et al. "Exploring fusion-reactor physics with high-power electron cyclotron resonance heating on ASDEX Upgrade". In: *Plasma Physics and Controlled Fusion* 62.2 (Jan. 2020), p. 024012. DOI: 10.1088/1361-6587/ab512b.

[57] D. Wagner et al. "Status, Operation, and Extension of the ECRH System at ASDEX Upgrade". In: *Journal of Infrared, Millimeter, and Terahertz Waves* 37.1 (July 2015), pp. 45–54. DOI: 10.1007/s10762-015-0187-z.

[58] E. Poli, A.G. Peeters, and G.V. Pereverzev. "TORBEAM, a beam tracing code for electron-cyclotron waves in tokamak plasmas". In: *Computer Physics Communications* 136.1-2 (May 2001), pp. 90–104. DOI: 10.1016/s0010-4655(01)00146-1.

[59] Wolfgang Suttrop et al. "Practical limitations to plasma edge electron temperature measurements by radiometry of electron cyclotron emission". In: *IPP-report* 1/306 (Dec. 1996). URL: https://hdl.handle.net/11858/00-001M-0000-0027-61A2-7.

[60] S S Denk et al. "Analysis of electron cyclotron emission with extended electron cyclotron forward modeling". In: *Plasma Physics and Controlled Fusion* 60.10 (Sept. 2018), p. 105010. DOI: 10.1088/1361-6587/aadb2f.

[61] B. Kurzan and H. D. Murmann. "Edge and core Thomson scattering systems and their calibration on the ASDEX Upgrade tokamak". In: *Review of Scientific Instruments* 82.10 (Oct. 2011). DOI: 10.1063/1.3643771.

[62] A. Mlynek et al. "Design of a digital multiradian phase detector and its application in fusion plasma interferometry". In: *Review of Scientific Instruments* 81.3 (Mar. 2010). DOI: 10.1063/1.3340944.

[63] R. M. McDermott et al. "Extensions to the charge exchange recombination spectroscopy diagnostic suite at ASDEX Upgrade". In: *Review of Scientific Instruments* 88.7 (July 2017), p. 073508. DOI: 10.1063/1.4993131.

[64] S K Rathgeber et al. "Estimation of profiles of the effective ion charge at ASDEX Upgrade with Integrated Data Analysis". In: *Plasma Physics and Controlled Fusion* 52.9 (Aug. 2010), p. 095008. DOI: 10.1088/0741-3335/52/9/095008.

[65] E. Viezzer et al. "High-resolution charge exchange measurements at ASDEX Upgrade". In: *Review of Scientific Instruments* 83.10 (Oct. 2012). DOI: 10.1063/1.4755810.

[66] Alberto Castillo Castillo et al. "Experimental investigation of current jumps in linear geometry hot cathode ionization gauges in strong magnetic fields". In: *Fusion Engineering and Design* 181 (Aug. 2022), p. 113194. DOI: 10.1016/j.fusengdes.2022.113194.

[67] R. Fischer et al. "Integrated Data Analysis of Profile Diagnostics at ASDEX Upgrade". In: *Fusion Science and Technology* 58.2 (Oct. 2010), pp. 675–684. DOI: 10.13182/fst10-110.

[68] M Willensdorfer et al. "Characterization of the Li-BES at ASDEX Upgrade". In: *Plasma Physics and Controlled Fusion* 56.2 (Jan. 2014), p. 025008. DOI: 10.1088/0741-3335/56/2/025008.

[69] P. J. McCarthy, P. Martin, and W. Schneider. "The CLISTE Interpretive Equilibrium Code". In: *IPP-report* 5/85 (May 1999). URL: https://hdl.handle.net/11858/00-001M-0000-0027-6023-D.

[70] R. Fischer et al. "Coupling of the Flux Diffusion Equation with the Equilibrium Reconstruction at ASDEX Upgrade". In: *Fusion Science and Technology* 69.2 (Apr. 2016), pp. 526–536. DOI: 10.13182/fst15-185.

[71] G. V. Pereverzev and P. N. Yushmanov. "ASTRA - Automated System for TRansport Analysis". In: *IPP-Report* 5/98 (Feb. 2002). URL: http://hdl.handle.net/11858/00-001M-0000-0027-4510-D.

[72] O. P. Ford et al. "Imaging motional Stark effect measurements at ASDEX Upgrade". In: *Review of Scientific Instruments* 87.11 (Aug. 2016). DOI: 10.1063/1.4959873.

[73] R. Fischer et al. "Sawtooth induced q-profile evolution at ASDEX Upgrade". In: *Nuclear Fusion* 59.5 (Mar. 2019), p. 056010. DOI: 10.1088/1741-4326/ab0b65.

[74] L.L. Lao et al. "Reconstruction of current profile parameters and plasma shapes in tokamaks". In: *Nuclear Fusion* 25.11 (Nov. 1985), pp. 1611–1622. DOI: 10.1088/0029-5515/25/11/007.

[75] N. C. Hawkes and M. Brix and. "Calibration and operational experience with the JET motional Stark effect diagnostic". In: *Review of Scientific Instruments* 77.10 (Oct. 2006). DOI: 10.1063/1.2221915.

[76] M. Brix et al. "Accuracy of EFIT equilibrium reconstruction with internal diagnostic information at JET". In: *Review of Scientific Instruments* 79.10 (Oct. 2008). DOI: 10.1063/1.2964180.

[77] R.J. Hawryluk. "An empirical approach to tokamak transport". In: *Physics of Plasmas Close to Thermonuclear Conditions*. Pergamon, 1981, pp. 19–46. DOI: https://doi.org/10.1016/B978-1-4832-8385-2.50009-1.

[78] TRANSP home page. URL: https://transp.pppl.gov/index.html.

[79] M. Kikuchi. "Steady state tokamak reactor based on the bootstrap current". In: *Nuclear Fusion* 30.2 (Feb. 1990), pp. 265–276. DOI: 10.1088/0029-5515/30/2/006.

[80] O. Sauter et al. "Steady-state fully noninductive operation with electron cyclotron current drive and current profile control in the tokamak à configuration variable (TCV)". In: *Physics of Plasmas* 8.5 (May 2001), pp. 2199–2207. DOI: 10.1063/1.1355317.

[81] Yuntao Song et al. "Realization of thousand-second improved confinement plasma with Super I-mode in Tokamak EAST". In: *Science Advances* 9.1 (Jan. 2023). DOI: 10.1126/sciadv.abq5273.

[82] R C Wolf. "Internal transport barriers in tokamak plasmas". In: *Plasma Physics and Controlled Fusion* 45.1 (Nov. 2002), R1–R91. DOI: 10.1088/0741-3335/45/1/201.

[83] J.R. Ferron et al. "High internal inductance for steady-state operation in ITER and a reactor". In: *Nuclear Fusion* 55.7 (June 2015), p. 073030. DOI: 10.1088/0029-5515/55/7/073030.

[84] T Fukuda and the JT-60 Team. "Development of high-performance discharges with transport barriers in JT-60U". In: *Plasma Physics and Controlled Fusion* 44.12B (Nov. 2002), B39–B52. DOI: 10.1088/0741-3335/44/12b/304.

[85] R. Dux et al. "Accumulation of impurities in advanced scenarios". In: *Journal of Nuclear Materials* 313-316 (Mar. 2003), pp. 1150–1155. DOI: 10.1016/s0022-3115(02)01508-8.

[86] A C C Sips, for the Steady State Operation, and the Transport Physics topical group Activity. "Advanced scenarios for ITER operation". In: *Plasma Physics and Controlled Fusion* 47.5A (Apr. 2005), A19–A40. DOI: 10.1088/0741-3335/47/5a/003.

[87] S.C. Jardin, N. Ferraro, and I. Krebs. "Self-Organized Stationary States of Tokamaks". In: *Physical Review Letters* 115.21 (Nov. 2015). DOI: 10.1103/physrevlett.115.215001.

[88] I. Krebs et al. "Magnetic flux pumping in 3D nonlinear magnetohydrodynamic simulations". In: *Physics of Plasmas* 24.10 (Sept. 2017). DOI: 10.1063/1.4990704.

[89] A. Burckhart et al. "Experimental Evidence of Magnetic Flux Pumping in ASDEX Upgrade". In: *Nuclear Fusion, submitted* (2023).

[90] M Shimada et al. "Chapter 1: Overview and summary". In: *Nuclear Fusion* 47.6 (June 2007), S1–S17. DOI: 10.1088/0029-5515/47/6/s01.

[91] H. Zohm et al. "A stepladder approach to a tokamak fusion power plant". In: *Nuclear Fusion* 57.8 (June 2017), p. 086002. DOI: 10.1088/1741-4326/aa739e.

[92] R. J. Buttery et al. "DIII-D Research to Prepare for Steady State Advanced Tokamak Power Plants". In: *Journal of Fusion Energy* 38.1 (Sept. 2018), pp. 72–111. DOI: 10.1007/s10894-018-0185-y.

[93] E. J. Strait et al. "Wall Stabilization of High Beta Tokamak Discharges in DIII-D". In: *Physical Review Letters* 74.13 (Mar. 1995), pp. 2483–2486. DOI: 10.1103/physrevlett.74.2483.

[94] J Hobirk et al. "Improved confinement in JET hybrid discharges". In: *Plasma Physics and Controlled Fusion* 54.9 (July 2012), p. 095001. DOI: 10.1088/0741-3335/54/9/095001.

[95] E. Joffrin et al. "Triggering of internal transport barrier in JET". In: *Plasma Physics and Controlled Fusion* 44.8 (Aug. 2002), pp. 1739–1752. DOI: 10.1088/0741-3335/44/8/320.

[96] Y. Sakamoto et al. "Development of reversed shear plasmas with high bootstrap current fraction towards reactor relevant regime in JT-60U". In: *Nuclear Fusion* 49.9 (Aug. 2009), p. 095017. DOI: 10.1088/0029-5515/49/9/095017.

[97] J Stober et al. "The role of the current profile in the improved H-mode scenario in ASDEX Upgrade". In: *Nuclear Fusion* 47.8 (July 2007), pp. 728–737. DOI: 10.1088/0029-5515/47/8/002.

[98] A.C.C. Sips et al. "The performance of improved H-modes at ASDEX Upgrade and projection to ITER". In: *Nuclear Fusion* 47.11 (Oct. 2007), pp. 1485–1498. DOI: 10.1088/0029-5515/47/11/010.

[99] J. Hobirk et al. "Reaching High Poloidal Beta at Greenwald Density with Internal Transport Barrier Close to Full Noninductive Current Drive". In: *Physical Review Letters* 87.8 (Aug. 2001). DOI: 10.1103/physrevlett.87.085002.

[100] C.C. Petty et al. "High-beta, steady-state hybrid scenario on DIII-D". In: *Nuclear Fusion* 56.1 (Dec. 2015), p. 016016. DOI: 10.1088/0029-5515/56/1/016016.

[101] A. Bock et al. "Non-inductive improved H-mode operation at ASDEX Upgrade". In: *Nuclear Fusion* 57.12 (Oct. 2017), p. 126041. DOI: 10.1088/1741-4326/aa8967.

[102] A. Bock et al. "Advanced tokamak investigations in full-tungsten ASDEX Upgrade". In: *Physics of Plasmas* 25.5 (May 2018). DOI: 10.1063/1.5024320.

[103] V. Philipps. "Tungsten as material for plasma-facing components in fusion devices". In: *Journal of Nuclear Materials* 415.1 (Aug. 2011), S2–S9. DOI: 10.1016/j.jnucmat.2011.01.110.

[104] A. Kallenbach et al. "Non-boronized compared with boronized operation of ASDEX Upgrade with full-tungsten plasma facing components". In: *Nuclear Fusion* 49.4 (Mar. 2009), p. 045007. DOI: 10.1088/0029-5515/49/4/045007.

[105] D. Silvagni et al. "The impact of divertor neutral pressure on confinement degradation of Advanced Tokamak Scenarios at ASDEX Upgrade". In: *Physics of Plasmas* (2023), submitted.

[106] J. Stober et al. "Advanced tokamak experiments in full-W ASDEX Upgrade". In: *26th IAEA Fusion Energy Conference* (2016). URL: https://hdl.handle.net/21.11116/0000-0003-6D96-A.

[107] R Neu et al. "Impurity behaviour in the ASDEX Upgrade divertor tokamak with large area tungsten walls". In: *Plasma Physics and Controlled Fusion* 44.6 (May 2002), pp. 811–826. DOI: 10.1088/0741-3335/44/6/313.

[108] R. Schramm et al. "Development and application of a predictive model for advanced tokamak scenario design". In: *Nuclear Fusion, submitted* (2023).

[109] E Fable et al. "Novel free-boundary equilibrium and transport solver with theory-based models and its validation against ASDEX Upgrade current ramp scenarios". In: *Plasma Physics and Controlled Fusion* 55.12 (Nov. 2013), p. 124028. DOI: 10.1088/0741-3335/55/12/124028.

[110] A. A. Ivanov et al. "New adaptive grid plasma evolution code SPIDER". In: *Proceedings of 32nd EPS Conference on Plasma Physics, Tarragona.* Vol. 29C. P-5.063. 2005. URL: https://citeseerx.ist.psu.edu/document?repid=rep1&type=pdf&doi=ecdab61f6d54cf6ca33db24203b6da545f2deadc.

[111] G. M. Staebler, J. E. Kinsey, and R. E. Waltz. "A theory-based transport model with comprehensive physics". In: *Physics of Plasmas* 14.5 (May 2007), p. 055909. DOI: 10.1063/1.2436852.

[112] C. Bourdelle et al. "A new gyrokinetic quasilinear transport model applied to particle transport in tokamak plasmas". In: *Physics of Plasmas* 14.11 (Nov. 2007), p. 112501. DOI: 10.1063/1.2800869.

[113] M Erba et al. "Extension of a Bohm model for L-mode electron heat transport to ion heat transport and to the ohmic regime". In: *Plasma Physics and Controlled Fusion* 37.11 (Nov. 1995), pp. 1249–1261. DOI: 10.1088/0741-3335/37/11/005.

[114] V.V Parail et al. "Predictive modelling of JET optimized shear discharges". In: *Nuclear Fusion* 39.3 (Mar. 1999), pp. 429–437. DOI: 10.1088/0029-5515/39/3/310.

[115] S. C. Guo and F. Romanelli. "The linear threshold of the ion-temperature-gradient-driven mode". In: *Physics of Fluids B: Plasma Physics* 5.2 (Feb. 1993), pp. 520–533. DOI: 10.1063/1.860537.

[116] F. Jenko, W. Dorland, and G. W. Hammett. "Critical gradient formula for toroidal electron temperature gradient modes". In: *Physics of Plasmas* 8.9 (Sept. 2001), pp. 4096–4104. DOI: 10.1063/1.1391261.

[117] M. Reisner et al. "Increased core ion temperatures in high-beta advanced scenarios in ASDEX upgrade". In: *Nuclear Fusion* 60.8 (July 2020), p. 082005. DOI: 10.1088/1741-4326/ab8b32.

[118] J. Puchmayr. "Optimization of Pedestal Stability on ASDEX Upgrade". In: *IPP-Report* 11/2020 (Nov. 2020). Masters Thesis. DOI: 10.17617/2.3262339.

[119] Martin Greenwald. "Density limits in toroidal plasmas". In: *Plasma Physics and Controlled Fusion* 44.8 (July 2002), R27–R53. DOI: 10.1088/0741-3335/44/8/201.

[120] R. Bilato et al. "Heuristic model for the power threshold of the L-H transition". In: *Nuclear Fusion* 60.12 (Oct. 2020), p. 124003. DOI: 10.1088/1741-4326/abb540.

[121] S. Fietz et al. "Investigation of transport models in ASDEX Upgrade current ramps". In: *Nuclear Fusion* 53.5 (Apr. 2013), p. 053004. DOI: 10.1088/0029-5515/53/5/053004.

[122] S.Van Mulders et al. "Inter-discharge optimization for fast, reliable access to ASDEX Upgrade AT scenario". In: *Nuclear Fusion, submitted* (2023).

[123] M Muraca et al. "Reduced transport models for a tokamak flight simulator". In: *Plasma Physics and Controlled Fusion* 65.3 (Feb. 2023), p. 035007. DOI: 10.1088/1361-6587/acb2c6.

[124] V Igochine et al. "Plasma effect on error fields correction at high β_N in ASDEX Upgrade". In: *Plasma Physics and Controlled Fusion* 65.6 (May 2023), p. 062001. DOI: 10.1088/1361-6587/accfbc.

[125] Van Mulders, Simon. "Full-discharge simulation and optimization with the RAPTOR code, from present tokamaks to ITER and DEMO". PhD thesis. Lausanne, EPFL, 2023. DOI: 10.5075/EPFL-THESIS-9965.

[126] Simon van Mulders. *private conversation.*

[127] J Stober et al. "Exploring fusion-reactor physics with high-power electron cyclotron resonance heating on ASDEX Upgrade". In: *Plasma Physics and Controlled Fusion* 62.2 (Jan. 2020), p. 024012. DOI: 10.1088/1361-6587/ab512b.

[128] A. G. Peeters et al. "Linear gyrokinetic stability calculations of electron heat dominated plasmas in ASDEX Upgrade". In: *Physics of Plasmas* 12.2 (Jan. 2005). DOI: 10.1063/1.1848111.

[129] F Felici and O Sauter. "Non-linear model-based optimization of actuator trajectories for tokamak plasma profile control". In: *Plasma Physics and Controlled Fusion* 54.2 (Jan. 2012), p. 025002. DOI: 10.1088/0741-3335/54/2/025002.

[130] F. Felici et al. "Real-time physics-model-based simulation of the current density profile in tokamak plasmas". In: *Nuclear Fusion* 51.8 (Aug. 2011), p. 083052. DOI: 10.1088/0029-5515/51/8/083052.

[131] F. Felici et al. "Real-time-capable prediction of temperature and density profiles in a tokamak using RAPTOR and a first-principle-based transport model". In: *Nuclear Fusion* 58.9 (July 2018), p. 096006. DOI: 10.1088/1741-4326/aac8f0.

[132] Massimiliano Lacquaniti. *private conversation.*

[133] J. Li et al. "Quasi-linear heat transport induced by ITG turbulence in the presence of impurities". In: *Nuclear Fusion* 60.12 (Oct. 2020), p. 126038. DOI: 10.1088/1741-4326/abb51f.

[134] Kyuho Kim et al. "Full-f XGC1 gyrokinetic study of improved ion energy confinement from impurity stabilization of ITG turbulence". In: *Physics of Plasmas* 24.6 (June 2017). DOI: 10.1063/1.4984991.

[135] D.L. Keeling et al. "Test of electrical resistivity and current diffusion modelling on MAST and JET". In: *Nuclear Fusion* 58.1 (Nov. 2017), p. 016028. DOI: 10.1088/1741-4326/aa9495.

[136] I Jenkins et al. "Test of current ramp modelling for AT regimes in JET". In: *Proceedings of the 37th EPS Conference on Plasma Physics (Dublin, Ireland, 2010) P*. Vol. 2. 2010. URL: https://scipub.euro-fusion.org/wp-content/uploads/2014/11/EFDC100604.pdf.

[137] Jörg Hobirk. *private conversation*.

[138] K. L. van de Plassche et al. "Fast modeling of turbulent transport in fusion plasmas using neural networks". In: *Physics of Plasmas* 27.2 (Feb. 2020), p. 022310. DOI: 10.1063/1.5134126.

[139] C Angioni et al. "Particle transport in tokamak plasmas, theory and experiment". In: *Plasma Physics and Controlled Fusion* 51.12 (Nov. 2009), p. 124017. DOI: 10.1088/0741-3335/51/12/124017.

[140] D. R. Baker and M. N. Rosenbluth. "Density profile consistency and its relation to the transport of trapped versus passing electrons in tokamaks". In: *Physics of Plasmas* 5.8 (Aug. 1998), pp. 2936–2941. DOI: 10.1063/1.873016.

[141] J. Weiland and H. Nordman. "Drift wave model for inward energy transport in tokamak plasmas". In: *Physics of Fluids B: Plasma Physics* 5.5 (May 1993), pp. 1669–1671. DOI: 10.1063/1.860801.

[142] T. Hein et al. "Gyrokinetic study of the role of β on electron particle transport in tokamaks". In: *Physics of Plasmas* 17.10 (Oct. 2010). DOI: 10.1063/1.3503622.

[143] Clemente Angioni. *private conversation*.

[144] C. Angioni et al. "Scaling of density peaking in H-mode plasmas based on a combined database of AUG and JET observations". In: *Nuclear Fusion* 47.9 (Aug. 2007), pp. 1326–1335. DOI: 10.1088/0029-5515/47/9/033.

[145] F. Ryter et al. "The upgraded ASDEX Upgrade contribution to the ITPA confinement database: description and analysis". In: *Nuclear Fusion* 61.4 (Mar. 2021), p. 046030. DOI: 10.1088/1741-4326/abe4b0.

Image sources

[A] Ralph Dux. *Plasmaphysik und Fusionsforschung Teil II: Fusionsforschung*. lecture notes.

[B] University of Wisconsin-Madison. URL: https://iec.neep.wisc.edu/operation.php.

[C] EuroFusion; e.g.: Gianmaria De Tommasi. "Plasma Magnetic Control in Tokamak Devices". In: *Journal of Fusion Energy* 38.3-4 (May 2018), pp. 406–436. DOI: 10.1007/s10894-018-0162-5.

[D] Federico Felici. "Real-Time Control of Tokamak Plasmas: from Control of Physics to Physics-Based Control". PhD thesis. EPFL Lausanne, 2011. DOI: 10.5075/EPFL-THESIS-5203.

[E] Hartmut Zohm, ed. *Magnetohydrodynamic Stability of Tokamaks*. Wiley, Dec. 2014. DOI: 10.1002/9783527677375.

[F] EUROfusion; e.g.: Arsioli Bruno. *Calculation of Neutral Beam Injection Power Deposition for He Plasmas in ASDEX Upgrade*. July 2010. DOI: 10.13140/RG.2.2.19435.13604.

[G] Ulrich Stroth. *Plasmaphysik*. Springer Berlin Heidelberg, 2018. DOI: 10.1007/978-3-662-55236-0.

[H] TW Thijs Versloot. "Edge rotation and momentum transport in JET fusion plasmas". PhD thesis. Technische Universiteit Eindhoven, 2011. DOI: 10.6100/IR715588.

[I] I T Chapman. "Controlling sawtooth oscillations in tokamak plasmas". In: *Plasma Physics and Controlled Fusion* 53.1 (Nov. 2010), p. 013001. DOI: 10.1088/0741-3335/53/1/013001.

[K] IPP. *Foto: Volker Steger*.

[L] EUROfusion. URL: https://euro-fusion.org/wp-content/uploads/2022/06/3D10.06-4c-scaled.jpg.

[M] A T Salmi et al. "NBI torque in the presence of magnetic field ripple: experiments and modelling for JET". In: *Plasma Physics and Controlled Fusion* 53.8 (May 2011), p. 085005. DOI: 10.1088/0741-3335/53/8/085005.

Acknowledgments

I would like to take the opportunity to thank everyone, who supported me during the time working on my project and contributed to generating a very friendly working environment.

I would like to begin by **Hartmut Zohm**, who gave me the opportunity to carry out this very interesting project and was my academic supervisor. His guidance and feedback during our regular meetings were invaluable.

Further, I want to thank my direct supervisor **Alexander Bock**, for defining the topic for this project and for guiding me, when the original plan did not work out as expected. You were always available, when I had questions or needed help.

I'm grateful for the very fruitful collaboration with **Simon van Mulders** providing the RAPTOR model, and contributing to a relevant amount of the experimental results presented here.

I want to thank **Jörg Stober** for many discussions regarding the experimental outcomes and for providing the idea and previous work on the counter-ECCD scenario.

I also want to thank **Emiliano Fable**, for being very helpful in setting up the ASTRA model in the beginning of my thesis and providing me with the background information required to do so. I also want to thank you for helping me, whenever I had a problem with ASTRA.

Thank you to **Giovanni Tardini** for also helping me with ASTRA, for providing a tool to make most of the spectrogram plots found in this work, and for providing me with the basics required, to adapt data from JET to a format that can be used in ASTRA.

I want to thank **Marc Maraschek** for providing a tool with which to locate MHD events in AUG, for explaining how to use it and for assisting with the localization of modes, when this was required as input to further experiments.

I want to thank **Rainer Fischer** for providing the IDE evaluation after the experiments, which was an important input for the work done during this thesis.

I want to thank **Maximilian Reisner** for doing fast IDE runs between dis-

charges, allowing for more information on where to go with a scenario in the short term.

I want to thank **Jörg Hobirk** and **Philip Schneider** for helping me understand the operational differences between AUG and JET and for helping me understand the behavior and various systems of JET.

I'm particularly grateful to all other members of **the ASDEX Upgrade Team** for making operation possible, providing explanations of their respective systems when required and for allowing me to carry out the rather large amount of discharges required to make this project work.

I want to thank **Elisabeth Wolfrum** for acting as my scientific counsel and providing helpful feedback during the status updates of my thesis.

I want to thank my office mates **Teobaldo Luda di Cortemiglia** and **Jonas Puchmayr** for many useful discussions on the smaller day to day problems and for contributing to the very friendly working environment.

Finally, I want to thank **Magdalena Bauer**, **Daniel Wendler**, **Tabea Gleiter**, **David Kulla**, **Benedikt Zimmermann**, **Felix Klossek**, **Markus Weiland**, **Sebastian Hörmann** and **Manuel Herschel** for an enjoyable time at IPP and the many interesting discussions we had during the lunch and coffee breaks.

Last but not least, my particular thanks go to the coffee group who shared with me the knowledge that there is no life without a good coffee.

This work has been carried out within the framework of the EUROfusion Consortium, funded by the European Union via the Euratom Research and Training Programme (Grant Agreement No 101052200 — EUROfusion). Views and opinions expressed are however those of the author(s) only and do not necessarily reflect those of the European Union or the European Commission. Neither the European Union nor the European Commission can be held responsible for them.